Western Graduate&PostdoctoralStudies

Western University
Scholarship@Western

Electronic Thesis and Dissertation Repository

6-5-2018 10:00 AM

Numerical and experimental investigation on the elastic properties of discontinuous fiber reinforced composites

Xiaotian Yi, *The University of Western Ontario*

Supervisor: Jiang, Liying, *The University of Western Ontario*

A thesis submitted in partial fulfillment of the requirements for the Master of Engineering Science degree in Mechanical and Materials Engineering

© Xiaotian Yi 2018

Follow this and additional works at: https://ir.lib.uwo.ca/etd

Part of the Other Mechanical Engineering Commons

Recommended Citation

Yi, Xiaotian, "Numerical and experimental investigation on the elastic properties of discontinuous fiber reinforced composites" (2018). *Electronic Thesis and Dissertation Repository*. 5431.
https://ir.lib.uwo.ca/etd/5431

This Dissertation/Thesis is brought to you for free and open access by Scholarship@Western. It has been accepted for inclusion in Electronic Thesis and Dissertation Repository by an authorized administrator of Scholarship@Western. For more information, please contact wlswadmin@uwo.ca.

Abstract

Discontinuous fiber reinforced composites (DFRC) through injection molding have been widely used in the industrial fields due to their relatively high mechanical performance and low cost. This work is directed towards developing an accurate and efficient numerical simulation package to predict the elastic properties of the injection molded DFRC for fulfilling their potential applications and reducing the expensive experimental costs.

By combining the micromechanics modeling and finite element (FE) analysis, the elastic properties of the DFRC with the aligned fibers are firstly predicted to establish a database for developing semi-empirical formulation through data fitting. Then the elastic properties of DFRC with oriented fibers are calculated through orientation averaging. An integrated software package is developed to output the elastic properties of the composites for given composite constituents, fiber volume fraction, fiber aspect ratio and fiber orientation distribution. Experimental tensile tests are performed to validate the numerical results. Microscopy-based technique and image pixel analysis are performed to determine the fiber volume fraction gradient. In order to calibrate the numerical simulation results, the effects of fiber volume fraction gradient and fiber curvature on the elastic properties of the composites are investigated. Those factors will be further considered in the integrated software package to improve the accuracy of the numerical simulation. This work is expected to advance the development of numerical techniques for composite materials.

Keywords

Discontinuous fiber reinforced composite (DFRC), injection molding, micromechanics modeling, finite element analysis (FEA), representative volume element (RVE), elastic properties.

Co-Authorship Statement

This thesis is prepared according to the specifications of the monograph format by the School of Graduate and Postdoctoral Studies at the University of Western Ontario. The co-authors of each chapter and their contributions are described as follows:

Chapter 2: Integrated software package for predicting elastic properties of DFRC

The integrated software package for predicting the elastic properties of DFRC was designed by Hui Liu, Fengrui Liu, Jia Xue, and Xiaotian Yi under the guidance of Professor Liying Jiang. The Python script and Matlab code in the integrated software package for calculating the elastic properties of DFRC were programmed by Hui Liu and Fengrui Liu, the work of coordinate transformation for calculating the elastic properties of DFRC in global coordinate system were conducted by Jia Xue and Xiaotian. All work of considering fiber volume fraction gradient and fiber curvature effects in the integrated software package were conducted by Xiaotian Yi. Drafts of Chapter 2 were written by Xiaotian Yi, and modifications were done under the supervision of Professor Liying Jiang.

Chapter 3: Experiments

The tensile tests were conducted by Hui Liu and Fengrui Liu at Ford Research and Innovation Center. The burn-off tests for determining fiber volume fraction gradient were conducted by Jia Xue and Xiaotian Yi. The specimen preparation and image acquisition for the microscopic-based method were conducted by Xiaotian Yi. All work of image pixel analysis for determining fiber volume fraction gradient are conducted by Xiaotian Yi. Drafts of Chapter 3 were written by Xiaotian Yi, and modifications were done under the supervision of Professor Liying Jiang.

Chapter 4: Fiber curvature effects

All work of fiber curvature effects on the elastic properties of DFRC are conducted by Xiaotian Yi. Drafts of Chapter 4 were written by Xiaotian Yi, and the modifications were done under the supervision of Professor Liying Jiang.

Acknowledgments

I would first like to thank my supervisor Professor Liying Jiang. The door to Prof. Jiang office was always open whenever I ran into a trouble spot or had some questions about my research or writing. She consistently and patiently guides me in the right direction whenever she thought I needed it.

Appreciation is also expressed to the following: Dr. Zeng and Dr. Li at the Ford Research and Innovation Center, for all the guidance and support they provided. Professor Klassen and Dr. Fan, for the experiment equipment and the valuable advices they provided. Dr. Xue, Dr. Xu and Dr. Zhou, for their passionate participation and input. All my friends, for their inspiration and encourage.

Finally, I must express my gratitude to my parents and to my wife for providing me with support and encouragement.

Table of Contents

Abstract i
Co-Authorship Statement ii
Acknowledgments iii
Table of Contents iv
List of Tables vii
List of Figures ix
Nomenclature xii
Chapter 1 1
1 Introduction and Literature Review 1

1.1 History and background of composites 1
1.2 Composites classification 2
1.3 Injection molding of composites 5
1.4 Mechanical properties of DFRC 7

1.4.1 Effect of properties of fiber and matrix 7
1.4.2 Effect of fiber volume fraction 9
1.4.3 Fiber aspect ratio effect 11
1.4.4 Fiber orientation effect 12

1.5 Research objective 15
1.6 Thesis outline 16

Chapter 2 17
2 Integrated software package for Predicting Elastic Properties of DFRC 17

2.1 Aligned fiber module 17

2.1.1 Finite element analysis 17
2.1.2 Semi-empirical formulae - modified Halpin-Tsai equations 22

2.2 Orientation averaging module 25

2.2.1 Orientation distribution function 26
2.2.2 Closure approximation 29
2.2.3 Orientation averaging 32
2.2.4 Coordinate transformation 33

Chapter 3 36
3. Experiments 36

3.1 Tensile tests 36
3.2 Burn-off test 39
3.3 Microscopy-based method 45

3.3.1 Specimen preparation 46
3.3.2 Microscopic image acquisition 48
3.3.3 Image pixel analysis 51

3.4 Results and discussion 57

3.4.1 Test and prediction results for G/DFRC 58
3.4.2 Test and prediction results for C/DFRC 60

Chapter 4 65
4. Fiber Curvature Effects 65

4.1 Finite element (FE) analysis on RVE with curved fibers 66

4.1.1 RVE generation 67
4.1.2 RVE meshing 71
4.1.3 Boundary conditions 73
4.1.4 Meshing convergence 76

4.2 Results and discussion 77

4.2.1 Effects of fiber curvature on the longitudinal Young's modulus 77
4.2.2 Effective fiber AR 81

Chapter 5 87
5. Conclusions, Contributions and Future Work 87

5.1 Conclusions and contributions 87
5.2 Recommendations for future work 88

References 90
Appendices 90
Appendix A: The parameters $pa(i,j)$ for IBOF 100
Appendix B: MATLAB code in the image pixel analysis and the effective fiber aspect ratio determination 101
Curriculum Vitae 108

List of Tables

Table 1.1 Mechanical properties of the fibers and matrix of the specimen (Fu et al., 2000). 8
Table 1.2 Mechanical properties of the G/DFRC and C/DFRC from tensile test (Fu et al., 2000). 8
Table 1.3 Mechanical properties of the DFRC with different fiber volume fraction in tensile test (Fu et al., 2000). 10
Table 1.4 The predicted modulus for the unit cell with different fiber curvature, the fiber is aligned in direction-1 and the fiber curvature towards to direction-2 (Bapanapalli & Nguyen, 2008)..... 10
Table 1.5 Effect of fiber AR on the effective elastic modulus (Zeng et al., 2014)..... 12
Table 1.6 Effect of fiber orientation on the mechanical properties of a DFRC (Mortazavian & Fatemi, 2015) 12
Table 2.1. Mechanical parameters of fibers and matrix..... 18
Table 3.1 The specifications of the DFRC plaque for tensile test. 37
Table 3.2 Dimension of specimen for the burn-off experiment..... 42
Table 3.3 Fiber volume fraction calculated for each segment, Image #1, #2, #3, sample B. 56
Table 3.4 Fiber volume fraction calculated for each segment, Image # 4, sample A..... 56
Table 3.5 The error of the prediction for each case of the G/DFRC plaque..... 59
Table 3.6 An example of calculating E_L, fiber volume fraction 30%..... 60
Table 3.7 The error percentage of the Young's modulus of the C/DFRC plaque with 30% fiber volume fraction..... 62
Table 4.1 RVE dimensions and fiber distance..... 70
Table 4.2 The DOF of the nodes on the RVE surfaces for the symmetric boundary conditions..... 74
Table 4.3 FE predicted longitudinal Young's modulus E_L for the RVE model with curved fibers 78
Table 4.4 The longitudinal Young's modulus E_L of the RVE model with straight fibers predicted by the integrated software package..... 82

Table 4.5 Effective fiber AR for the RVE model with typical curvature angle, for fiber VF of 10% and 15%. 83
Table 4.6 Polynomial coefficients in 3-D data fitting for the effective fiber aspect ratio (VF=10% and VF=15%) 85

List of Figures

Figure 1.1 Illustration of reinforcement types for continuous and discontinuous fibers. ... 3
Figure 1.2 The principle scheme of the injection molding machine (Dr. Dmitri Kopeliovich, 2014). ... 6
Figure 1.3 Orientation state examples and corresponding 2nd order orientation tensor.... 14
Figure 2.1 A 2-D example of periodic boundary conditions. ... 19
Figure 2.2 The comparison of the numerical results for the longitudinal Young's modulus with Halpin-Tsai and the Mori-Tanaka prediction. ... 24
Figure 2.3 Fiber orientation representation. ... 27
Figure 2.4 Illustration of the global and the local coordinate systems for the material. ... 33
Figure 3.1 Specimen cutting strategies for G/DFRC plaque. ... 37
Figure 3.2 (a) The dimension of the specimen, for both C/DFRC and G/DFRC; (b) The DIC mapping example for one of the specimens. ... 38
Figure 3.3 Specimen cutting strategies for C/DFRC plaque. ... 38
Figure 3.4 C/DFRC plaque and specimen configuration. ... 40
Figure 3.5 Image of specimen and C/DFRC plaque. ... 40
Figure 3.6 Skin-core-skin configuration for the burn-off test. ... 41
Figure 3.7 Specimens with the mount. ... 42
Figure 3.8 Burn-off test equipment. ... 43
Figure 3.9 The TGA curve for specimen #1. ... 44
Figure 3.10 The remaining carbon fibers after burn-off test. ... 45
Figure 3.11 Illustration of the specimen grinding and polishing direction for the Microscopy-based method. ... 46
Figure 3.12 The specimens after cold mounting process. ... 47
Figure 3.13 polishing machine and polishing powder for the C/DFRC specimen. ... 47
Figure 3.14 Specimen levelling press. ... 48
Figure 3.15 Comparing different magnification for sample A and B. ... 50
Figure 3.16 Example image for the specimen with WF=40%, the magnificent for the objective lens and the eyes lens are 500 and 10 respectively. ... 51
Figure 3.17 Image chopping for pixel analysis, Image #1 for Sample B. ... 52

Figure 3.18 Binary images with different grey level for Image #1 of sample B. 54
Figure 3.19 Illustration of the image segments of Image #1 of sample B. 55
Figure 3.20 Typical stress-strain curve for the tensile test with tested specimens. 57
Figure 3.21 Result comparing for GFRC plaque with 15 % fiber volume fraction..... 58
Figure 3.22 Result comparing for GFRC plaque with 10% fiber volume fraction..... 59
Figure 3.23 Comparison of the Young's modulus between test and predictions at different locations of the C/DFRC plaque with 30% fiber volume fraction..... 61
Figure 3.24 Comparison of the Young's modulus between test and predictions at different locations of the C/DFRC plaque with 16% fiber volume fraction..... 63
Figure 4.1 Illustration of the single curved fiber. 67
Figure 4.2 The example of overlapping fiber in the RVE model with curved fibers. 69
Figure 4.3 The fiber bundle and the Geometry of the RVE..... 70
Figure 4.4 Cutting plane of the RVE model meshed by different type of elements..... 72
Figure 4.5 Example of meshing of the RVE model with aligned fiber, VF=10%, AR=20. 73
Figure 4.6 Example RVE with the surfaces applied boundary condition..... 74
Figure 4.7 Illustration of a RVE before and after deformation..... 75
Figure 4.8 Variation of the Young's modulus E_L with the increasing element number (fiber VF=10%, AR=20)..... 76
Figure 4.9 Variation of the normalized longitudinal Young's modulus with fiber curvature angle for different fiber AR (VF=10%). 79
Figure 4.10 Variation of the normalized longitudinal Young's modulus with fiber curvature angle for different fiber VF (AR=20). 80
Figure 4.11 Influence of fiber AR and fiber curvature angle on the normalized longitudinal Young's modulus, fiber VF =10%..... 80
Figure 4.12 The fitting curve for the longitudinal Young's modulus E_L of the G/DFRC with straight fibers, (a) VF=10%, (b) VF=15%. 82
Figure 4.13 The effective fiber AR versus fiber curvature angle for the RVE models with different fiber VF and true fiber AR 84
Figure 4.14 Effective fiber AR for composites with VF = 10% to be used in the integrated software package..... 85

Figure 4.15 Effective fiber AR for composites with VF =15% to be used in the integrated software package..... 86

Nomenclature

E_f	Young's modulus of fiber
E_m	Young's modulus of matrix
E_c	Tensile modulus of composite
σ_f	Tensile strength of fiber
σ_m	Tensile strength of matrix
σ_c	Tensile strength of composite
μ_f	Poisson's ratio of fiber
μ_m	Poisson's ratio of matrix
λ_f	Fiber efficiency factor
d_f	Diameter of fiber
l_f	Length of fiber
V_f	Fiber volume fraction
u	Displacement field
$\boldsymbol{\varepsilon}^0$	Strain field
$\{\boldsymbol{\sigma}\}$	Stress vector
$\{\boldsymbol{\varepsilon}\}$	Strain vector
$[\boldsymbol{C}]$	Stiffness matrix
$[C_{KM}]$	Stiffness matric of the DFRC in the global coordinate system
$[C_{KM}]_P$	Stiffness matrix of the DFRC in the local coordinate system
$[\boldsymbol{S}]$	Compliance matrix
V	Volume of RVE
Φ_{hetero}	Strain energy
E_L	Longitudinal modulus
E_T	Transverse modulus
G_{LT}	Shear modulus in the L-T plane
G_{TT}	Shear modules in the transverse plane
μ_{LT}	Longitudinal Poisson's ratio

μ_{TT}	Transverse Poisson's ratio
$\psi(\mathbf{p})$	Orientation distribution function
$\mathbf{p}$	Unit orientation vector of fiber
a_{ij}	2nd order orientation tensor
a_{ijkl}	4th order orientation tensor
λ	Eigenvalue of the orientation tensor
$\underset{e}{\rightarrow}$	Eigenvector of the orientation tensor

Chapter 1

1 Introduction and literature review

1.1 History and background of composites

Nowadays composite materials are getting more popular in many fields, such as automotive, aerospace, architecture, energy, and infrastructure industries. The history of composites can date back to 1500 B.C. The early Egyptian and Mesopotamian mixed mud and straw to make stronger and more reliable buildings. In 1200 A.D. the Mongols combined wood, glue, and bones to create the first composite bow which was highly durable. Since the fiberglass was made in the late 1930s, the history of modern composites has begun (Adams, 1987).

A composite material is generally made from at least two constituent materials which often have different physical or chemical properties. These two constituents are the reinforcement and the matrix, respectively. The reinforcement is usually harder and stronger than the matrix, which provides the strength and stiffness for the composites. The functions of the matrix are binding the reinforcements together, maintaining the reinforcements within a proper spacing, and protecting the reinforcements from abrasion or the environmental detriments (Stevenson, 2011).

In terms of mechanical properties, the composite is better than its constituent materials used alone. In general, the major benefit of the composite materials is that they are light as well as strong. Compared with metals, composite materials have low density while maintaining high stiffness and strength, so that the weight reduction of composite products can be achieved. Moreover, the composites can be made as anisotropic materials. Therefore, the composites have the advantages in designing the parts which need different allowable stresses in different directions. For example, a cylindrical vessel has twice allowable stress in the hoop direction than in the longitudinal direction (Campbell, 2010).

1.2 Composites classification

The matrix provides a continuous phase for the composites, and the loads can be transferred from the matrix to the reinforcements by shearing. Polymers, metals, and ceramics are the most common matrix materials used for modern composites. Compared with polymers, the strength and the stiffness of metals are higher, as well as the ductility. Ceramics have higher strength and stiffness than polymers; however, they are more brittle. Nevertheless, polymer matrix composites have the largest produced quantities due to their lower manufacturing cost and relatively good performance (Wang et al., 2011).

The polymer matrix can be classified into two categories, i.e., thermosets and thermoplastics. The thermoset materials include polyesters, epoxies, bismaleimides, and etc. During the curing process of thermoset materials, the 3-D crosslinked structures are formed to connect polymer chains, which is an irreversible process. The common thermoplastic polymers are polyesters, polyetherimide, polyamide imide. Unlike the curing process of the thermosets, the thermoplastic polymers can be reprocessed when the temperature reaches to a certain value. The cost for producing thermoset composites is more expensive than the thermoplastic composites since the production conditions are more rigorous for both temperature and pressure. In addition, due to the 3-D crosslinked structures, the thermosets are more thermally stable than the thermoplastics. However, the thermoplastics which have the semi-crystalline microstructures have been developed recently. These materials also have an excellent strength at a high temperature, such as PEEK. (Chawla et al., 2012; Rezaei et al., 2009; Wang et al., 2011).

Based on the reinforcements, the composites can be classified as particle-reinforced, fiber-reinforced and structural composites. Generally, the particle-reinforced composite is the cheapest one among these three categories. Based on the size of the particles, two kinds of particle-reinforced composites are defined, i.e., large-particle composites and dispersion-strengthened composites respectively. For example, concrete is the most common large-particle composite. The upper limit of the mechanical properties of the large-particle composites can be estimated by the rule of mixtures (Aleksendrić & Carlone, 2015; Karsli & Aytac, 2013; Velmurugan, 2012). The size of particles in the dispersion-strengthened

composites is much smaller than the large-particle composites, and the matrix is the main portion to bear the applied load. Meanwhile, the dislocation motion is inhibited by these small particles (Kim, 2000). Laminar composites and sandwich panels are two typical structural composites. The laminar composites are formed by stacking and gluing the high-strength sheets together, such as the modern skis. The sandwich panels are normally made by a low-density core layer and two skin layers attached on each side of the core. Due to their lower density and high bending stiffness, the sandwich panels are often used in the aircraft structures (Ajit, 2009; Asp & Greenhalgh, 2014).

The fiber-reinforced composites consist of a matrix and at least one kind of fiber material. Due to their high strength and stiffness and low density, the fiber-reinforced composites are widely used in many applications, such as helicopters, satellite systems, and golf or tennis rackets. The fiber-reinforced composites can be classified into different categories based on the fiber length, the materials of fibers, and the fabrication processes (Kepnang et al., 2009; Panthapulakkal & Sain, 2007; Stevenson, 2011; Velmurugan, 2012).

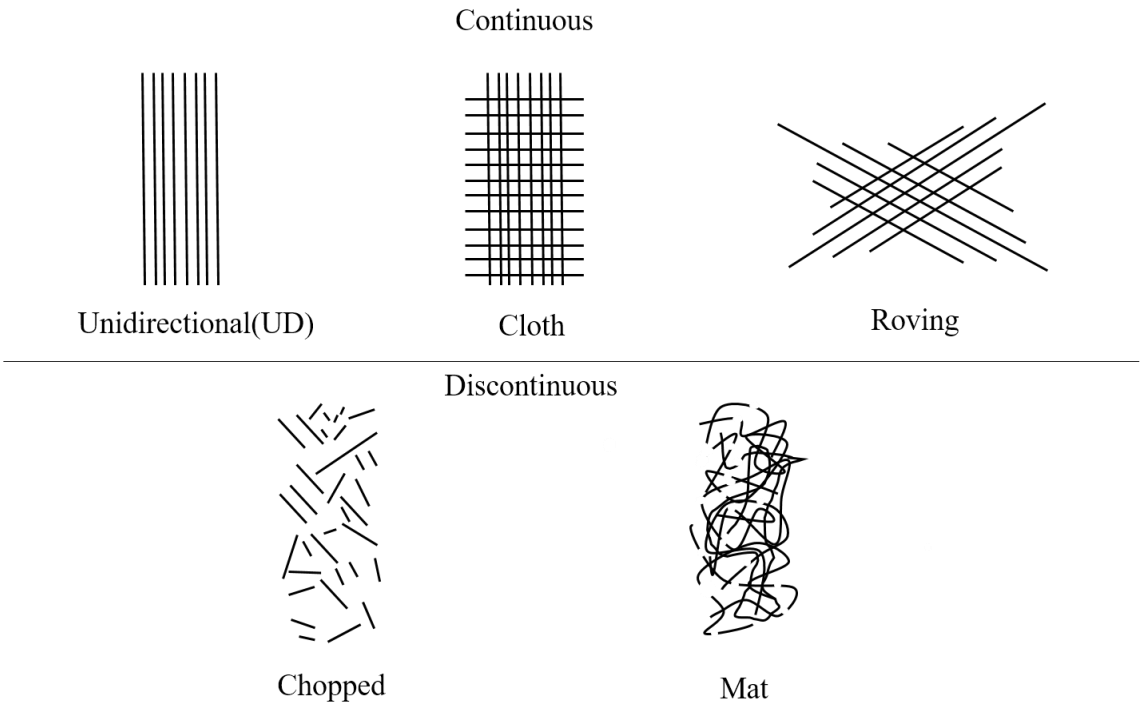

Figure 1.1 Illustration of reinforcement types for continuous and discontinuous fibers.

Based on the fiber length, the fiber-reinforced composites fall into two categories, discontinuous fiber-reinforced composites (DFRC) and continuous fiber-reinforced composites, respectively. The illustration for each reinforcement type is shown in Figure 1.1. Commonly, the discontinuous fibers are randomly oriented in the composites, such as chopped fibers and mat fibers. While the continuous fibers are often arranged well, like the unidirectional, woven and roving fibers. Due to the difference of the fiber arrangements, the discontinuous fiber composites have lower mechanical properties than the continuous fiber composites in a particular direction. (Aleksendrić & Carlone, 2015).

The definition of the discontinuous fiber is relative to the continuous fiber. The length of the continuous fiber is usually over fifteen times of its critical length, while the length of the discontinuous fiber is shorter than this value. The critical fiber length can be calculated based on the fiber diameter, the tensile strength, and the fiber-matrix bond strength. When the fiber length equals to its critical length, the maximum applied stress on the composite is the same as the fiber tensile strength. All the load will be transmitted from the matrix to the fibers when the fiber length is longer than this critical length. On the contrary, if the fiber is shorter than its critical length, only a portion of load can be transmitted from the matrix (Callister, 2006). Therefore, the continuous fiber-reinforced composites usually have more effective fiber strengthening compared to the DFRC. However, as the development of the DFRC in recent years, the stiffness and tensile strength of the DFRC could reach over 50% of their continuous counterparts. In addition, compared to the continuous fiber reinforced composites, the DFRC have more advantages in designing the products which require complex shape, and the fabrication process of DFRC is easier and faster (Stevenson, 2011; Prashanth et al., 2017).

In terms of fiber materials, the fibers can be classified as natural fibers and synthetic fibers. Natural fibers can be produced from plants and geological processes, such as wood fibers, wool fibers, and the mineral fibers. The synthetic fibers do not exist in nature, while they are produced by chemical synthesis. Metallic fibers, carbon fibers, and glass fibers are typically synthetic fibers. Metallic fibers are usually ductile materials, such as copper, gold, silver, and aluminum (Stevenson, 2011; Prashanth et al., 2017). The reinforcements we studied in this work are carbon fiber and glass fiber. Carbon fibers usually have 5-10

micrometers in diameter and a nearly cylindrical shape. Because of the crystal alignment between the carbon atoms, the carbon fibers have a high strength to volume ratio. The diameter of glass fibers is usually larger than that of carbon fibers, which can be more than 20 micrometers. The glass fibers also have the advantages in strength to volume ratio, even though it is not as high as the carbon fibers. Because of the relative cheap fabrication cost and the good mechanical properties, the glass fibers have been widely applied in the products which require a large amount of composites, such as boats. While carbon fibers are often used in racing cars to significantly reduce the weight. Moreover, the carbon fibers have good conductivity, while the glass fiber are non-conductors (Fu et al., 2000; Jagannatha et al., 2015; Karsli & Aytac, 2013; Prashanth et al., 2017).

1.3 Injection molding of composites

There are numerous processes for manufacturing composites, including lay-up, vacuum bagging, liquid resin molding, thermoforming, filament winding, compression molding, and injection molding. Each process has its advantages and limitations. The selection of the manufacturing process is usually contingent on the composite design, such as the constituents of the composite, the required geometry of the composite, and the economic cost (Aleksendrić & Carlone, 2015; Barkoula et al., 2008; Campbell, 2010). The injection molding is one of the most favorable composite manufacturing processes since it has better economic advantages in designing the composites with complex structure. In addition, the injection molding allows a wide range of materials for selection. For the injection modeling, the reinforcing materials could be chopped carbon fibers and glass fibers, and the host matrix can be both thermosets and thermoplastics.

The principle scheme of the injection molding is shown in Figure 1.2 as a simple example. During the processing, the molten polymer is mixed with the fibers, and then the fiber-polymer mixtures are transferred by the screw through the barrel. The mixtures can be heated and softened in the barrel. The reciprocating screw is applied in the injection molding machine, which can move both forward and backward according to the molding cycle. Then the mixtures are injected into a mold cavity with desired shape under high pressure. One disadvantage of the injection molding is the limitation of fiber length, i.e.,

the fibers need to be chopped in a discontinuous form and are mixed with the matrix. DFRC are the most common products from the injection molding (Thi et al., 2015; Vincent et al., 2005).

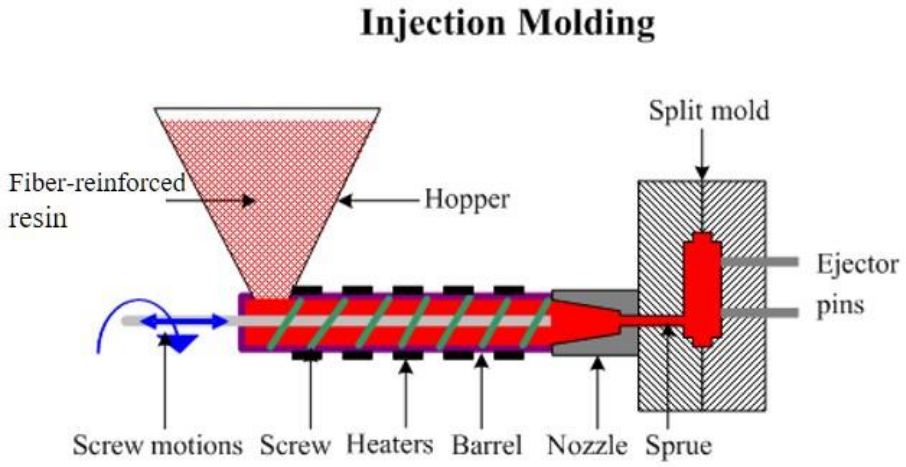

Figure 1.2 The principle scheme of the injection molding machine (Dr. Dmitri Kopeliovich, 2014).

By adding the chopped fibers into the polymer matrix through the injection molding, the DFRC materials can have strong mechanical properties and obtain a desired shape (Bledzki & Faruk, 2004; Panthapulakkal & Sain, 2007). However, the mechanical properties of the injection-molded DFRC does not only depend on the contents of the reinforcing fibers and the host matrix. Other factors such as the fiber aspect ratio, fiber orientation, fiber volume fraction gradient, fiber curvature also have significant effects on the mechanical properties of DFRC (Abdulmajeed et al, 2011; Houshyar et al., 2005; Houshyar et al., 2005; Rezaei et al., 2009; Thomason & Vlug, 1996). For example, when the fiber-matrix mixtures are forced into the cavity under high pressure, the discontinuous chopped fibers are usually oriented in the DFRC, resulting in the material anisotropy. Therefore, the DFRC is not as strong as the continuous fiber-reinforced composites in the fiber alignment direction. In addition, the injection molding usually causes a non-uniform distribution of the fibers in the DFRC parts (Liu et al., 2016; Zeng et al., 2014, 2015). Therefore, for the consideration of DFRC application, it is necessary to investigate how the mechanical properties of DFRC are affected by those factors.

1.4 Mechanical properties of DFRC

Generally, the mechanical properties of the DFRC materials include stiffness, strength, fatigue life, wear and corrosion resistances, etc. The stiffness is the deformation resistance of the DFRC materials, and it describes the relationship between the stress and the strain in the DFRC materials (Velmurugan, 2012). The stiffness is usually the primary factor for selecting a DFRC material. Commonly, the DFRC materials are required a high stiffness at a low density (Rosen, 1973).

The major factors that affect the mechanical properties of the injection-molded DFRC are the material properties of fibers and the matrix, fiber volume fraction (VF), fiber aspect ratio (AR), and fiber orientation (Abdulmajeed et al., 2011; Advani & Tucker, 1987; Fisher et al., 2003; Houshyar et al., 2005; Kunc et al., 2015; Pan, 1993; Tandon & Weng, 1984; Tucker & Liang, 1999b; Vincent et al., 2005). Some other factors may include environment temperature, composite void content, fiber-matrix chemical and mechanical bonding (Kepnang et al., 2009; Velmurugan, 2012).

Based on the applications of the DFRC, the fiber VF and AR should be determined before the DFRC fabrication (Abdulmajeed et al., 2011; Robinson & Robinson, 1994). However, the fiber VF distribution may not be uniform and the fiber orientation distribution could vary at different locations of the DFRC plaque, which is the main reason for the anisotropic and non-homogenous mechanical properties of DFRC. (Abdulmajeed et al., 2011; Fu et al., 2000; Fu & Lauke, 1996; Notta-Cuvier et al., 2014; Zeng et al., 2014, 2015).

1.4.1 Effect of properties of fiber and matrix

The mechanical properties of the composite are directly affected by its constituents' properties, such as the Young's modulus of the fibers and the matrix. The tensile properties of the discontinuous glass fiber reinforced composite (G/DFRC), the discontinuous carbon fiber reinforced composite (C/DFRC), and their constituents were tested by a Zwick 1456 machine (Fu et al., 2000). The mechanical properties of the tested fibers and matrix are extracted and shown in Table 1.1.

Material	Tensile strength (MPa)	Young's modulus (GPa)
Glass fiber	1956	78.51
Carbon fiber	3950	238
Polypropylene	31.60	1.30

Table 1.1 Mechanical properties of the fibers and matrix of the specimen (Fu et al., 2000).

As shown is Table 1.1, both the tensile strength and the Young's modulus of the carbon fibers are higher than those of the glass fibers. With the same fiber volume fraction (25 %), tensile test results of the G/DFRC and C/DFRC from this work are shown Table 1.2. As observed in this table, both the tensile strength and the tensile modulus of the C/DFRC are higher than the properties of the G/DFRC. In addition, from the results of the tensile tests on the specimen with the hybrid fibers (12.5 % glass fiber and 12.5 % carbon fiber), the mechanical properties were found higher than the G/DFRC and lower than the C/DFRC (Fu et al., 2006). Therefore, the mechanical properties of the DFRC are directly affected by the properties of its constituents. Because the mechanical properties of the matrix are too small relative to the fibers, the mechanical properties of the fibers are the upper bound of the DFRC, while the mechanical properties of the matrix are the lower bound (Tucker & Liang, 1999b).

Material	Tensile strength (MPa)	Tensile modulus (GPa)
G/DFRC	50.05	8.50
C/DFRC	59.02	14.80

Table 1.2 Mechanical properties of the G/DFRC and C/DFRC from tensile test (Fu et al., 2000).

Since the chopped fibers have random fiber orientation in the injection molded DFRC, the classical rule of mixtures cannot be used to predict the mechanical properties of DFRC directly. By adding the fiber efficiency factor (λ_f), the effects of the fiber orientation and length can be considered in the rule of mixtures as shown below (Fu et al., 2000):

$$E_c = \lambda_f E_f V_f + E_m(1-V_f) \tag{1.1}$$

where *E* represents the tensile modules, and the subscripts *c*, *f* and *m* denote the composite, fiber, and matrix, respectively. V_f is the fiber volume fraction. Similarly, the tensile strength (σ_c) of the DFRC can be determined as (Fu et al., 2000):

$$\sigma_c = \lambda_f \sigma_f V_f + \sigma_m (1 - V_f) \tag{1.2}$$

where σ is the strength. It should be noted that the fiber efficiency factor (λ_f) in Eq. (1.1) and Eq. (1.2) takes different values since the effects of fiber orientation and length on the tensile modulus and the tensile strength of DFRC are different. The mechanical properties of the DFRC determined by the modified rules of mixtures have the same tendency as the tensile test results (Fu et al., 2000). With the same fiber volume fraction, the C/DFRC have better mechanical properties than the G/DFRC. However, the cost of the G/DFRC is more economic (Fu et al., 2006; Stevenson, 2011).

1.4.2 Effect of fiber volume fraction

Once the constituents of the composite are confirmed, the effect of fiber volume fraction on the mechanical properties of the DFRC is significant. In order to get higher mechanical properties for the composites, higher fiber volume fraction is preferred for most cases (Fu et al., 2000). The mechanical properties for the DFRC with different fiber volume fractions are determined by tensile tests and shown in Table 1.3. However, it is found that the increment of the mechanical properties of DFRC is not proportional to the fiber volume fraction. Particularly when the fiber volume fraction reaches a certain value, the mechanical properties even dropped down as observed in the literature (Rezaei et al., 2009). In other words, as the fiber volume fraction increases, the fiber efficiency in Eq. (1.1) and Eq. (1.2) will decrease. Take the C/DFRC properties in Table 1.3 as an example, the fiber efficiency factors in Eq. (1.1) are determined as 0.48, 0.32, and 0.24 according to the fiber volume fraction of 8%, 16% and 25%, respectively (Fu et al., 2000). This analytical formulation provides a similar prediction trend as the experimental data.

One reason that causes the increment limit of the properties of the DFRC is the formation of fiber bundles. As the fiber volume fraction increases in the injection molded DFRC, the possibility of forming fiber bundles increases. The fiber bundle will cause two typical problems. One problem is that there will be not enough matrix material to fill the gap

between the fibers, resulting in the insufficient load transfer efficiency (Houshyar et al., 2005). The second one is that some fibers in the bundle get curved, which will also decrease the fiber reinforcement efficiency in particular direction. Finite element analysis on a unit cell which contains a curved fiber was performed to investigate the effects of the fiber curvature on the mechanical properties of the composite (Bapanapalli & Nguyen, 2008). The results as shown in Table 1.4 indicate that the fiber curvature degrades the elastic modulus along the fiber alignment direction. However, the elastic modulus in the other directions may either increase or vary a little. Since the fiber bundles can cause a remarkable stiffness reduction in the fiber alignment direction, the increment of the mechanical properties of DFRC will confront a bottle-neck after the fiber volume fraction reaches a certain value (Bapanapalli & Nguyen, 2008; Tucker & Liang, 1999a).

Material	Fiber VF	Tensile strength (MPa)	Tensile modulus (GPa)
G/DFRC	8%	48.70	5.60
	16%	49.20	7.25
	25%	50.05	8.50
C/DFRC	8%	57.40	10.35
	16%	57.75	13.35
	25%	59.02	14.80

Table 1.3 Mechanical properties of the DFRC with different fiber volume fraction in tensile test (Fu et al., 2000).

Curvature angle	E_{11} (MPa)	E_{22} (MPa)	E_{33} (MPa)
0°	8920	3010	3650
30°	7630	3010	3590
42°	6650	3250	3630
60°	5670	3580	3680

Table 1.4 The predicted modulus for the unit cell with different fiber curvature, the fiber is aligned in direction-1 and the fiber curvature is towards to direction-2 (Bapanapalli & Nguyen, 2008).

Since continuously increasing the fiber volume fraction after a certain point will not have an improvement on the mechanical properties of the DFRC, researchers attempted to

determine the optimal fiber volume fraction of the DFRC through theoretical modeling (Pan, 1993). Based on the model of elastic stress transfer, both the upper and the lower limits of the fiber volume fraction in the DFRC can be determined. Within this appropriate range of fiber volume fraction, the mechanical properties of composites increase with the increasing of the fiber volume fraction efficiently (Houshyar et al., 2005; Pan, 1993).

In addition, from the images of the injection molded composite plaque, it is observed that the fiber volume fraction is not uniform through the thickness direction. For example, the X-ray CT scan images showed that the fiber volume fraction at the core layer is higher than the skin layers (Zeng et al., 2014, 2015). For some locations in the tested plaque, the volume fraction of the core layer is even two times of the skin layer. The experiment methods based on two typical optical microscopy image analyses were applied and compared by Cann et al. (2008) to determine the accurate volume fraction gradient through the thickness direction of the plaque.

1.4.3 Fiber aspect ratio effect

The fiber aspect ratio (AR) is defined as the fiber length over its diameter, i.e., l_f/d_f. Table 1.5 shows the tested mechanical properties of the specimens with different fiber AR (Zeng et al., 2014). When the fiber volume fraction and the orientation distribution are fixed, it is found that the elastic modulus of the composite increases with the increasing of fiber AR, particularly for the range from 5 to 50. However, the increment of the elastic modulus is not significant for the AR from 50 to 100. The elastic properties of the glass fiber reinforced polypropylene with different sets of fiber length were determined from both experimental and analytical methods by Thomson and Vlug (1996), which indicates that the elastic modulus becomes more independent when the fiber length is larger than 0.5 mm. The results are consistent with the conclusion in the other studies (Fu et al., 2000; Nguyen et al., 2008; Robinson & Robinson, 1994; Zeng et al., 2014). When the fiber diameter is confirmed, the effect of the fiber AR is actually the effect of the fiber length. The interface between the fibers and matrix will increase as the increasing of the fiber length, resulting in more efficient stress transferred from the matrix to the fibers. Therefore, the increase of

the fiber AR will get higher elastic properties of DFRC within a certain range of the fiber AR.

Fiber AR	5	15	20	25	50	100
Elastic modules (MPa)	2100	4140	4750	5050	5980	6190

Table 1.5 Effect of fiber AR on the effective elastic modulus (Zeng et al., 2014).

The fiber curvature is also one of the reasons that cause the increment limit of the elastic properties of DFRC by increasing the fiber AR. Like the fiber volume fraction, the possibility of forming curved fibers in the injection molded DFRC also increases as the fiber length gets larger (Bapanapalli & Nguyen, 2008). In addition, the fiber AR may also affect the fiber orientation of the injection molded DFRC, resulting in the variation of the mechanical properties of the composites.

1.4.4 Fiber orientation effect

During the injection molding of DFRC, the fibers are suspended and oriented in the matrix. In response to the interactions of the kinematic flow, fibers will have different orientation distribution at different locations in the parts (Advani & Tucker, 1987). To investigate the effects of fiber orientation on the mechanical properties of short fiber composites, the mechanical properties of specimens (S-glass fiber reinforced PA6) with the same fiber volume fraction were tested through tensile tests (Mortazavian & Fatemi, 2015). The results are shown in Table 1.6, in which the angles represent the aligned fiber directions relative to the tensile loading direction. It is observed that the fiber orientation has a significant effect on both the stiffness and the strength of the composites.

Fiber direction	Tensile strength (MPa)	Elastic modulus (MPa)
0°	130	7330
45°	89	4500
90°	91	5050

Table 1.6 Effect of fiber orientation on the mechanical properties of a DFRC (Mortazavian & Fatemi, 2015).

Since the fiber orientation has significant effect on the mechanical properties of DFRC, it is essential to determine the fiber orientation before predicting the mechanical properties of DFRC. Experimentally, the fiber orientation can be determined by scanning electron microscopy and X-ray CT scan images. It was found that the fiber orientation distribution varies through the thickness direction of the plaque, as well as at the different locations of the plaque (Zeng et al., 2014, 2015). Based on the confocal technique and the novel image processing, the fiber orientation distribution can be determined accurately (Eberhardt et al., 2001).

Numerical modeling on the fiber orientation has been advanced for decades. The earlier study can be dated by to the early 1970's. For example, the numerical technique with the application of the Hele-Shaw flows was developed to predict the fiber orientation in the injection molded composites (Altan et al., 1971). By considering the fiber quantity and shape in the numerical simulation, the fiber orientation distribution predicted by the numerical method is consistent with that by the experimental method (Kim et al., 2001). Also, the fiber orientation distribution of the injection molded plate was measured by combining a high-resolution 3-D computed tomography system (XVA-160a) and the finite element software CIMP-PACK3DM (Thi et al., 2015). In recent years, the commercial simulation software has been developed rapidly, such as Moldflow and Modex3D. These two software packages can be used to predict the fiber orientation for the large and complex injection molded DFRC. For the Moldflow, it is possible to determine the fiber orientation variation through the thickness direction of the parts. The fiber orientation distribution predicted by the Moldflow for each layer through the thickness direction of the DFRC plaque was compared to the results determined from the CT scan image analysis, it was found that Moldflow can provide a sufficiently accurate prediction for the fiber orientation (Zeng et al., 2014, 2015). Good agreement between the experimental data and the Moldflow prediction was also confirmed by Wang et al. (2016).

To determine the fiber orientation from the theoretical perspective, there are many factors need to be considered, such as the rheology of fiber suspension and fiber interactions during the injection process (Advani & Tucker, 1987; Blanc et al., 2006; Nguyen Thi et al., 2015; Tucker & Liang, 1999b). The probability distribution function is developed to describe the

fiber orientation distribution in the injection molded composites. However, the orientation distribution function is cumbersome. Therefore, a compact orientation tensor was developed to represent the fiber orientation state. Compared to the distribution function, the orientation tensor is easier to solve, because the use of tensor does not rely on the details of the fiber motion. The orientation tensor can be written in any even order form. The higher order adopted in the orientation tensor, the more accuracy it can describe the fiber orientation state (Advani & Tucker, 1987). Figure 1.3 shows the graphic representation for three special cases of a 2nd fiber orientation tensor. Figure 1.3(a) represents the isotropic orientation state, Figure 1.3(b) is the planar isotropic state, and Figure 1.3(c) is the aligned fiber state. It can be noticed that the summation of the components in fiber orientation tensor should be unity, which means that the summation of the probability of fiber orientation is one.

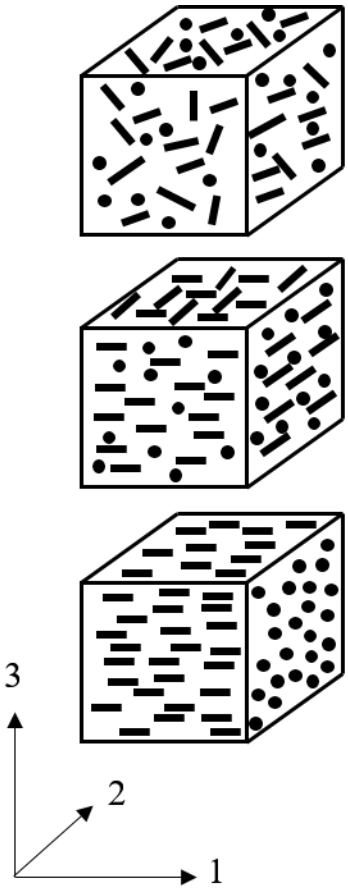

(a) 3-D random $a_{ij} = \begin{bmatrix} 1/3 & 0 & 0 \\ 0 & 1/3 & 0 \\ 0 & 0 & 1/3 \end{bmatrix}$

(b) 2-D random $a_{ij} = \begin{bmatrix} 1/2 & 0 & 0 \\ 0 & 1/2 & 0 \\ 0 & 0 & 0 \end{bmatrix}$

(c) Aligned $a_{ij} = \begin{bmatrix} 1 & 0 & 0 \\ 0 & 0 & 0 \\ 0 & 0 & 0 \end{bmatrix}$

Figure 1.3 Orientation state examples and the corresponding 2nd order orientation tensor.

In the injection molding process, the fiber orientation distribution in the DFRC is very complex, which varies with locations and through the thickness of the plaques. Such fiber distribution induces the non-uniform and anisotropic material properties of the DFRC (Zeng et al., 2014, 2015). In order to make accurate structural analysis of the DFRC parts, it is necessary to get a detailed mapping of the material properties for the DFRC. Experimental testing is a common way to determine the mechanical properties of the materials, however, it is very time consuming and expensive, particularly for the composites with complex microstructure. Therefore, we employ numerical simulation in this work to predict the mechanical properties of the DFRC, and attempt to make it more efficiently while maintaining the accuracy. In this numerical study, the potential factors that may influence the elastic properties of the DFRC will be included.

1.5 Research objective

The objective of this work is to develop an integrated software package based on micromechanics modeling and finite element analysis to predict the elastic properties of DFRC. The novelty of this work is combining the numerical and analytical solution to ensure the efficiency and accuracy of the integrated software package. Experimental testing is also performed to validate the predicted results. More efforts are focused on how to improve the accuracy of the integrated software package by considering the fiber volume fraction gradient and the fiber curvature effects. In this integrated software package, the fiber and matrix elastic properties, the fiber volume fraction, the fiber AR, the fiber orientation distribution tensor, and the fiber curvature information are the inputs. Automatic simulation can be conducted to output the elastic properties of the composites directly. The achievements in this work are summarized as the follows:

1) An integrated software package is developed to predict the elastic properties of DFRC, and the prediction shows good agreement with the data of the tensile test of the composites.
2) The fiber volume fraction gradient through the thickness direction of the DFRC plaque is determined, and the accuracy of the integrated software package is increased by considering the fiber volume fraction gradient.

3) The fiber curvature effects on the elastic properties of DFRC are investigated, and the fiber curvature is associated with the effective fiber AR to calibrate the predicted results of integrated software package.

1.6 Thesis outline

Chapter 1 gives an introduction of the composites, and states the research objectives and the thesis outline. Chapter 2 provides a detailed procedure of developing the integrated software package to predict the elastic properties of the DFRC. The fundamentals of the micromechanics modeling, the RVE model generation, the boundary conditions, the fiber orientation averaging, and the post-processing are elaborated in this chapter. Chapter 3 includes the tensile tests for verifying the accuracy of the integrated software package. Microscopy-based technique and image pixel analysis are performed to get the fiber volume fraction gradient through the thickness of the DFRC plaque. The fiber volume fraction gradient is incorporated in the numerical modeling to demonstrate its effect upon the elastic properties of the composites. The fiber curvature effect on the elastic properties of the DFRC is investigated in Chapter 4. Through data fitting, an effective fiber aspect ratio is determined to represent the fiber curvature effect. The whole thesis is concluded in Chapter 5 with the contributions and recommendations for the future work.

Chapter 2

2 An integrated software package for predicting elastic properties of DFRC

To predict the elastic properties of the DFRC, an integrated software package is developed. This integrated software package contains two modules, namely, aligned fiber module (module 1) and the orientation averaging module (module 2). In module 1, the elastic properties of the DFRC with aligned fibers are calculated by combining micromechanics modeling, finite element (FE) analysis and semi-empirical analytical solution. In module 2, with any given fiber orientation, the elastic properties of the DFRC with oriented fibers are determined by averaging the results in all directions.

2.1 Aligned fiber module

In the aligned fiber module, finite element (FE) simulation is performed to calculate the elastic properties of the DFRC with aligned fibers for different fiber aspect ratio and volume fraction. Extensive data have been collected to establish a database library. The FE prediction is more accurate than the original Halpin-Tsai equations developed for predicting the elastic properties of the DFRC with aligned fibers. However, the FE computation is more expensive, particularly for the composite with higher volume fraction and larger aspect ratio of fibers. Therefore, the collected database is used for data fitting to develop semi-empirical formulae, which are defined as the modified Halpin-Tsai equations. These semi-empirical models could ensure both efficiency and accuracy for practical applications.

2.1.1 Finite element analysis

The first part of module 1 is FE analysis on the micromechanics model, in which a representative volume element (RVE) model is developed to predict the effective elastic properties of the DFRC with aligned fibers. The FE analysis includes five main processes,

i.e., RVE generation, fiber and matrix meshing, implementation of boundary conditions for the RVE, solving process and the post processing, respectively.

These five processes in the FE analysis are achieved by Python script and the Abaqus/CAE, so that the FE analysis could be performed parametrically and automatically. Once the needed parameters are scribed in the Python and the programed script is imported into the Abaqus/CAE, the elastic properties of the DFRC with aligned fibers could be calculated and recorded in a text file. The results will be used for data fitting to get the modified Halpin-Tai equations in the next part of module 1. The Python script with the Abaqus/CAE has a great benefit of batch computation. Therefore, it is not necessary to repeat all the processes manually if some parameters, like fiber volume fraction and aspect ratio, are changed.

Case studies performed by FE analysis are for discontinuous glass fiber reinforced composites (G/DFRC) and carbon fiber reinforced composite (C/DFRC). Table 2.1 lists the mechanical properties of the fiber and matrix, and the diameter of both glass fiber and carbon fiber. To attenuate the false boundary layer effects, the size of the RVE is selected as 1.5 times of the fiber length (Liu et al., 2016).

	G/DFRC	C/DFRC
Young's modulus of fiber, E_f	75 GPa	240 GPa
Poisson's ratio of fiber, μ_f	0.25	0.22
Young's modulus of matrix, E_m	1.6 GPa	3.2 GPa
Poisson's ratio of matrix, μ_m	0.35	0.37
Diameter of fibers, d_f	25 μm	7 μm

Table 2.1. Mechanical parameters of fibers and matrix.

The fibers are aligned and randomly located in the RVE model. When creating the RVE model, the fibers are generated one by one. The program should automatically determine whether a new generated fiber overlaps with the existing fibers in the RVE. If this is the case, the new generated fiber will be relocated. The generation of the RVE without overlapping fibers is realized by developing a modified random sequential adsorption (RSA) algorithm based on the Boolean operation (Harper et al, 2012; Liu et al., 2016). The

merit of the developed algorithm is its efficiency since it avoids the looping determination of the overlapping between the new generated fiber and each pre-existing one.

After the RVE is generated with the prescribed fiber volume fraction, some fibers may over-span the RVE block. The extending part of the fibers is cut and translated to the corresponding opposite sides of the RVE in order to ensure the whole fiber is included in the RVE. Such treatment of the over-spanning fibers also keeps the geometric profiles on the opposite sides of the RVE the same. This is necessary for employing the periodic boundary conditions (PBC) in the following RVE analysis. Among the classical boundary conditions commonly used on the RVE, i.e., Dirichlet, Neumann and periodic boundary conditions, the PBC could provide a more accurate prediction on the effective elastic constants for a given RVE size (Nguyen et al., 2012), even for non-periodic materials (Abd El-Rahman & Tucker, 2013; Kanit et al., 2003; Nguyen et al., 2012; Ostoja-Starzewski, 2006). As Figure 2.1 shows below, the deformation of every point on line *a* should be the same as every point on line *b* after applying the loading. Therefore, the deformed shapes for the opposite surfaces of the RVE will be the same. In general, the PBC for the displacement field $\boldsymbol{u}$ can be written as

$$\boldsymbol{u}(\boldsymbol{x}+\boldsymbol{L}) = \boldsymbol{u}(\boldsymbol{x}) + \boldsymbol{\varepsilon}^0 \cdot \boldsymbol{x} \quad \forall \boldsymbol{x} \in \partial V \tag{2.1}$$

where $\boldsymbol{\varepsilon}^0$ is a prescribed strain field, and $\boldsymbol{L}$ is the RVE dimension.

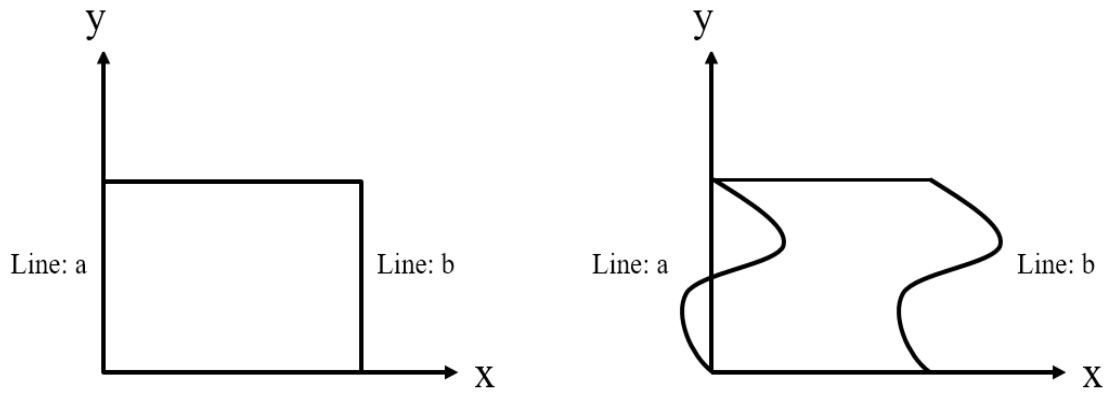

Figure 2.1 A 2-D example of periodic boundary conditions.

Before applying the PBC on the RVE model, the RVE is meshed by the direct meshing method. 8-node cube elements (C3D8R) or 4-node tetrahedron elements (C3D4) are selected for the meshing. After meshing the RVE model, the nodes' number on the opposite side surface of the RVE have to be the same, which is one of the conditions for applying the PBC. For every node *x* on one surface, the corresponding node *x+l* on the opposite side surface of the RVE model can be found. Then, these corresponding nodes on the opposite side surfaces of the RVE are coupled and constrained by Eq. (2.1) in Python. As shown by Fig. (2.1), the application of this constraint ensures that the deformation of the opposite surfaces of the RVE is the same.

The FE analysis on the RVE yields stress, strain and strain energy, while cannot predict the effective elastic properties of the RVE directly. Therefore, homogenization technique (Hill, 1963a) based on the strain energy equivalence is adopted for the RVE model to determine the effective elastic constants of the general heterogeneous materials, which requires,

$$\overline{\{\boldsymbol{\sigma}\} \cdot \{\boldsymbol{\varepsilon}\}} = \{\overline{\boldsymbol{\sigma}}\} \cdot \{\overline{\boldsymbol{\varepsilon}}\} \tag{2.2}$$

where $\{\boldsymbol{\sigma}\}$ and $\{\boldsymbol{\varepsilon}\}$ are stress and strain vectors in Voigt notation and the over bar represents the volume average for these quantities.

Thus, the effective stiffness matrix $[\boldsymbol{C}]$ of the equivalent homogenized RVE can be determined from the constitutive equations, i.e.

$$\{\,\overline{\boldsymbol{\sigma}}\,\} = [\boldsymbol{C}] \cdot \{\,\overline{\boldsymbol{\varepsilon}}\,\} \tag{2.3}$$

In general, there are 21 unknown parameters in the effective stiffness matrix $[\boldsymbol{C}]$ for a heterogeneous material. As a common practice in the homogenization technique, 21 tests with different constant strain states of the homogenized RVE are employed to determine these unknowns.

For each test, the strain energy of the equivalent homogenized volume is determined as (Ostoja-Starzewski, 2006),

$$\Phi_{homo} = \frac{V}{2}\{\bar{\boldsymbol{\sigma}}\}\cdot\{\bar{\boldsymbol{\varepsilon}}\} = \frac{V}{2}\{\bar{\boldsymbol{\varepsilon}}\}\cdot[\boldsymbol{C}]\cdot\{\bar{\boldsymbol{\varepsilon}}\} \tag{2.4}$$

where V denotes the volume of RVE. The corresponding strain energy Φ_{hetero} of the heterogeneous RVE can be expressed in terms of the stresses and strains from the FE analysis,

$$\Phi_{hetero} = \frac{V}{2}\overline{\{\sigma\}\{\varepsilon\}} = \frac{1}{2}\sum_{e=1}^{M}\left(\int_{Ve}\sigma_{ij}\varepsilon_{ij}dV\right) \tag{2.5}$$

where M is the total number of elements in the FE model.

Particularly, for the RVE with aligned fibers, the material is transversely isotropic, resulting in 5 independent constants in the stiffness matrix. These constants will be determined from 5 tests. It is assumed that all the fibers are aligned in the direction "3 (Z)" in the RVE, therefore, the mechanical properties of the RVE is isotropic in 1-2 (X-Y) plane. The stiffness matrix is simplified as,

$$C_{KM} = \begin{bmatrix} C_{11} & C_{12} & C_{13} & 0 & 0 & 0 \\ & C_{11} & C_{13} & 0 & 0 & 0 \\ & & C_{33} & 0 & 0 & 0 \\ & & & C_{44} & 0 & 0 \\ & & & & C_{44} & 0 \\ Sym. & & & & & 1/2(C_{11}-C_{12}) \end{bmatrix} \tag{2.6}$$

For Test 1, the strain energy of the equivalent homogenized volume under a prescribed strain field $\{\bar{\varepsilon}\} = \{\varepsilon_1^0\,0\,0\,0\,0\}^T$ is determined as,

$$\Phi_{homo} = \frac{V}{2}C_{11}(\varepsilon_1^0)^2 \tag{2.7}$$

Thus C_{11} in the stiffness matrix is thus obtained according to the strain energy equivalence $\Phi_{homo} = \Phi_{hetero}$, i.e., $C_{11} = 2\Phi_{hetero}/[V(\varepsilon_1^0)^2]$. Similarly, the other material constants in the stiffness matrix can also be determined, which is not demonstrated here for simplicity purpose. Such common practice for the homogenization technique is well elaborated in the literature (Hill, 1963b)

Once the material constants in the stiffness matrix are determined, the compliance matrix of the RVE can also be obtained as shown in Eq. (2.8). It should be noticed that the subscribe "*L*" and "*T*" means the longitudinal and transverse direction, respectively. "*L*" direction is also the fiber alignment direction. From the compliance matrix, the Young's modulus, Poisson's ratio and shear modulus of the material can be extracted, i.e.,

$$[\mathbf{S}] = [\mathbf{C}]^{-1} = \begin{bmatrix} \frac{1}{E_T} & -\frac{\mu_{TT}}{E_T} & -\frac{\mu_{LT}}{E_T} & 0 & 0 & 0 \\ -\frac{\mu_{TT}}{E_T} & \frac{1}{E_T} & -\frac{\mu_{LT}}{E_L} & 0 & 0 & 0 \\ -\frac{\mu_{LT}}{E_L} & -\frac{\mu_{LT}}{E_L} & \frac{1}{E_L} & 0 & 0 & 0 \\ 0 & 0 & 0 & \frac{1}{G_{LT}} & 0 & 0 \\ 0 & 0 & 0 & 0 & \frac{1}{G_{LT}} & 0 \\ 0 & 0 & 0 & 0 & 0 & \frac{1}{G_{TT}} \end{bmatrix} \tag{2.8}$$

To improve the accuracy of the FE analysis, the results are calculated by averaging five sets of data.

2.1.2 Semi-empirical formulae - modified Halpin-Tsai equations

Based on self-consistent micromechanics model, the Halpin-Tsai equations are developed in an analytical format to predict the elastic properties of the composite materials. Those equations are empirical with approximations, which could provide quite accurate results on the elastic properties for the composites over a certain range of fiber volume fraction (Halpin & Kardos, 1976; Liu et al., 2016; Younes et al., 2012).

In general, the Halpin-Tsai equations for Young's modulus and shear modulus of the composites with aligned fibers can be expressed as (Halpin & Kardos, 1976)

$$\frac{E}{E_m} = \frac{1 + \xi\eta V_f}{1 - \eta V_f} \tag{2.9}$$

where V_f is the fiber volume fraction, E represents the elastic constants, including E_T, E_L, G_{TT} and G_{LT} in Eq. (2.8). The subscript "m" denotes the quantities for polymer matrix, and parameter η in Eq. (2.10) is represented by,

$$\eta = \frac{E_f/E_m - 1}{E_f/E_m + \xi} \tag{2.10}$$

The subscript "f" represents the quantities for fiber. The factor ξ is used to describe the influence of the geometry of the reinforcing phase with the values given below,

$$\xi = 2 \qquad (for\ E_T) \tag{2.11a}$$

$$\xi = AR \qquad (for\ E_L) \tag{2.11b}$$

$$\xi = \frac{1 + \mu_m}{3 - \mu_m - 4\mu_m^2} \quad (for\ G_{TT}) \tag{2.11c}$$

$$\xi = 1 \qquad (for\ G_{LT}) \tag{2.11d}$$

Other constants in the compliance matrix can be determined by:

$$\mu_{LT} = \mu_f V_f + \mu_m(1 - V_f), \mu_{TT} = \frac{E_T}{2G_{TT}} - 1 \tag{2.12}$$

where μ_f and μ_m are the Poisson's ratio of fiber and matrix respectively.

Case study is conducted on the carbon fiber reinforced composite with different volume fraction and fiber aspect ratio. The results from the prediction by both Halpin-Tsai equations and Mori-Tanaka method for the longitudinal Young's modulus are compared with the numerical FE simulation as shown in Figure 2.2. Similar to Halpin-Tsai equations, the Mori-Tanaka equations predict the stiffness and compliance tensors based on the self-consistency theory (Benveniste, Y., 1987).

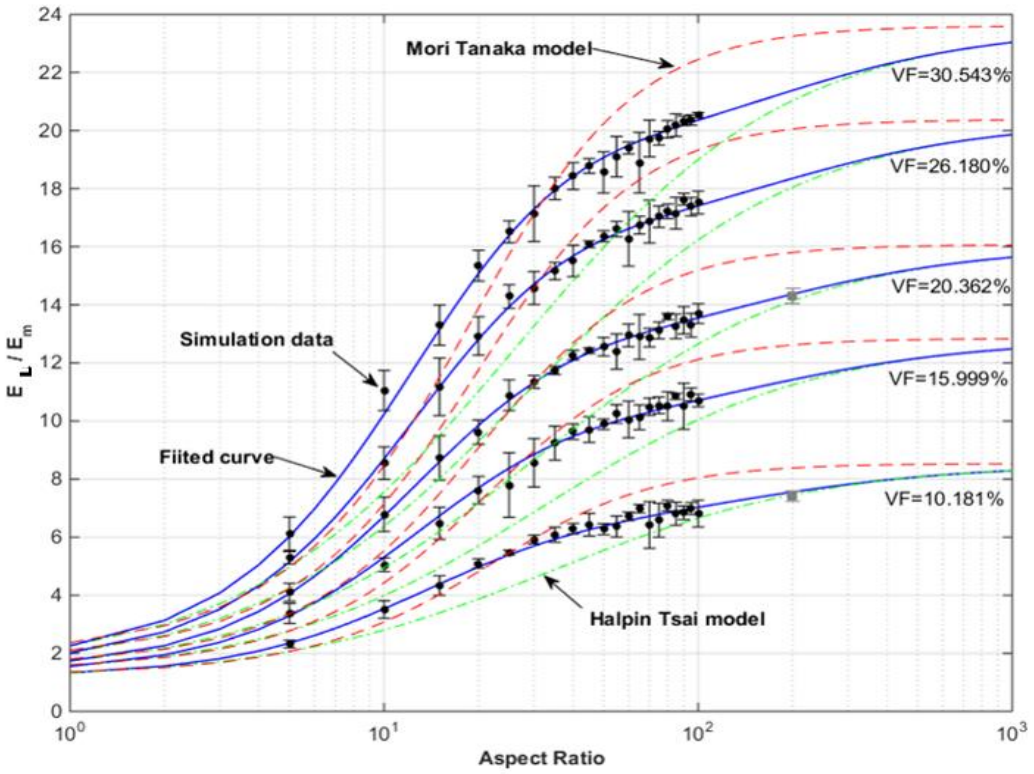

Figure 2.2 The comparison of the numerical results for the longitudinal Young's modulus with Halpin-Tsai and the Mori-Tanaka prediction.

It is obvious to observe the discrepancy between the Halpin-Tsai model and the numerical results, particularly when the fiber aspect ratio falls in the range of 10~150, which is a typical fiber aspect ratio for the injection molded composites. It is thus concluded that the Halpin-Tsai equations may not be accurate to predict the elastic constants for the injection molded DFRC with aligned fibers, which needs further modification. By fitting the results from the FE analysis, the modified Halpin-Tsai equations are developed. ς is determined to replace ξ in Eqs. (2.11a), (2.11c) and (2.11d), while Eq. (2.9) still keeps the same format. The only exception is for the longitudinal Young's modulus, which is replaced by Eq. (2.13b). These modified Halpin-Tsai equations are summarized as the follows:

$$\zeta = 2.15 \qquad (for\ E_T) \qquad (2.13a)$$

$$\frac{E_L}{E_m} = \frac{1+\zeta\eta V_f}{1-\eta V_f} + \frac{\alpha\left(E_f/E_m - 1\right)\left[V_f\left(1-V_f\right)\right]^{\delta}}{\beta\zeta} e^{-(ln(\zeta)-\gamma)^2/(2\beta^2)}, \zeta = AR \qquad (2.13b)$$

$$\zeta = 2.69V_f + 0.74 \qquad (for\ G_{TT}) \qquad (2.13c)$$

$$\zeta = 3.28V_f + 1.10 \qquad (for\ G_{LT}) \qquad (2.13d)$$

Comparing with the original equations, the modified Halpin-Tsai equations provides the corrections term. For example, in the expression of the longitudinal Young's modulus, the second term is the correction factor. By fitting with the FE analysis results in the database library, the four correction coefficients α, β, γ, and δ are determined as 22.33, 0.95, 4.09,1.55 respectively. It should be noted, if the material properties are changed, the parameters in the modified Halpin-Tsai equations will change accordingly.

In this module, if the material properties for the matrix and reinforcement are given as the input, FE analysis will be automatically conducted to collect extensive data to establish a library. The database in the library will be used for data fitting to get the modified Halpin-Tsai equations for this composite. Therefore, for any input aspect ratio and volume fraction, the elastic constants of such composite with aligned fibers will be automatically calculated through this module.

2.2 Orientation averaging module

From the previous analysis, it is concluded that Module 1 combines the accuracy of the FE simulation and the efficiency of the semi-empirical formulation. However, this module can be only used to predict the elastic constants of composites with aligned fibers. For general injection molded DFRC, the fibers are distributed in the polymer matrix with orientation. Therefore, a 2nd module is needed to develop to determine the elastic constants of the composites through orientation averaging.

In the orientation averaging module, the elastic properties calculated by module 1 and the fiber orientation tensor simulated by Moldflow (or Moldex3D) are the two inputs. There

are three steps in this module, including closure approximation, orientation averaging, and coordinate transformation.

The orientation averaging requires not only the elastic properties for the composites with aligned fibers, but the 4th order fiber orientation tensor as well. However, the fiber orientation tensor from the Moldflow simulation is 2nd order. Therefore, the closure approximation method is used to get an approximation of the 4th order orientation tensor first. After the 4th order fiber orientation tensor is determined, the orientation average method is used to calculate the 4th order stiffness matrix of the composites in the material principal directions. Then, the stiffness matrix for the composite with oriented fibers in the material principal directions will be converted to the 2nd order stiffness matrix. Next, the stiffness matrix in the material principal directions will be further transferred to the one in the global coordinate system.

2.2.1 Orientation distribution function

As shown in Figure 2.3, the orientation state of a fiber with length l and diameter d is described by two Euler angles φ and θ in the *xyz* coordinate system or by a vector **p**. It is commonly assumed that the orientation distribution function is a complete description of the fiber orientation state in the literature (Advani & Tucker, 1987), which is prescribed as $\psi(\theta,\phi)$ or $\psi(\mathbf{p})$. The components of the unit vector **p** can be directly related to θ and ϕ, i.e.,

$$p_1 = \sin\theta\cos\phi \tag{2.13a}$$

$$p_2 = \sin\theta\sin\phi \tag{2.13b}$$

$$p_3 = \cos\theta \tag{2.13c}$$

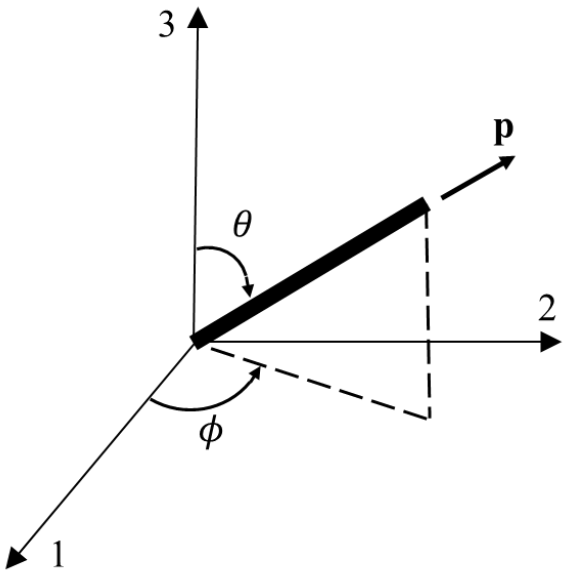

Figure 2.3 Fiber orientation representation.

The orientation distribution function must satisfy three physical conditions. The first one is the periodic condition, which can be expressed as,

$$\psi(\theta, \phi) = \psi(\pi - \theta, \phi + \pi) \tag{2.14}$$

$$\psi(\mathbf{p}) = \psi(-\mathbf{p}) \tag{2.15}$$

The second one is the normalization condition,

$$\int_{\theta=0}^{\pi} \int_{\phi=0}^{2\pi} \psi(\theta, \phi) \sin\theta \, d\theta \, d\phi = \oint \psi(\mathbf{p}) \, d\mathbf{p} = 1 \tag{2.16}$$

And the third condition is the continuity condition which describes the changes in the function $\psi(\mathbf{p})$ with time when fibers are moving, i.e.,

$$\frac{D\psi}{Dt} = -\frac{\forall}{\forall \mathbf{p}} (\psi \dot{\mathbf{p}}) \tag{2.17}$$

where $\forall / \forall P$ is the gradient operator on the surface of the unit sphere. With the selected average fiber angular velocities, ($\dot{\theta}$ and $\dot{\phi}$), this condition provides a way to determine the evolution of ψ with time.

As mentioned in the previous section, the Moldflow (or Moldex3D) simulation outputs the 2nd orientation tensor a_{ij} directly. This tensor is related to the orientation distribution function through the following expression (Advani & Tucker, 1987),

$$a_{ij} = \oint p_i p_j \psi(\mathbf{p})\, d\mathbf{p} \tag{2.18}$$

Similarly, the 4th order orientation tensors (a_{ijkl}) is defined as (Advani & Tucker, 1987),

$$a_{ijkl} = \oint p_i p_j p_k p_l \psi(\mathbf{p})\, d\mathbf{p} \tag{2.19}$$

It should be noted that the odd-order orientation tensors are zero since the distribution function is an even function. Due to the symmetry and normalization conditions of the orientation tensors, the independent components for the 2nd order and 4th order tensors could be reduced to five and fourteen, respectively.

In general, the fiber distribution function should be determined from the orientation tensor. This is realized by starting the expression of $\psi(\mathbf{p})$ in Fourier representation, i.e., (Advani & Tucker, 1987)

$$\psi(\mathbf{p}) = \psi_0 + \psi_{ij} f_{ij}(\mathbf{p}) + \psi_{ijkl} f_{ijkl}(\mathbf{p}) + \cdots \qquad (i, j, k, l \ldots = 1,2,3) \tag{2.20}$$

where f_{ij}, f_{ijkl} are the basis functions, i.e.,

$$f_{ij}(\mathbf{p}) = p_i p_j - \frac{1}{3}\delta_{ij} \tag{2.21a}$$

$$f_{ijkl}(\mathbf{p}) = p_i p_j p_k p_l - \frac{1}{7}(\delta_{ij} p_k p_l + \delta_{ik} p_j p_l + \delta_{il} p_j p_k + \delta_{jk} p_i p_l + \delta_{jl} p_i p_k + \delta_{kl} p_i p_j) + \frac{1}{35}(\delta_{ij}\delta_{kl} + \delta_{ik}\delta_{jl} + \delta_{il}\delta_{jk}) \tag{2.21b}$$

and

$$\psi_0 = \frac{1}{4\pi}\oint \psi(\mathbf{p})\, d\mathbf{p} \tag{2.22a}$$

$$\psi_{ij} = \frac{1}{4\pi} \cdot \frac{3 \times 5}{2} \oint \psi(\mathbf{p}) f_{ij}(\mathbf{p})\, d\mathbf{p} \tag{2.22b}$$

$$\psi_{ijkl} = \frac{1}{4\pi} \cdot \frac{3 \times 5 \times 7 \times 9}{2 \times 3 \times 4} \oint \psi(\mathbf{p}) f_{ijkl}(\mathbf{p})\, d\mathbf{p} \tag{2.22c}$$

According to the normalization condition of the distribution function, and the definition of the orientation tensor a_{ij} in Eq. (2.18), the distribution function becomes:

$$\psi(\mathbf{p}) = \frac{1}{4\pi} + \frac{15}{8\pi} b_{ij} f_{ij}(\mathbf{p}) + \frac{315}{32\pi} b_{ijkl} f_{ijkl}(\mathbf{p}) + \ldots \tag{2.23}$$

With the deviatoric versions of the orientation tensors defined as,

$$b_{ij} = a_{ij} - \frac{1}{3}\delta_{ij} \tag{2.24a}$$

$$b_{ijkl} = a_{ijkl} - \frac{1}{7}(\delta_{ij}a_{kl} + \delta_{ik}a_{jl} + \delta_{il}a_{jk} + \delta_{jk}a_{il} + \delta_{jl}a_{ik} + \delta_{kl}a_{ij}) + \frac{1}{35}(\delta_{ij}\delta_{kl} + \delta_{ik}\delta_{jl} + \delta_{il}\delta_{jk}) \tag{2.24b}$$

Certainly, the orientation distribution function can also be expanded with higher orders. However, the computational cost of the fiber distribution function $\psi(\boldsymbol{p})$ is expensive. It should also be noted that the 4th order orientation tensor a_{ijkl} should be determined, which will be outlined in the next section.

2.2.2 Closure approximation

For a given 2nd order orientation tensor from Moldflow (or Moldex3D) simulation, the 4th order (or even higher order) orientation tensor can be obtained by the closure approximation methods. In the literature, efforts have been made to develop those methods, including two hybrid closure approximations (Advani & Tucker, 1987, 1990), orthotropic closure approximations (Cintra & Tucker, 1995), improved model of orthotropic closure approximations (Chung & Kwon, 2001), weighting method approximations (Doghri &

Tinel, 2006), and invariant-based optimal fitting (IBOF) approximations (Chung & Kwon, 2002). Based on the natural closure approximation and the orthotropic closure approximation (Cintra & Tucker, 1995; Dupret & Verleye, 1999), the eigenvalue-based optimal fitting (EBOF) and IBOF were developed by Chung & Kwon (2002). There is no obvious difference of the accuracy for IBOF and EBOF, but computation cost for IBOF is much less than the EBOF approximation method. It should be noted that the closure approximation should be constructed following several guidelines. Firstly, the closure approximation should be constructed from the lower order and the unit tensor. Secondly, the transferred higher order orientation tensor must satisfy the normalization condition. Thirdly, the symmetry property of the orientation tensor should be remained after the closure approximation. We have compared all these methods in recovering the fiber orientation distribution function and found that IBOF method is sufficiently accurate for our case. It is also concluded that the accuracy and the efficiency of the IBOF method are acceptable by Chung & Kwon (2002). Therefore, the IBOF method is selected to approximate the 4th order tensor in the integrated software package.

The 4th order orientation tensor can be expressed by using IBOF as:

$$\begin{aligned} a_{ijkl} = \beta_1 S(\delta_{ij}\delta_{kl}) + \beta_2 S(\delta_{ij}a_{kl}) + \beta_3 S(a_{ij}a_{kl}) + \beta_4 S(\delta_{ij}a_{km}a_{ml}) \\ + \beta_5 S(a_{ij}a_{km}a_{ml}) + +\beta_6 S(a_{im}a_{mj}a_{kn}a_{nl}) \end{aligned} \tag{2.25}$$

where the operator S denotes the symmetric part of a tensor, for example:

$$S(a_{ij}) = \frac{1}{2}(a_{ij} + a_{ji}) \tag{2.26}$$

The coefficients β_i are calculated in terms of the invariants of the 2nd order orientation tensor, i.e.,

$$\begin{aligned}\beta_i = {} & pa(i,1) + pa(i,2)\mathrm{II} + pa(i,3)\mathrm{II}^2 + pa(i,4)\mathrm{III} + pa(i,5)\mathrm{III}^2 \\ & + pa(i,6)\mathrm{II}\cdot\mathrm{III} + pa(i,7)\mathrm{II}^2\cdot\mathrm{III} + pa(i,8)\mathrm{II}\cdot\mathrm{III}^2 \\ & + pa(i,9)\mathrm{II}^3 + pa(i,10)\mathrm{III}^3 + pa(i,T)\mathrm{II}^3\cdot\mathrm{III} + pa(i,12)\mathrm{II}^2 \\ & \cdot\mathrm{III}^2 + pa(i,13)\mathrm{II}\cdot\mathrm{III}^3 + pa(i,14)\mathrm{II}^4 + pa(i,15)\mathrm{III}^4 \\ & + pa(i,16)\mathrm{II}^4\cdot\mathrm{III} + pa(i,17)\mathrm{II}^3\cdot\mathrm{III}^2 + pa(i,18)\mathrm{II}^2\cdot\mathrm{III}^3 \\ & + pa(i,19)\mathrm{II}\cdot\mathrm{III}^4 + pa(i,20)\mathrm{II}^5 \\ & + pa(i,21)\mathrm{III}^5 \qquad (i=3,4,6)\end{aligned} \tag{2.27}$$

Where I, II and III are the invariants of the 2nd order orientation tensor, which can be expressed in terms of the three eigenvalues (λ_1, λ_2 and λ_3) of the fiber orientation tensor a_{ij}, i.e.,

$$\mathrm{I} = \lambda_1 + \lambda_2 + \lambda_3 \tag{2.28a}$$

$$\mathrm{II} = \lambda_1\lambda_2 + \lambda_2\lambda_3 + \lambda_3\lambda_1 \tag{2.28b}$$

$$\mathrm{III} = \lambda_1\lambda_2\lambda_3 \tag{2.28c}$$

The values of $pa(i,j)$ are provided in Appendix A . After the independent coefficients β_3 , β_4 and β_6 have been determined, the next step is to calculate the coefficients β_1, β_2 and β_5 as,

$$\begin{aligned}\beta_1 = \frac{3}{5}\Big[& -\frac{1}{7} + \frac{1}{5}\beta_3\left(\frac{1}{7} + \frac{4}{7}\mathrm{II} + \frac{8}{3}\mathrm{III}\right) - \beta_4\left(\frac{1}{5} - \frac{8}{15}\mathrm{II} - \frac{14}{15}\mathrm{III}\right) \\ & - \beta_6\left(\frac{1}{35} - \frac{4}{35}\mathrm{II} - \frac{24}{105}\mathrm{III} + \frac{16}{15}\mathrm{II}\cdot\mathrm{III} + \frac{8}{35}\mathrm{II}^2\right)\Big]\end{aligned} \tag{2.29a}$$

$$\beta_2 = \frac{6}{7}\left[1 - \frac{1}{5}\beta_3(1 + 4\mathrm{II}) + \frac{7}{5}\beta_4\left(\frac{1}{6} - \mathrm{II}\right) - \beta_6\left(-\frac{1}{5} + \frac{4}{5}\mathrm{II} + \frac{2}{3}\mathrm{III} - \frac{8}{5}\mathrm{II}^2\right)\right] \tag{2.29b}$$

$$\beta_5 = -\frac{4}{5}\beta_3 - \frac{7}{5}\beta_4 - \frac{6}{5}\beta_6\left(1 - \frac{4}{3}\mathrm{II}\right) \tag{2.29c}$$

If higher order terms are needed in the fiber orientation distribution function $\psi(\mathbf{p})$ in Eq. (2.23), the higher order orientation tensor, for example, the 6th order or even higher order, could be determined in a similar way by choosing appropriate closure approximation.

2.2.3 Orientation averaging

The orientation averaging method is used to predict the elastic stiffness for the composites with oriented fibers, which are described by the orientation tensor. Consider a general 4th order stiffness tensor **C** associated with the composites reinforced by aligned fibers in the direction of **p**, the orientation average of **C** denoted by $\langle \mathbf{C} \rangle$ is defined as (Advani & Tucker, 1987),

$$\langle \mathbf{C} \rangle = \oint \mathbf{C}(\mathbf{p})\psi(\mathbf{p})d\mathbf{p} \tag{2.30}$$

For the tensor **C** to be transversely isotropic about the direction **p**, the tensor must have the following format (Advani & Tucker, 1987),

$$\begin{aligned} C_{ijkl}(p) = {} & B_1(p_i p_j p_k p_l) + B_2(p_i p_j \delta_{kl} + p_k p_l \delta_{ij}) + \\ & B_3(p_i p_k \delta_{jl} + p_i p_l \delta_{jk} + p_j p_l \delta_{ik} + p_j p_k \delta_{il}) + B_4(\delta_{ij}\delta_{kl}) + B_5(\delta_{ik}\delta_{jl} + \delta_{il}\delta_{jk}) \end{aligned} \tag{2.31}$$

where B_i are five scalar constants, related to the five independent components of the stiffness tensor C_{KM} in as shown in Eq. (2.6), i.e.,

$$B_1 = C_{33} + C_{11} - 2C_{13} - 4C_{44} \tag{2.32a}$$

$$B_2 = C_{13} - C_{12} \tag{2.32b}$$

$$B_3 = C_{44} + \frac{1}{2}(C_{12} - C_{11}) \tag{2.32c}$$

$$B_4 = C_{12} \tag{2.32d}$$

$$B_5 = \frac{1}{2}(C_{11} - C_{12}) \tag{2.32e}$$

After the integration by Eq. (2.30), the orientation average of the 4th order stiffness matrix **C** is determined as (Advani & Tucker, 1987),

$$\begin{aligned} < C_{ijkl} >= & B_1(a_{ijkl}) + B_2(a_{ij}\delta_{kl} + a_{kl}\delta_{ij}) \\ & + B_3(a_{ik}\delta_{jl} + a_{il}\delta_{jk} + a_{jl}\delta_{ik} + a_{jk}\delta_{il}) + B_4(\delta_{ij}\delta_{kl}) \\ & + B_5(\delta_{ik}\delta_{jl} + \delta_{il}\delta_{jk}) \end{aligned} \tag{2.33}$$

Therefore, the orientation averaging through the orientation distribution function has been converted in terms of the orientation tensor, which gives the stiffness constants of the composites with oriented fibers. It should be noted that the stiffness constants determined here are associated with the principal directions of the orientation tensor, i.e., the material principal directions. Therefore, we use $[C_{ijkl}]_p$ to replace $\langle C_{ijkl} \rangle$.

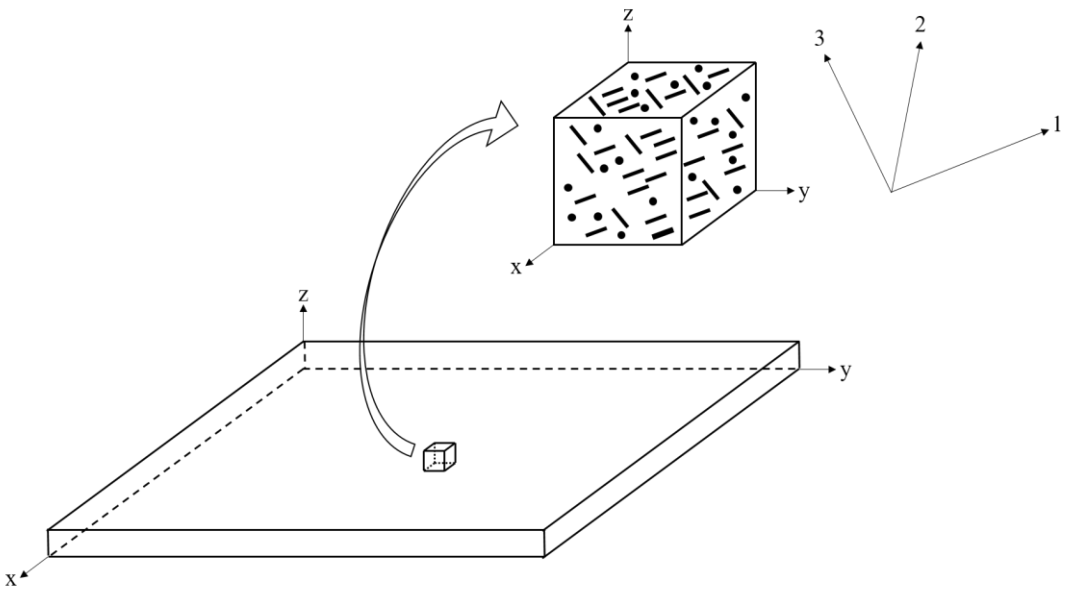

Figure 2.4 Illustration of the global and the local coordinate systems for the material.

2.2.4 Coordinate transformation

Before we do the coordinate transformation from the local coordinate system (associated with the material principal directions) to the global coordinate system, the averaged elastic stiffness $[C_{ijkl}]_p$ for the composite with oriented fibers is degraded to a 6×6 2nd order

tensor$[C_{KM}]_p$ in the Voigt notation. Figure 2.4 shows the illustration of the global and local coordinate system, the material properties in the global coordinate system (x-y-z) are calculated from the material properties $[C_{KM}]_p$ in the local coordinate system (1-2-3).

Eigenvalue analysis is performed to determine the eigenvalues (λ_1, λ_2 and λ_3) and eigenvectors ($\overrightarrow{e_1}$, $\overrightarrow{e_2}$ and $\overrightarrow{e_3}$) of the orientation tensor a_{ij}. Thus the transformation tensor $[l]$ between the coordinate associated with material principal directions and the global coordinate system is determined as (Ting, 1996),

$$[l] = [\overrightarrow{e_1}\ \overrightarrow{e_2}\ \overrightarrow{e_3}] \tag{2.34}$$

which is the eigenvector matrix. Performing both stress and strain transformation and using the Hooke's Law, the stiffness matrix in the global coordinate system can be expressed as (Ting, 1996),

$$[C] = [M]^{-1}[C]_p[[M]^T]^{-1} \tag{2.35}$$

where $[M]$ can be determined by,

$$[M] = \begin{bmatrix} M_1 & M_2 \\ M_3 & M_4 \end{bmatrix} \tag{2.36a}$$

$$M_1 = \begin{bmatrix} {l_{11}}^2 & {l_{21}}^2 & {l_{31}}^2 \\ {l_{12}}^2 & {l_{22}}^2 & {l_{32}}^2 \\ {l_{13}}^2 & {l_{23}}^2 & {l_{33}}^2 \end{bmatrix} \tag{2.36b}$$

$$M_2 = \begin{bmatrix} 2l_{21}l_{31} & 2l_{31}l_{11} & 2l_{21}l_{11} \\ 2l_{22}l_{32} & 2l_{12}l_{32} & 2l_{12}l_{22} \\ 2l_{23}l_{33} & 2l_{13}l_{33} & 2l_{13}l_{23} \end{bmatrix} \tag{2.36c}$$

$$M_3 = \begin{bmatrix} l_{12}l_{13} & l_{22}l_{23} & l_{32}l_{33} \\ l_{11}l_{13} & l_{21}l_{23} & l_{31}l_{33} \\ l_{11}l_{12} & l_{21}l_{22} & l_{31}l_{32} \end{bmatrix} \tag{2.36d}$$

$$M_4 = \begin{bmatrix} l_{22}l_{33} + l_{32}l_{23} & l_{12}l_{33} + l_{32}l_{13} & l_{12}l_{23} + l_{22}l_{13} \\ l_{21}l_{33} + l_{31}l_{23} & l_{11}l_{33} + l_{31}l_{13} & l_{11}l_{23} + l_{21}l_{13} \\ l_{21}l_{32} + l_{31}l_{22} & l_{11}l_{32} + l_{31}l_{12} & l_{11}l_{22} + l_{21}l_{12} \end{bmatrix} \tag{2.36e}$$

with l_{ij} defined as the components in eigenvector matrix [l] in Eq.(2.34).

Up to now, two modules of the integrated software package have been completed. Module 1 predicts the elastic properties for the composites with aligned fibers, while module 2 transfers the results in the 1st module to the composite with oriented fibers in the global coordinate system if the orientation tensor representing the fiber distribution is provided. The numerical simulation results will be compared with the experimental data for validation purpose in the next Chapter.

Chapter 3

3 Experiments

In order to validate the prediction results from the integrated software package developed in the previous Chapter, standard tensile tests (ISO 527-4) are performed on the DFRC samples for comparison. Discrepancy is found between the numerical simulation results and the tensile test results. One of the possible error resources may come from the non-uniform distribution of the fibers through the sample thickness direction. Therefore, various methodologies are attempted to determine the fiber volume fraction gradient through the sample thickness. Firstly, burn-off (ASTM D2584) tests are conducted through thermal gravimetric analysis (TGA*)* experiments. However, due to the lack of knowledge and the limitation of the experimental equipment, the burn-off tests could not provide the reliable results since the measured fiber volume fraction is much lower than the theoretical value. An alternative method, the microscopy-based technique combined with grinding and polishing processes is performed to determine the fiber volume fraction distribution through the sample thickness.

The determined fiber volume fraction gradient is then imported into the integrated software package to determine the effective elastic constants of the sample. The details of all these tests are outlined in the following sections.

3.1 Tensile tests

To verify the accuracy of the developed integrated software package, tensile tests for several locations on the DFRC plaque are carried out at Ford Research and Innovation Center. Those tensile tests are conducted on a hydraulic MTS machine coupled with a Digital Image Correlation (DIC) system. The specifications of the tested DFRC samples are listed in Table 3.1. Both G/DFRC and C/DFRC samples are tested with two sets of different volume fractions, and the corresponding weight fractions are also provided in this table.

Fiber type	Fiber VF	Fiber WF	Number of specimen locations
Glass fiber	10%	20%	3
	15%	30%	3
Carbon fiber	16%	20%	6
	30%	40%	6

Table 3.1 The specifications of the DFRC plaque for tensile test.

The cutting strategy for the G/DFRC plaque is shown in Figure 3.1, in which three types of specimens are cut in the middle of the plaque along 0º, 45º and 90º directions, respectively. The dimension and the configuration of the specimen are demonstrated in Figure 3.2(a), which follows the standards of (ISO 527-4). The analyzed area by DIC system is in the middle of the specimen as shown in Figure 3.2(a), and the corresponding mapping result is demonstrated in Figure 3.2(b).

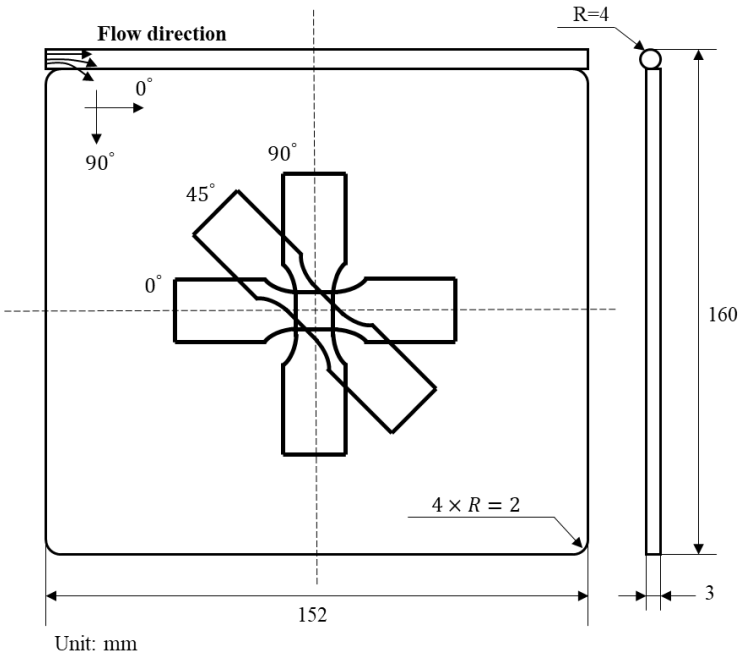

Figure 3.1 Specimen cutting strategies for G/DFRC plaque.

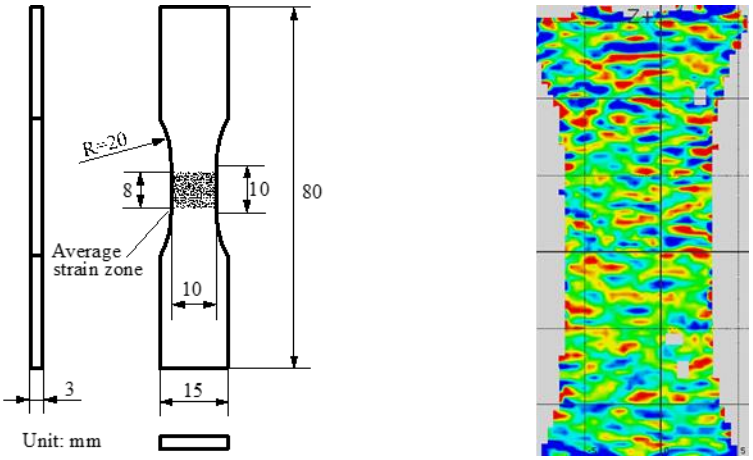

(a) Dimension of specimen (b) DIC mapping of specimen

Figure 3.2 (a) The dimension of the specimen, for both C/DFRC and G/DFRC; (b) The DIC mapping example for one of the specimens.

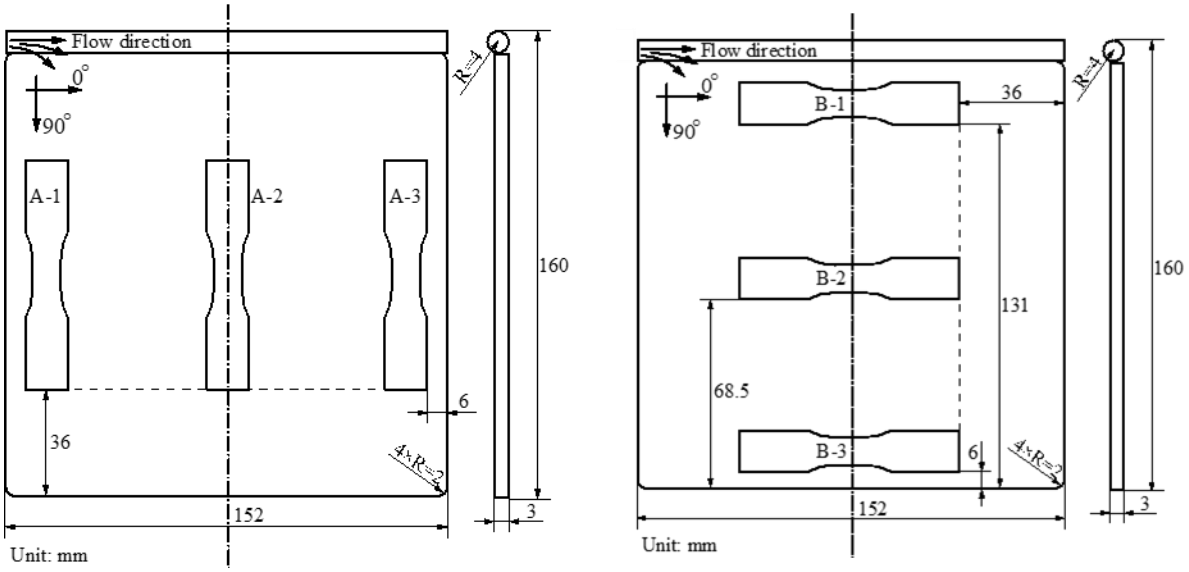

(a) Cutting strategy A (b) Cutting strategy B

Figure 3.3 Specimen cutting strategies for C/DFRC plaque.

For the C/DFRC plaques, the specimens are cut at different locations along 0º and 90º directions, as shown in Figure 3.3. The specimen size and DIC mapping zone are the same as for the G/DFRC. For both G/DFRC and C/DFRC samples, three specimens are cut in the same location to repeat the testing, and the longitudinal modulus is determined by averaging these three sets of tensile testing results.

After the tensile tests for both the G/DFRC and the C/DFRC samples have been done, the testing data are compared with the results predicted by the integrated software package, which will be shown in the later section. It is found that for the G/DFRC material, the integrated software package prediction agrees well with the tensile testing data. However, for the C/DFRC samples, the error is higher than the G/DFRC case, even more than 10% for some locations. Therefore, it is necessary to investigate the source of the errors. In addition to the accuracy of the Moldflow (or Moldex3D), there are some other possibilities, e.g., the fiber volume fraction variation and the fiber actual aspect ratio. As the first step of our numerical simulation, these two parameters are set as constant input values in the integrated software package. Particularly, for the composites from the injection molding, it is commonly accepted that the fiber volume fraction is not uniform along the thickness direction, which will have a gradient. From the CT scan images and Moldflow simulation (Zeng et al., 2014, 2015) of an injection molded sample, it is observed that most fibers are oriented at in plane direction with more fibers concentrated in the middle part, clearly demonstrating a skin-core structure. Therefore, this Chapter will focus on determining the fiber volume fraction gradient and investigating such gradient effect upon the elastic constants of the DFRC.

3.2 Burn-off test

There are two standard methods (ASTM D2584 and ASTM D3171) commonly used to determine the fiber volume fraction in the composite materials. The ASTM D2584 involves the matrix burning off, while the ASTM D3171 use the chemical digestion of the polymer matrix (ASTM International, 2010a; Mcdonough et al., 2004). Because of the experimental equipment is not available for the ASTM D3171 standard, the burn-off experiment is attempted in this work. Firstly, the weight of the C/DFRC specimens is measured at the room temperature. Then, the specimens are placed in the crucibles, which are put in the thermal gravimetric analysis (TGA) heated up to a certain temperature where the matrix would be burnt off, but with the fibers remained in the stable form. After a certain time, all the matrix should be removed from the crucible, and the fibers should be cooled down to the room temperature. Next, the weight of fibers is measured to determine the fiber weight fraction, which could be further used to determine the fiber volume fraction.

Before the burn-off experiment, the specimens need to be cut from the C/DFRC plaque. Figure 3.4 and 3.5 shows the detailed positions and the dimensions of the specimens and images. Similar to the tensile tests, two sets of specimens are prepared with fiber weight fraction of 20 % and 40 %, respectively. The corresponding fiber volume fraction is 16 % and 30 %, respectively.

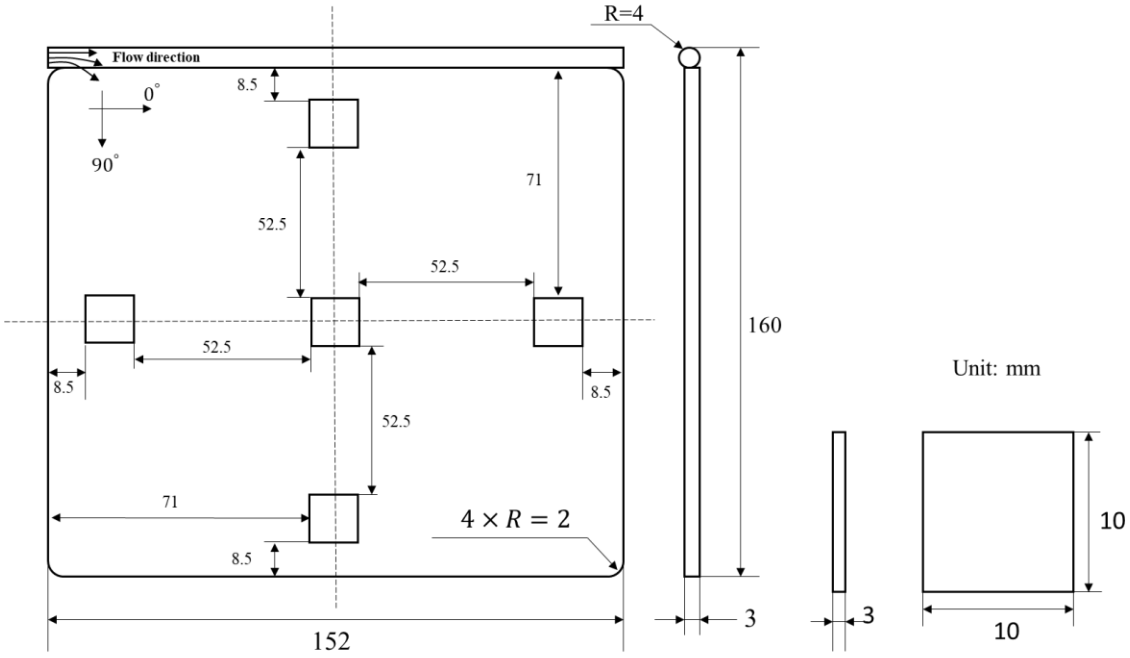

Figure 3.4 C/DFRC plaque and specimen configuration.

Figure 3.5 Image of specimen and C/DFRC plaque.

In the burn-off test, the goal is to find the gradient of fiber volume fraction through the thickness direction. Therefore, the tested specimen should represent the typical layers through the thickness direction. As shown in Figure 3.6, each specimen is divided into three layers (skin-core-skin). The thickness of the two skin layers is assumed as the same, with the thickness of the skin layer being 40% and the core layer being 20% of the whole specimen. Therefore, the fiber weight fraction for the core layer could be calculated after determining the fiber weight fraction for one skin layer. Both the original specimens and the ground specimens will be tested.

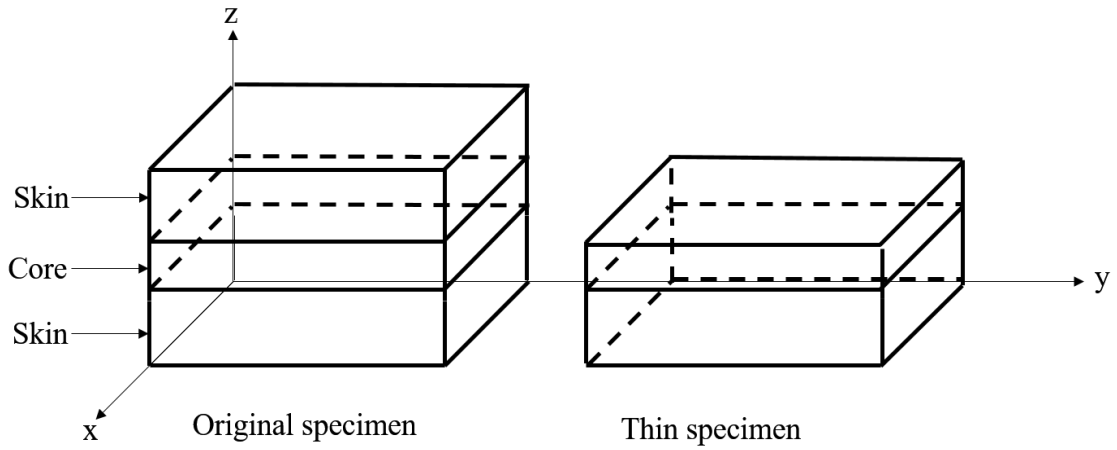

Figure 3.6 Skin-core-skin configuration for the burn-off test.

The next step is grinding the specimen. As the first attempt, only one skin layer is removed in this process. As shown in Figure 3.7, the mounted specimen is firstly ground with coarse sandpaper to remove most thickness of the skin-layer. Then, the higher grit sandpaper is used to obtain the smoothing surface. Table 3.2 shows the detailed dimension of the specimens with and without grinding. There are 20 specimens in total. Sample #1 to sample #10 are tested to determine the original fiber weight fraction of the whole specimen, while sample #11 to sample #20 are used to provide the fiber weight fraction of the specimens with one skin layer ground. As shown in Table 3.2, for the specimen with the same fiber weight fraction, the original thickness does not have much difference. The fiber weight fraction of the removed skin layer could be determined from these two sets of results. Meanwhile, the fiber weight fraction for the core layer could also be determined accordingly.

Figure 3.7 Specimens with the mount.

Sample #		Original thickness(mm)	Sample #		Original thickness(mm)	Thickness after grinding (mm)
20% fiber weight fraction	1	2.94	20% fiber weight fraction	11	2.90	1.84
	2	2.93		12	2.98	1.83
	3	2.95		13	2.94	1.78
	4	2.98		14	2.95	1.81
	5	2.91		15	2.92	1.82
40% fiber weight fraction	6	3.08	40% fiber weight fraction	16	3.07	1.80
	7	3.07		17	3.05	1.84
	8	3.09		18	3.15	1.77
	9	3.17		19	3.21	1.76
	10	3.00		20	3.03	1.83

Table 3.2 Dimension of specimen for the burn-off experiment

The burn-off test is performed at the Fraunhofer Project Centre for Composites Research at Western. Figure 3.8 shows the specimens and the crucibles in the burn-off equipment with thermal gravimetric analysis (TGA) technique, which could measure mass changing during the burn-off procedure. The equipment is heated to reach the temperature of 500 ℃ in half hour and remaining this temperature for a few hours. Under this condition, the

matrix material for the composite should be vaporized and exhausted through the tube. At such a temperature level, the carbon fibers should remain stable in the crucibles.

Figure 3.8 Burn-off test equipment.

However, during the burning off process, the carbon fibers keep disappearing over the time, despite the fact that the crucibles are covered by lids. Figure 3.9 shows the variation of both the weight of sample #1 and the temperature. It is expected that the weight should reach a plateau after burning off the polymer matrix, which is 20%. However, the curve

shows that sample#1 keeps losing its weight even though it is already much lower than the fiber weight fraction. Similar trend for the other samples is also observed. Therefore, the burn-off test fails for determining the C/DFRC weight fraction.

The major reason for this failure is due to the short length and the light weight of carbon fibers, so the fibers are removed with the vaporized matrix material. It is also possible that the ventilation of the equipment is too strong. As shown in Figure 3.10, most remaining fibers after this experiment are in bundles. Since the single carbon fiber is too short and light, it is very easy to be blew off with the matrix material. Because the rest of fibers are bundled together, and the weight is higher than one single fiber, it is relatively hard to remove the bundles with the vaporized matrix.

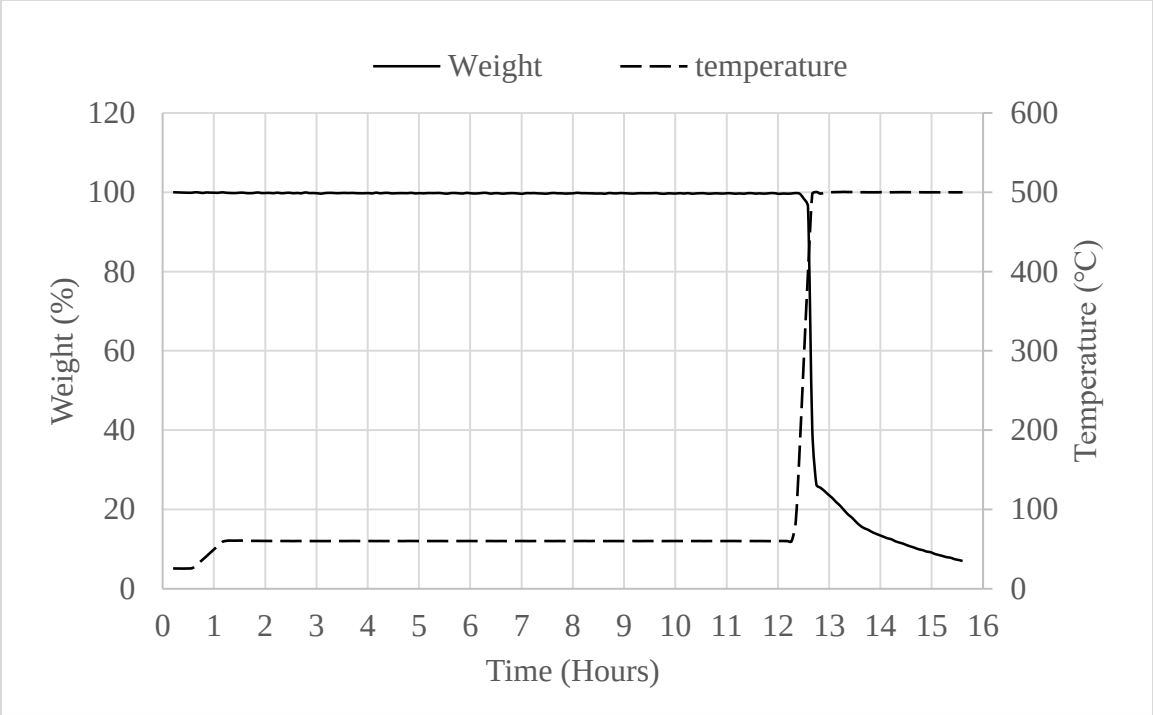

Figure 3.9 The TGA curve for specimen #1.

Figure 3.10 The remaining carbon fibers after burn-off test.

Further burn-off test is performed at Ford Research and Innovation Center. Similar results have obtained. It is thus concluded that more investigation is required to facilitate the burn-off test for C/DFRC. Here we attempt an alternative method to determine the fiber volume fraction distribution through the material thickness, which is based on the microscopy technique.

3.3 Microscopy-based method

Since the fiber distribution along the plaque thickness follows a skin-core structure and most fibers are oriented at in plane direction (Zeng et al., 2014, 2015), we can use microscope image of the plaque cross section to capture the fiber distribution features. After the cross section images are captured, the fiber volume fraction distribution could be determined by image analysis. It should be noted that the accuracy of this method highly depends on the qualities of both the surface and images. For finely polished cross section, the obtained images could capture more detailed features for the fiber layering (ASTM International, 2010b; Almeida et al., 2012; Mcdonough et al., 2004; Paciornik & Almeida, 2010).

3.3.1 Specimen preparation

Figure 3.11 shows the location, dimension, and grinding and polishing surface of the specimen. The specimen is located in the center of the C/DFRC plaque since the orientation tensor predicted by the Moldflow (Modex3D) is more reliable at this location. Similar to the burn-off experiment, two sets of specimens with different fiber weight fraction are prepared, i.e., sample A has 20% weight fraction, and sample B has 40% weight fraction.

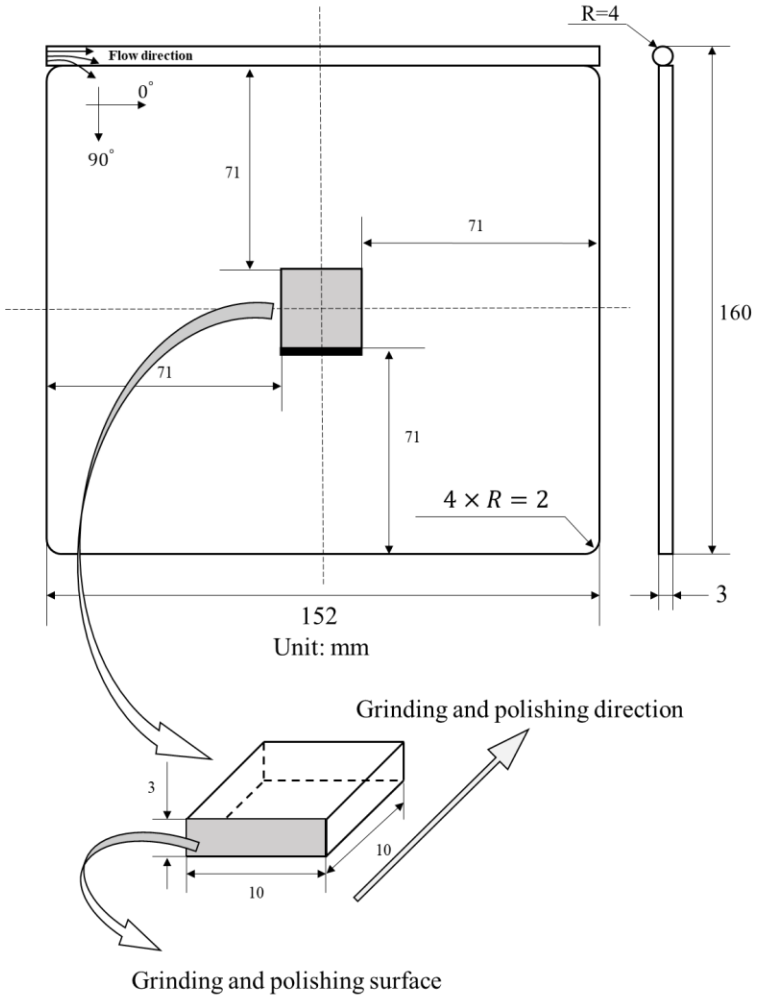

Figure 3.11 Illustration of the specimen grinding and polishing direction for the Microscopy-based method.

In order to support the specimen in a stable medium, the cold mounting method is applied. Before the cold mounting process, the specimens should be cleaned by acetone. Then the resin (epoxies) is mixed with a hardener to provide the mount for the specimen, the curing

time for the epoxy system is about 12 hours. Then the mounted specimens are knocked out, as shown in Figure 3.12, which are ready for surface grinding and polishing.

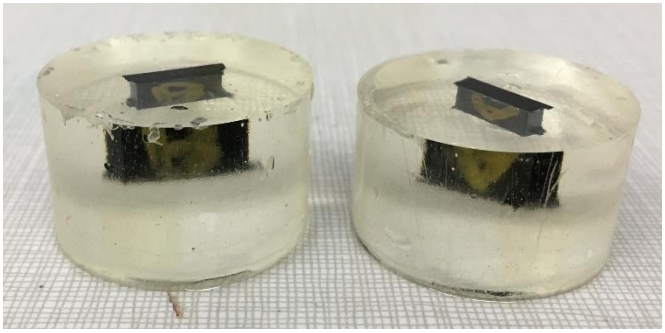

Figure 3.12 The specimens after cold mounting process.

Firstly, the mounted specimen is ground by coarse sandpaper. In this step, the damages from the specimen cutting could be mostly removed. Then the higher grit sandpaper is used to get a smoothing surface. Polishing process is very important for the microstructural analysis of the specimens, and all the damage from the cutting process should be completely removed (Ltd. R, 2002).

Figure 3.13 polishing machine and polishing powder for the C/DFRC specimen.

The polishing machine used in this process is shown in Figure 3.13. The abrasives are alumina (AL_2O_3) and monox (SiO_2), with grain sizes of 0.3μm and 0.25μm respectively. After the fusion of AL_2O_3 with water, the abrasives could be added to the interface between

the polishing surface of the specimen and the polishing disc. In addition, the lower force pushed on the specimen, the higher quality of the polished cross section could be obtained. A similar polishing procedure with SiO_2 is performed afterwards to get smoother surface of the specimen. Then the polished cross section of the specimen is ready for the next step imaging.

3.3.2 Microscopic image acquisition

To determine the fiber volume fraction gradient accurately, the images with the large magnification and high resolution are required. For image pixel analysis, higher magnification image could ensure more accurate results. However, limited by the resolution, a single image could not capture the information for the whole cross section of the specimen, i.e., a single clear image could only represent a portion of the whole cross section. Therefore, it is necessary to take several images with the same magnification, and join these images together to get a mosaic image for the pixel analysis (Paciornik & Almeida, 2010). Since the mount surface is not flat, the microscope would have some problems in focusing. Therefore, the specimens need to be compressed on the plasticine by the levelling press (Figure 3.14), and a piece of paper was covered on the polished surface to prevent scratching.

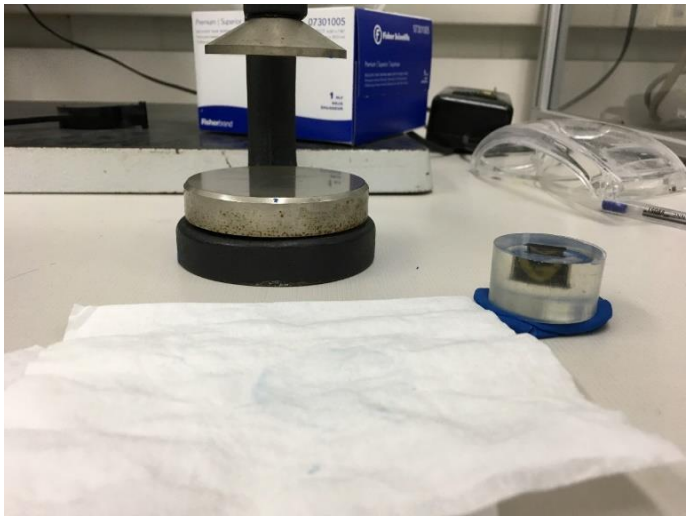

Figure 3.14 Specimen levelling press.

To determine the appropriate magnification of a single image, three sets of images are compared. The eyepiece lenses of the microscope is set as 10 times, and the magnification of objective lenses is set as 10, 20 and 50 times, respectively. The microscope provides a sample holder, which allows to control the displacement between each image accurately.

Figure 3.15 shows the image comparison for sample A and sample B. The fiber volume fraction gradient could be easily observed even in the low magnificent images, and these images could represent a larger area for the cross section. It is also found that the fiber volume fraction gradient is more obvious in the sample with the higher fiber weight fraction (or volume fraction). Therefore, sample B (WF=40 %) will be more focused on the images analysis in this experiment.

A series of images with the same magnification are consecutively taken along the thickness direction and are joined together. The joint images could reflect the information for the fiber distribution along the specimen thickness direction, which are divided into five layers in the current work to determine the fiber volume fraction gradient as shown in Figure 3.16. Moreover, Figure 3.16 only represent a portion of the whole cross section. In order to capture the complete information for the whole cross section of the specimen, similar images should be joined in parallel, so that image for the whole cross section of the specimen can be obtained.

A Matlab code is developed for the image pixel analysis, and is tested by analyzing the fiber volume fraction distribution through the five layers. The details of the analysis process and the theory of the image pixel analysis will be introduced in the next section. After testing the images by pixel analysis, the fiber volume fraction in these five layers is determined. Under the same conditions (the pixel of the images, the grey level) of pixel analysis, it is found that the trend lines for each layer volume fraction with the magnification of 200 times and 500 times are similar. However, the predicted results from 500 times magnification is closer to the fiber VF provided. Therefore, the microscope magnification (500 times) is selected. Meanwhile, the Matlab code for the image pixel analysis is approved to be valid.

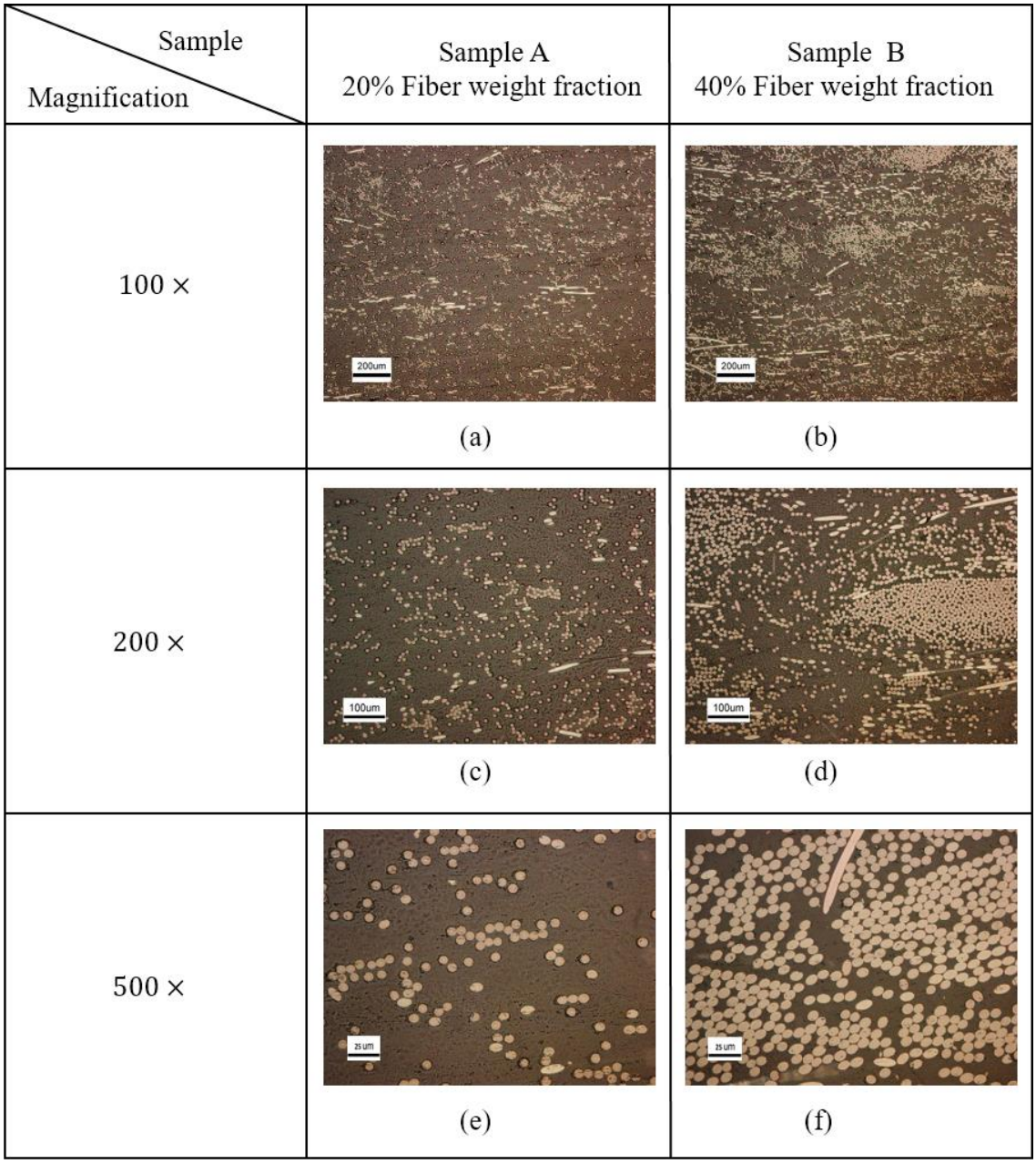

Figure 3.15 Comparing different magnification for sample A and B.

The specimens are sent to Ford Research and Innovation Center for batch imaging following the standards we set. After the images for the entire cross section are obtained, grinding and polishing processes are repeated on the specimen in order to get the images of the cross section at different depth. Totally, we get three sets of whole cross-section images at different location along the grinding direction for sample B for averaging purpose.

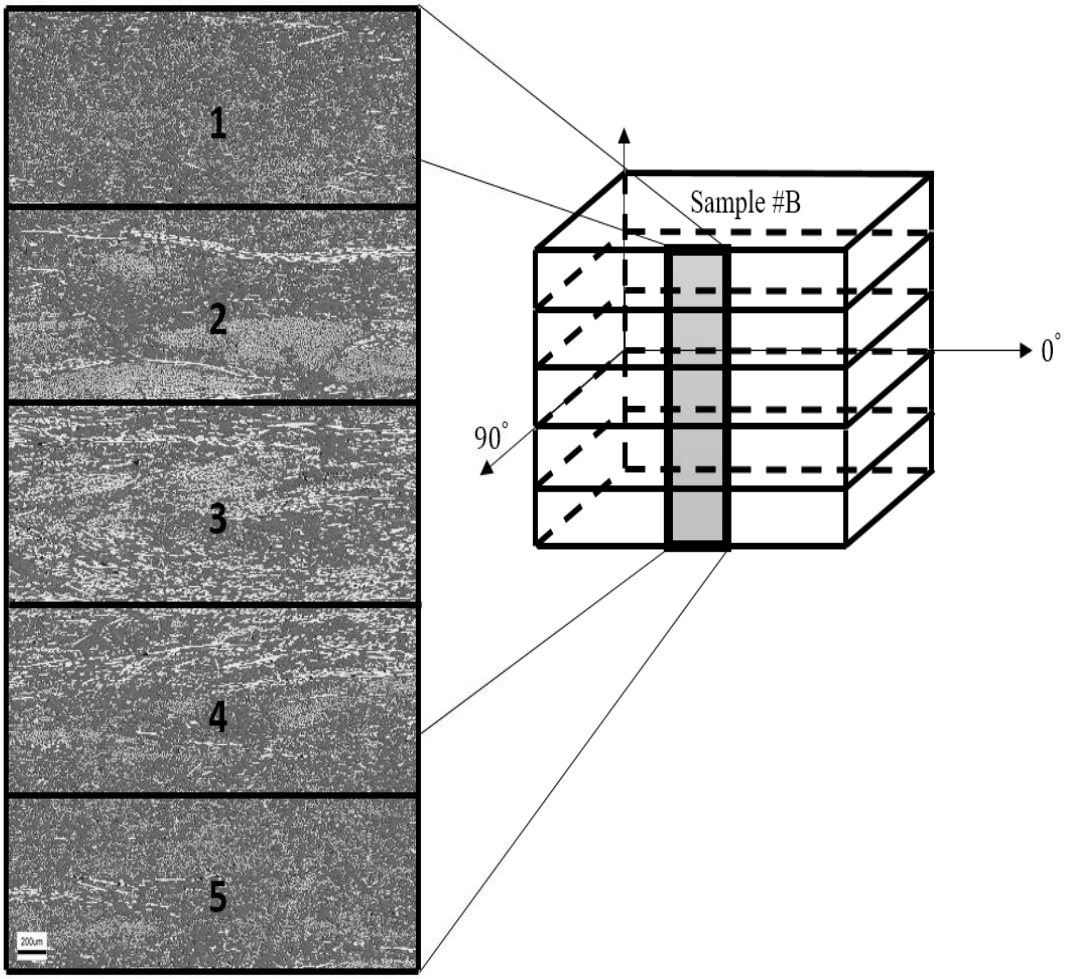

Figure 3.16 Example image for the specimen with WF=40%, the magnificent for the objective lens and the eyes lens are 50 and 10 respectively.

3.3.3 Image pixel analysis

Generally, there are two methods in the literature for the image pixel analysis, i.e., areal method and fiber counting method, respectively (Guild & Summerscales, 1993). The areal method is more commonly used, while the fiber counting method requires a very accurate measurement of the fiber cross section area. When the high quality and magnification images obtained, the areal method could provide an accurate fiber VF gradient through the thickness direction (Cann et al., 2008). Because the shooting angle of the microscopy camera is not perfectly consistent with the C/DFRC specimen, the area close to the edges

could affect the accuracy of the pixel analysis. Before performing the pixel analysis, the coarse edges of the images are cut off as shown by the perfect rectangular shape in Figure 3.17. Only the area inside of the black rectangle line is remained for further analysis. The high resolution microscope at Ford Research Innovation Center provides a series of images along the width of the cross section, which are taken separately and further joined together. There are several white vertical lines in this example image, which are formed in the process of image joining.

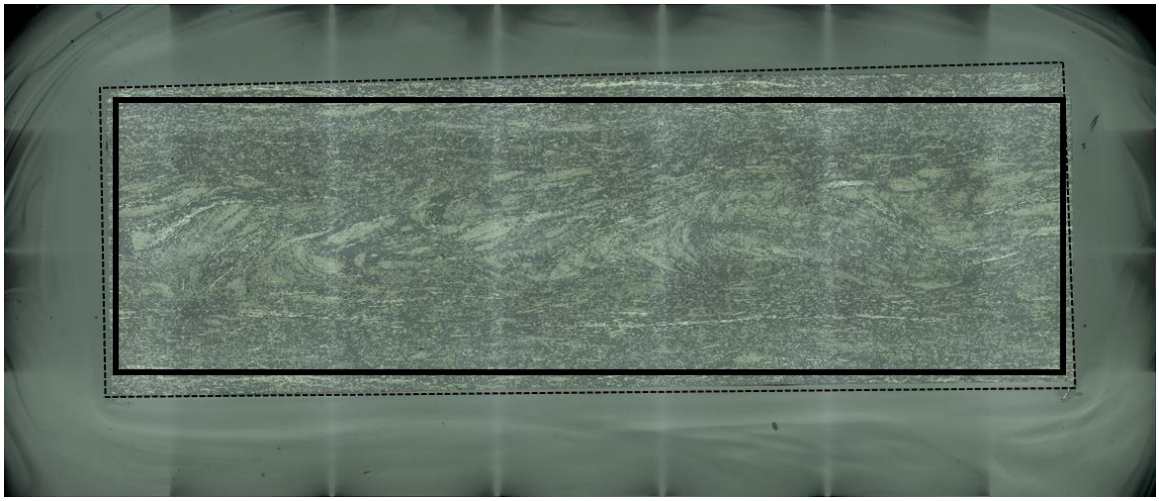

Figure 3.17 Image chopping for pixel analysis, Image #1 for Sample B.

Then the chopped images within the rectangle are transferred to black-and-white or binary images. To obtain the binary images, there is a grey level in the Matlab program code needs to be set appropriately. If the grey level of a pixel is greater than the chosen threshold value, this pixel will turn into white. Otherwise, it will turn into black. The purpose of creating the black and white pixels is to segment fibers and matrix, i.e., the white pixels represent the fibers, while the black pixels represent the matrix. For the areal method, the computational algorithm is to count the number of the black and white pixels in the area of the image of interest. Then, the area fraction of fibers (white pixels), i.e., the corresponding fiber VF, is calculated as the number of the white pixels divided by all the pixels in the image. In the areal method, the grey level is the key factor to affect the accuracy.

For the tested C/DFRC, the fiber VF for sample A and sample B are converted from the WF as 16% and 30%, respectively. First, we need to determine the grey level of the images,

which is realized by running a looped Matlab code for testing on the binary images of the specimen with 30% volume fraction until the calculated fiber VF agrees well with this prescribed value. For each individual test for determining the grey level, the binary images are different. Figure 3.18 shows the binary images with different grey level for the analyzed area in Figure 3.17. For example, in Figure 3.18 (a) and (c), the grey level are 0.53 and 0.42, respectively. The calculated fiber VF are 18% and 46%, respectively, which are far away from the target value (30%). The results are expected since as the grey level decreases, the images will become brighter, and the program will recognize more pixels as the fibers. Therefore, the calculated result of the fiber VF will be higher for the binary images with lower grey level. When the grey level reaches 0.475 as shown in Figure 3.18(b), the fiber VF is calculated as 30.05 %, which is very close to the target value. Therefore, the value of 0.475 is selected as the grey level for the next step image pixel analysis.

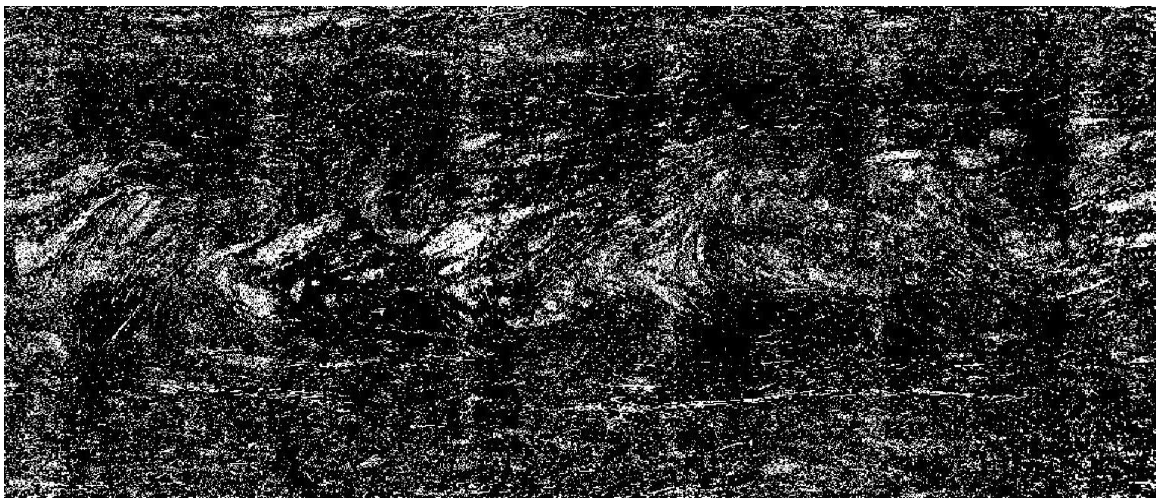

(a)

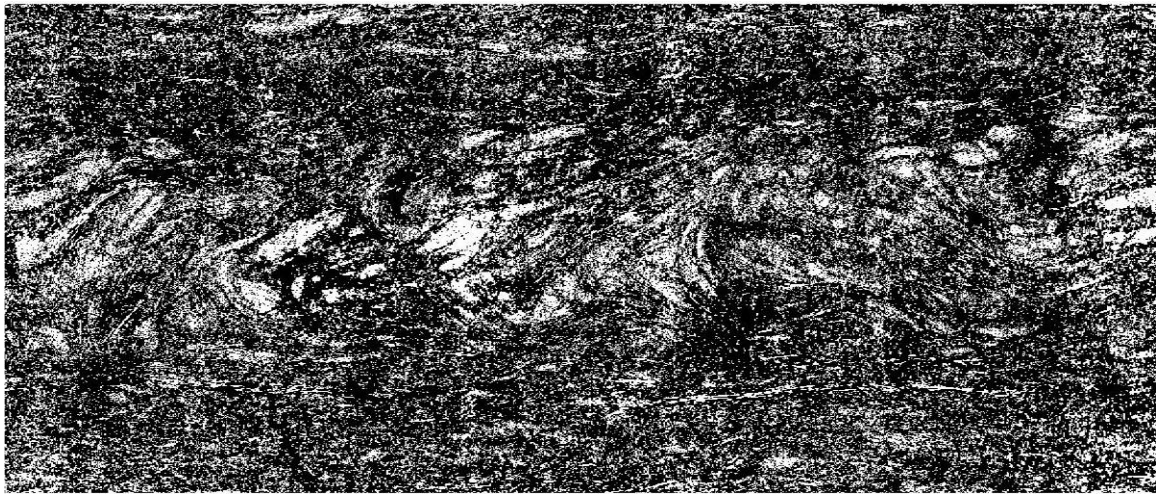

(b)

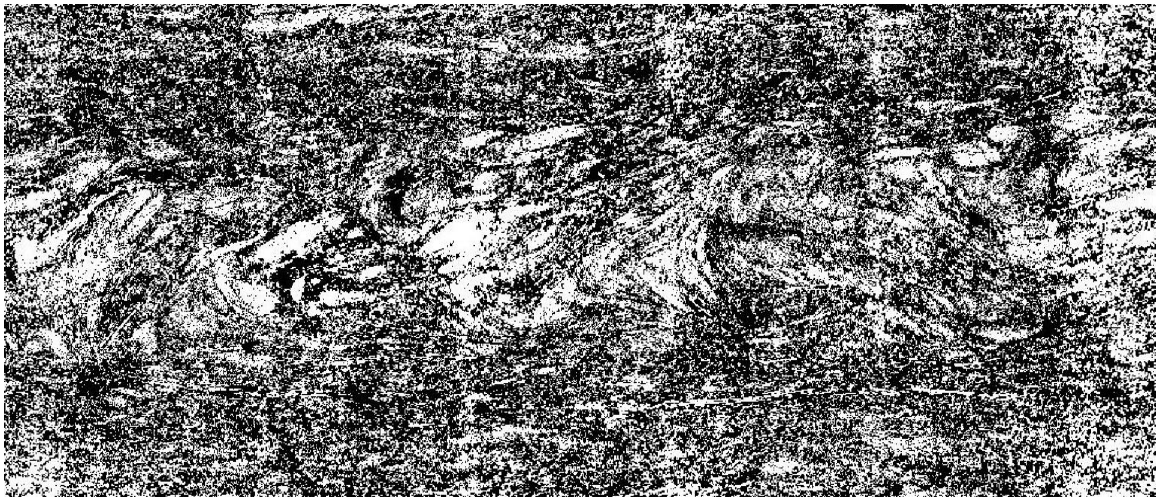

(c)

Figure 3.18 Binary images with different grey level for Image #1 of sample B.

In order to determine the fiber volume fraction gradient along the sample thickness direction, the image of the whole cross section is divided into 25 segments with five rows and five columns. Figure 3.19 shows an example for the divided segments of the original images in Figure 3.17. There are three original images for sample B (VF=30 %), and one original image for sample A (VF=16 %). These images are treated in the same way and the image pixel analysis is performed on the segmented images with the selected grey level

value of 0.475. Table 3.3 and 3.4 summarized the calculated fiber VF for each segment in the images, with the row and column numbers defined in Figure 3.19.

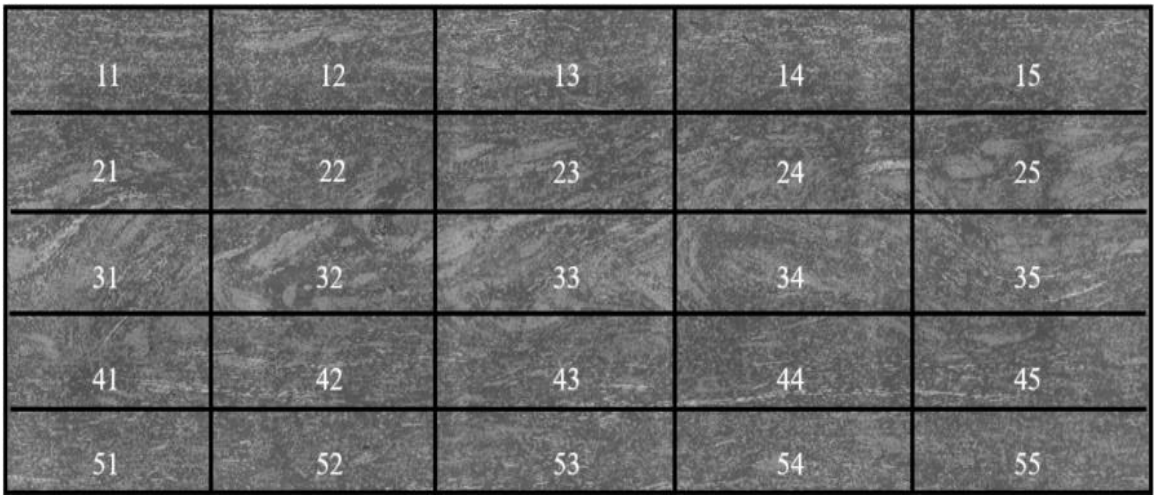

Figure 3.19 Illustration of the image segments of Image #1 of sample B.

Image #1, Sample B, Fiber VF=30 %						
Column# / Row#	1	2	3	4	5	Averaged Result
1	27.50%	26.70%	29.20%	27.40%	29.30%	28.00%
2	29.80%	27.40%	30.60%	31.30%	32.40%	30.30%
3	37.50%	36.70%	37.30%	33.10%	36.40%	36.20%
4	33.00%	31.70%	32.10%	31.50%	34.00%	32.50%
5	31.50%	27.00%	27.10%	24.70%	26.80%	27.40%
Image #2, Sample B, Fiber VF=30%						
Column# / Row#	1	2	3	4	5	Averaged Result
1	29.00%	29.20%	30.70%	28.90%	28.70%	29.30%
2	30.50%	32.20%	32.30%	31.00%	31.10%	31.40%
3	35.00%	35.80%	36.20%	35.40%	33.90%	35.30%
4	32.00%	34.20%	31.90%	30.60%	28.80%	31.50%
5	26.60%	26.90%	26.80%	24.90%	23.30%	25.70%

Image #3, Sample B, Fiber VF=30%						
Column# / Row#	1	2	3	4	5	Averaged Result
1	28.80%	31.40%	29.30%	28.10%	27.50%	29.00%
2	24.30%	24.40%	27.00%	28.60%	32.80%	27.40%
3	45.10%	38.20%	43.70%	37.40%	38.40%	40.60%
4	32.30%	28.70%	29.80%	21.10%	27.00%	27.80%
5	30.40%	25.60%	28.30%	31.40%	28.90%	28.90%

Table 3.3 Fiber volume fraction calculated for each segment, Image #1, #2, #3, sample B.

Image #4, Sample A, Fiber VF=16%						
Column# / Row#	1	2	3	4	5	Averaged Result
1	16.00%	15.50%	14.60%	14.50%	14.60%	15.04%
2	16.60%	16.40%	14.30%	16.20%	17.20%	16.14%
3	18.30%	17.30%	16.50%	18.80%	18.40%	17.86%
4	18.60%	15.40%	16.70%	18.90%	17.90%	17.50%
5	14.70%	14.30%	13.60%	14.60%	15.00%	14.44%

Table 3.4 Fiber volume fraction calculated for each segment, Image # 4, sample A.

As observed from Tables 3.3 and 3.4, the fiber volume fraction gradient is clearly presented, particularly for the specimen with higher volume fraction, i.e., sample B. From the averaged fiber VF of different layers of sample B, it is found that core section of the sample has a higher volume fraction, approximately 29% than the skin parts. For the C/DFRC sample with relatively lower volume fraction (16%), the fiber volume fraction gradient is not that significant, which is about 3 % difference between the core and skin parts.

It is concluded from the image pixel analysis that for injection molding process, the fiber volume fraction through the plaque thickness is not homogeneous. In order to increase the accuracy of the prediction on the elastic constants for the C/DFRC, it is necessary to consider the effect of the fiber volume fraction gradient. The averaged fiber VF gradient

through the specimen thickness will be imported into the integrated software package to predict the elastic constants of C/DFRC.

3.4 Results and discussion

The tensile tests are performed at the Ford Research and Innovation Center with Digital Image Correlation (DIC) to make the measurements. Specimens from both the G/DFRC and the C/DFRC plaques are tested. Figure 3.20 shows three typical stress-strain curves for the C/DFRC specimen A-1 as shown in Figure 3.3 of Chapter 3.1. The fiber weight fraction of the tested C/DFRC plaque is 40 % (30 % fiber VF).

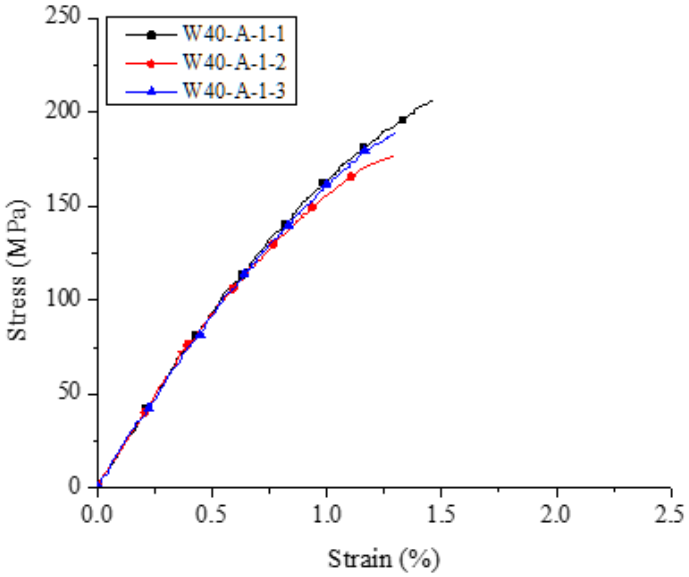

Figure 3.20 typical stress-strain curve for the tensile test with tested specimens.

The gripping position on the specimen during the tensile test may cause the error of the tensile strength. As shown in Figure 3.20, the tensile strength for three specimens at the same position of the plaque is different, but the linear sections for three curves are quite close to each other. The linear section on the curve is chopped and used to calculate the Young's modulus in the loading direction, which is averaged by these three sets of data. The tensile modulus in the loading direction from the experiments will be compared with the integrated software package simulation results in the following sections.

3.4.1 Test and prediction results for G/DFRC

The integrated software package is run to predict the elastic constants for the G/DFRC with two sets of fiber VF, and the fiber AR is 20 for both sets of fiber VF. The comparison is shown in Figure 3.21 and Figure 3.22 for the composites with the volume fraction of 15 % and 10 % respectively. It is obvious that the results demonstrate the material heterogeneity from both experimental measurements and numerical simulations, i.e., the longitudinal modulus is direction dependent. In general, the longitudinal modulus of the specimens in 45º direction is less than that along 0º and 90º directions. Meanwhile, the higher fiber volume fraction results in the higher reinforcement effect.

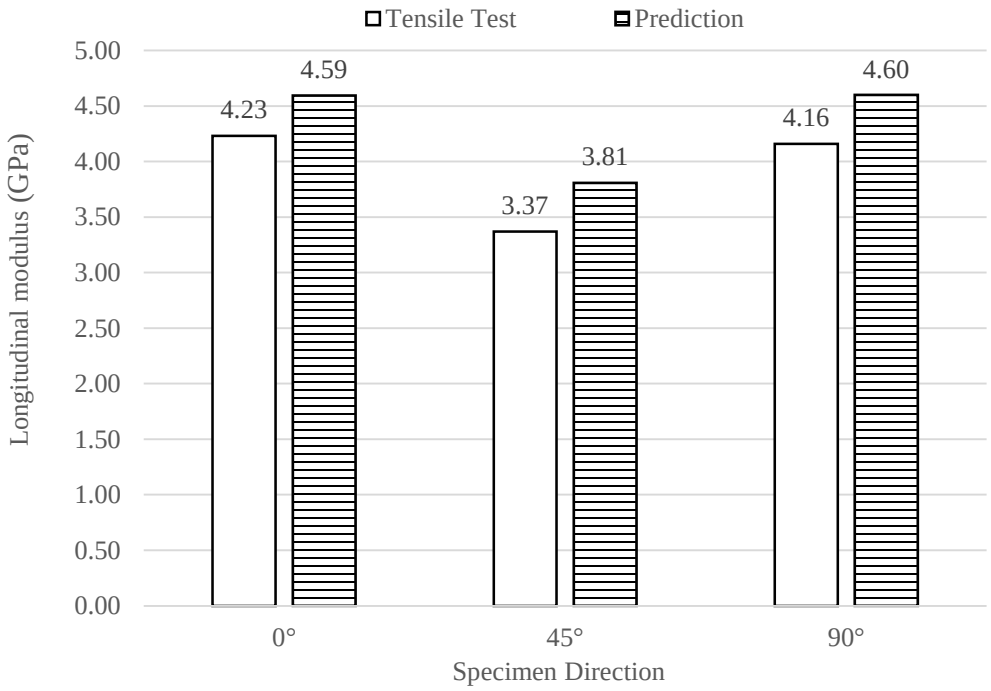

Figure 3.21 Result comparing for GFRC plaque with 15 % fiber volume fraction.

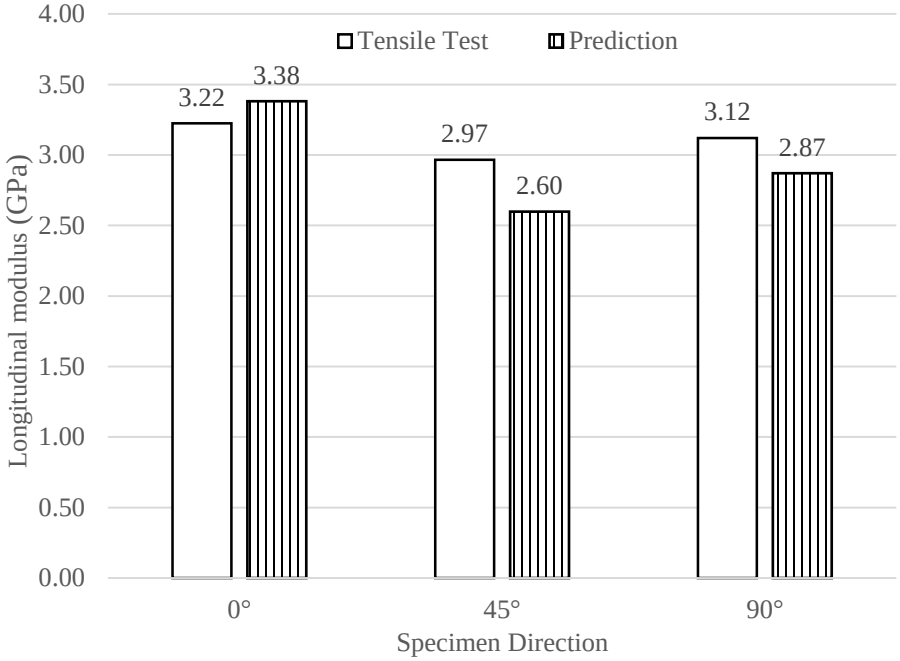

Figure 3.22 Result comparing for GFRC plaque with 10% fiber volume fraction.

Specimen direction on the tested plaque	The error of predicted longitudinal modulus	
	VF=10%	VF=15%
0° direction	4.83%	8.63%
45° direction	12.36%	12.99%
90° direction	8.02%	10.54%

Table 3.5 The error of the prediction for each case of the G/DFRC plaque.

For both cases, the numerically predicted results agree well with the tested data. As shown in Table 3.5, the error is below 10 % for most specimens. It can be found the error for the specimens with 15 % fibers is higher than that for the 10 % fiber volume fraction. The simulation results for the composites with 15 % fiber volume fraction are higher than the measured data, which may attribute to the fiber bundle effect. During the injection molding process, it is more likely for the fibers to form bundles in the composites with higher fiber volume fraction, and some fibers may also be curved. However, in the FE simulation, we only consider the ideal case that the fibers are all straight and not in physical contact.

Overall, the integrated software package is found to provide reliable predictions on the elastic constants of the G/DFRC samples.

3.4.2 Test and prediction results for C/DFRC

For the C/DFRC specimens, the integrated software package is run to predict the Young's modulus of two sets of samples, which have different volume fraction, i.e., 16% and 30%, respectively. There are four main input values in the integrated software package, the properties of the fiber and the matrix, the fiber aspect ratio, the fiber orientation tensor, and the fiber VF. The fiber aspect ratio is taken as 80, and the fiber and matrix material properties are listed in Table 2.1.

For these two sets of samples, the fiber VF gradient is calculated by the image pixel analysis in the previous section. However, since the fiber VF gradient for the samples with the volume fraction of 16% is not significant. It is, therefore, assumed as a constant to input into the integrated software package.

Layer #	Fiber VF (Averaged in columns)	Specimen Position on C/DFRC Plaque	The Analyzed Image	Calculated E_L (GPa)
1	28.00%	A-1	Image #1 Sample #B	20.24
2	30.30%			
3	36.20%			
4	32.50%			
5	27.40%			

Table 3.6 An example of calculating E_L, fiber volume fraction 30%

We choose six different locations of the plaque following different cutting strategies as shown in Figure 3.3 to prepare specimens in the tensile test. For each location, we prepare 3 specimens for repeating the testing. Therefore, for the C/DFRC with each individual volume fraction, there are total 18 specimens prepared. For the C/DFRC with volume fraction of 16 %, the Young's modulus along the loading direction is calculated through the integrated software package by using a constant volume fraction. However, for the C/DFRC with volume fraction of 30 %, the fiber volume fraction gradient effect is

considered and the calculation procedure is complex. Take the specimen A-1 as an example, the specimen is divided into five layers through the thickness direction. The input volume fraction value of each layer for the integrated software package is listed in Table 3.6, which are determined from the pixel image analysis in the previous section. Then the Young's modulus along the loading direction for each individual layer is calculated and output from the integrated software package. The Young's modulus for all the layers are then averaged to get the effective Young's modulus for the whole specimen. Similar procedure is performed to calculate the Young's modulus along the loading direction and the results are used to compare with the experimental results.

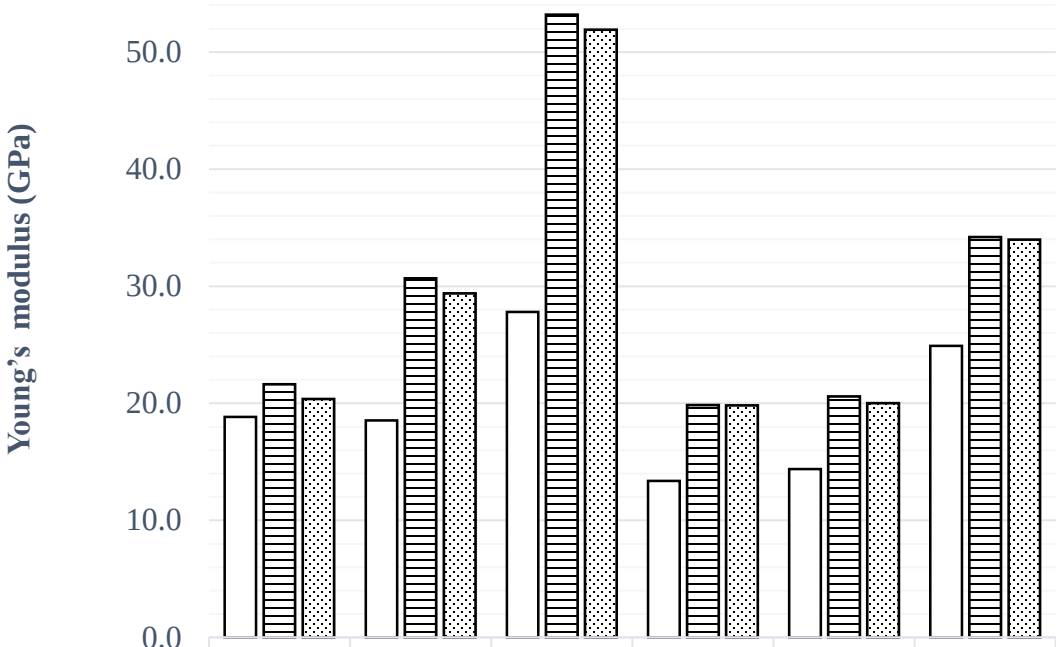

	A-1	A-2	A-3	B-1	B-2	B-3
Tensile Test (GPa)	18.8	18.5	27.8	13.4	14.4	24.9
Prediction #1 (GPa)	21.6	30.7	53.2	19.9	20.6	34.2
Prediction #2 (GPa)	20.4	29.4	51.9	19.8	20.0	34.0

Figure 3.23 Comparison of the Young's modulus between test and predictions at different locations of the C/DFRC plaque with 30% fiber volume fraction.

Figure 3.23 shows the comparision for the Young's modulus of the C/DFRC with 30% fiber volume fraction between the tensile test and the numerical simulation for all the specimens (from A-1 to B-3). The constant fiber volume fraction is used in the prediction #1, while the fiber volume fraction gradient is used in the prediction #2. In the numerical

calculation package, the fiber orientation tensor is a input determined from the Moldflow simulation. Since the volume fraction is the same for all these specimens, the fiber orientation is the major factor causing the variation of the Young's modulus at different locations of the plaque. In general, it is observed in this figure that if the fiber volume fraction gradient is considered, the numerical simulation results are closer to the experimental prediction. The numerical simulation results also overpredict the Young's modulus. It should also be mentioned that the numerical simulation results highly depend on the accurary of the Moldflow simulation for the orientation tensor. For example, for A-3 location, the Moldflow simulation result is not that reliable since this location is closed to the edge of the plaque.

Specimen	Error of Young's modulus E_L		
	Uniform VF	Graded VF	Improvements
A-1	14.76%	8.18%	6.58%
A-2	65.34%	58.41%	6.93%
A-3	91.37%	86.75%	4.62%
B-1	48.43%	48.17%	0.26%
B-2	43.05%	39.09%	3.95%
B-3	37.40%	36.51%	0.89%

Table 3.7 The error percentage of the Young's modulus of the C/DFRC plaque with 30% fiber volume fraction.

The error between the testing and numerical results is summarized in Table 3.7, from which considerable discrepancy is observed by the comparison. When considering the fiber volume fraction gradient, the relative error could be reduced over 6.5% at locations A-1 and A-2, but no significant change for the other locations. Especially for locations B-1 and B-3, the error reduction could be neglected. It is thus concluded that the effect of fiber volume fraction gradient could be compensated by the fiber orientation tensor in the numerical simulations. Another possible reason for the low error reduction may attribute to the lack of image pixel analysis. There is only one specimen location prepared for the image pixel, which is located at the center of the plaque. According to the cutting strategies in Figure 3.3, this image specimen is cut exactly from the same location as specimen A-2 and B-2. It is the reason that the consideration of the VF gradient can make more accurate

prediction on the Young's modulus. Since we use the same VF gradient for the other samples, the improvement for the Young's modulus prediction is slight.

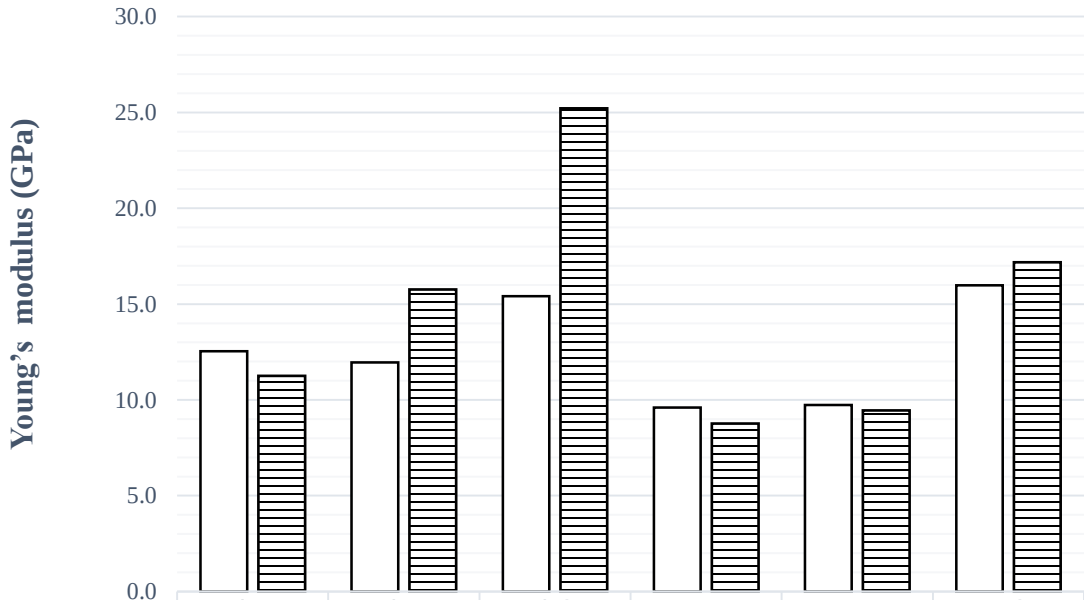

	A-1	A-2	A-3	B-1	B-2	B-3
Tensile Test (GPa)	12.5	12.0	15.4	9.6	9.7	16.0
Prediction (GPa)	11.3	15.8	25.2	8.8	9.4	17.2
Error%	10.25%	31.81%	63.51%	8.76%	2.92%	7.50%

Figure 3.24 Comparison of the Young's modulus between test and predictions at different locations of the C/DFRC plaque with 16% fiber volume fraction.

As shown in Table 3.4, for the C/DFRC plaques with 16 % fiber VF, the fiber volume fraction gradient is not significant. Therefore, we input a constant volume fraction into the integrated software package to determine the Young's modulus for the specimen along the loading direction. Figure 3.24 shows the comparison of the Young's modulus between the tensile test and the numerical simulation results from the integrated software package. The numerical prediction agrees quite well with the tensile test results, except for specimen A-3. Again, this significant discrepany is believed to be caused by the inaccurate prediction on the orientation tensor from the Moldflow simulation since this location is close to the edge of the plaque.

Comparing the prediction errors between the C/DFRC specimens with different fiber VF, it is found that numerical prediction on the Young's modulus of the C/DFRC with less volume fraction is more accurate. The reason lies in the fact that for the composites with

higher volume fraction, the fibers have more chance to agglomerate as bundles and get curvature. Therefore, it is also necessary to consider the curvature effects of the fibers for predicting the elastic constants of the DFRC.

Chapter 4

4 Fiber curvature effects

The objective of this chapter is to study the effects of fiber curvature on the elastic properties of the DFRC. From the microscopic images available in the previous chapter, it is clearly demonstrated that there are some curved fibers distributed in the composites. Both numerical simulation and analytical method (Bapanapalli & Nguyen, 2008) have shown that the curved fibers affect the mechanical properties of the composite materials significantly, particularly along the longitudinal direction, i.e., a remarkable stiffness reduction. However, there is relative small change for the material constants in the transverse direction. In the integrated software package we developed, the fibers are assumed as perfectly straight without considering the fiber curvature effects. As expected, the numerical simulations provide over-predicted results. Therefore, it is necessary to incorporate the curvature effects for calibrating the numerical results from the integrated software package.

There are several reasons that the fiber curvature is not included in the integrated software package directly. In the 1st module of the integrated software package, every fiber is randomly inserted into the RVE. When inserting the curved fibers into the RVE model, the new generated fiber has more chance to overlap with the pre-existing fibers due to the geometry of the curved fibers. In addition, due to the overlapping problem when inserting the curved fibers, it is more difficult for the RVE model to reach the target fiber volume fraction. Therefore, it is necessary to find an alternative method to represent the fiber curvature effects on the mechanical properties of the DFRC materials, which will be combined with the simulation results from the integrated software package to ensure both the accuracy and the efficiency of the computational modeling.

As well known, both analytical and numerical models have shown that the longitudinal modulus of the DFRC decreases with the decreasing of the fiber aspect ratio (AR) (Halpin Affdl & Kardos, 1976; Hine et al., 2002). Since the fiber curvature also tends to decrease the longitudinal modulus of the composites (Bapanapalli & Nguyen, 2008), we attempt to

correlate the curvature effects to the fiber effective AR by numerical calibration. This is realized through the following steps:

1) Predict the elastic properties of the RVE model with curved fibers. For each set of DFRC with fixed fiber volume fraction and true fiber AR, the RVE models with different fiber curvature angles are created in Abaque/CAE to output the longitudinal modulus;

2) Determine the effective fiber AR. With the same fiber volume fraction, the calculated modulus of the DFRC with curved fibers along the longitudinal direction will be used to fit the results output from the 1st module in the integrated software package for calibration purpose. This will determine the effective fiber AR according to the curvature.

When the image information of the distribution of fibers in the composites with the known fiber volume fraction and true fiber AR is given, we can determine the fiber curvature, which will be further transferred to the effective AR. This effective AR will be further input back to the integrated software package to predict the elastic constants of the DFRC.

4.1 Finite element (FE) analysis on RVE with curved fibers

In the FE analysis, a RVE model with solid embedded element is developed to predict the longitudinal modulus E_L for the DFRC with curved fibers. The fiber curvature is described by angle θ as shown in Figure 4.1, in which the fiber true length is defined as the arc length. Particularly for the straight fiber, the fiber curvature is 0^o. The fiber true aspect ratio (AR) is defined as the ratio of the true length to the diameter. The projected fiber length direction is defined as the longitudinal direction. In order to capture the fiber curvature effects, the fiber true length is remained the same in the modeling, while the curvature angle keeps changing.

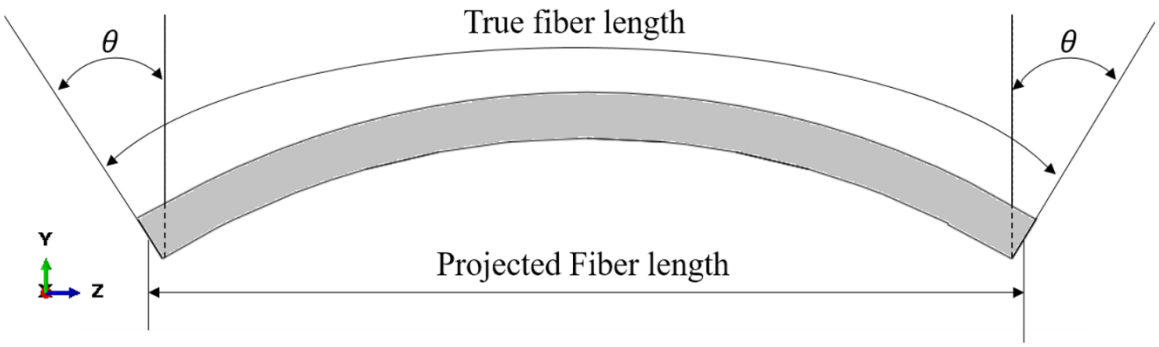

Figure 4.1 Illustration of the single curved fiber.

For each numerical testing model with fixed fiber volume fraction and AR, we select eight sets of fiber curvatures ranging from 20º to 60º. According to the previous studies (Bapanapalli & Nguyen, 2008; Velmurugan et al., 2014), the fiber curvature only has a minor effect on the elastic constants of the composites if the curvature angle is less than 20º. Therefore, we start the curvature angle from 20º and set the elastic constants the same as the DFRC with straight fibers for all the cases with the fiber curvature angle less than 20º. Since it is getting more difficult to create the RVE model for the fiber curvature angle over 60º due to the fiber overlapping, the highest fiber curvature angle considered in the numerical modeling is 60º.

For case study, we select the material as the G/DFRC with two sets of volume fractions, i.e., 10% and 15%, in order to make comparison with the experimental data. For each volume fraction, the AR is set as 20, 50, 60 and 100, respectively.

4.1.1 RVE generation

The generation of RVE with straight fibers is usually realized through the random sequential adsorption (RSA) algorithm (Harper et al., 2012), i.e., with the determined RVE size, the fibers are randomly inserted in the RVE. By using this methodology, it is very hard to reach a high fiber volume fraction for the composites with oriented fibers due to the overlapping of the fibers (El-rahman & Tucker III, 2013). In the literature, researchers have attempted to develop efficient approaches to avoid fiber overlapping (Drugan & Willis, 1996). Unfortunately, it is even more challenging for the RVE generation with curved fibers since these curved fibers have more chance to overlap. Moreover, FE direct

meshing on the RVE is also a hard task to satisfy the mesh conformity at the interfaces between the curved fibers and matrix. In order to overcome these issues, the embedded element technique ("Abaqus/CAE User's Manual", 2011), referring to a meshing algorithm that specified elements are embedded in the host elements, will be employed in the current work. The merit of this technique lies on the fact that the matrix and fibers in the RVE could be meshed separately and independently, which can be automatically realized by using the Python script in the Abaqus/CAE. Therefore, in order to avoid the curved fiber overlapping, we generate the non-overlapping fibers first. With the given fiber volume fraction, the RVE dimensions are determined accordingly.

When generating the fibers, the space between the neighboring fibers should be sufficient to get enough elements to fill in. Otherwise, there will be convergent issue for the FE calculation. Since the matrix element size is proportional to the distance between the neighboring fibers, shorter distance means smaller elements size and more computation cost. Also, the shorter distance between the fibers induces more chance for the fiber overlapping.

Figure 4.2 shows an example for fiber overlapping when the distance (D_Y) is not selected appropriately. There is no overlapping for the model with aligned fibers in this case, but the overlapping problem occurs after the fiber curvature angle is increased. The overlapping shown by the black area in this figure will cause meshing problem even though the embedded element technique is applied.

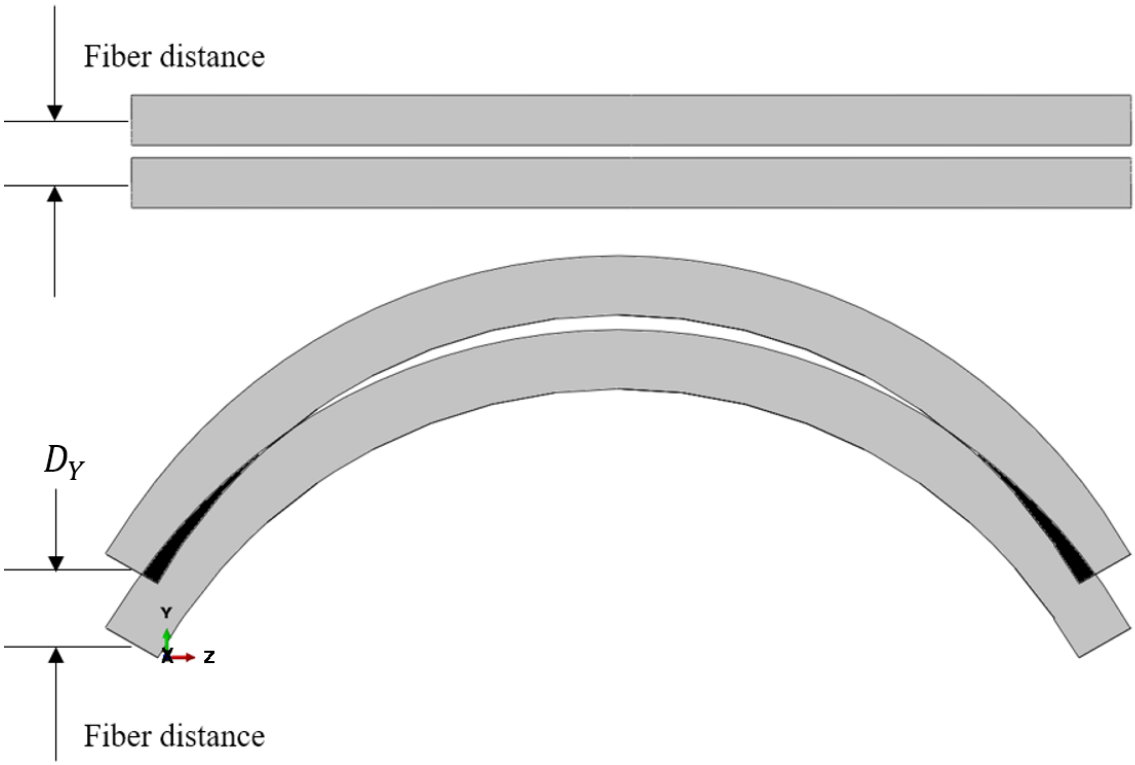

Figure 4.2 The example of overlapping fiber in the RVE model with curved fibers.

In addition, for the RVE model with the same fiber volume fraction and AR, the distance between the neighboring fibers should be fixed. The RVE model with higher fiber curvature angle is more likely to have the fiber overlapping, so it is better to start creating the RVE model from the case with the highest fiber curvature angle. Meanwhile, the fiber distance (D_Y) should not be too large. Otherwise, it is difficult for the fiber volume fraction to reach the target. After the generation of the fibers, the dimensions of the RVE model in Figure 4.3 are determined, with detailed information provided in Table 4.1. It should be mentioned that all the aligned fibers are curved in the transverse Y direction in Figure 4.3. However, the curved fibers can rotate randomly along the longitudinal direction, which means that the fibers could be curved in any direction within the X-Y plane. Since we only concern the longitudinal Young's modulus for calibration purpose, the well-arranged fibers in the RVE model are convenient for generating fibers. Otherwise, it is challenging to generate the non-overlapping fibers with curvature in random direction.

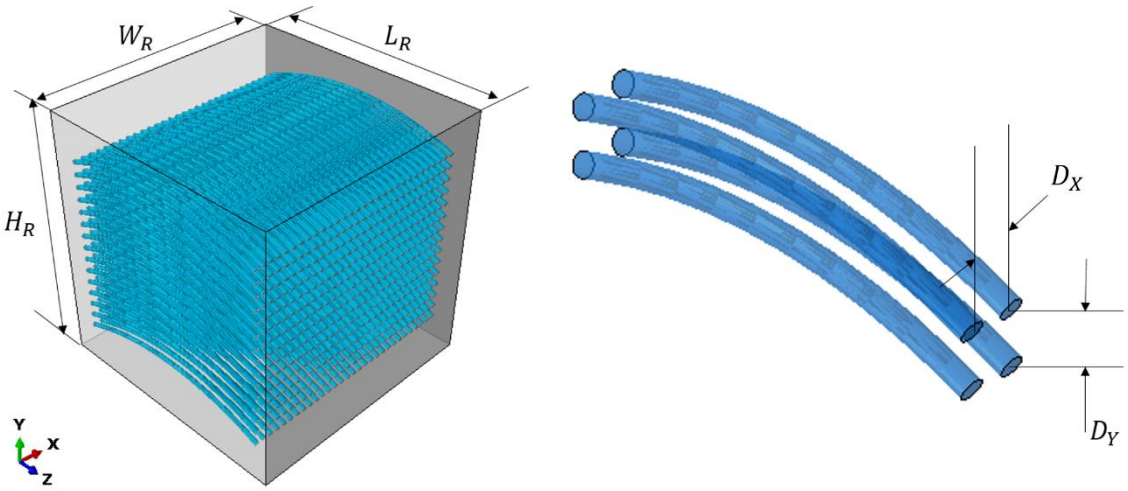

Figure 4.3 The fiber bundle and the Geometry of the RVE.

The detailed dimensions of the RVE model and the fiber distance are shown in Table 4.1, the parameters W_R and H_R are 9 for all the cases. The fiber distance and the RVE size should vary with the different fiber AR cases, so that the fiber volume fraction condition for all RVE models could be satisfied. Since the parameter unit option is not provided in Abaqus/CAE, users should define all the quantity units manually. The chosen length units for all procedures is millimeter, and the corresponding force and stress units are newton and mega pascal respectively.

VF=10%	D_X	D_Y	L_R
AR=20	0.30	0.70	9.3
AR=50	0.30	0.45	9.0
AR=60	0.24	0.42	8.5
AR=100	0.14	0.25	8.5
VF=15%	D_X	D_Y	L_R
AR=20	0.30	0.70	9.0
AR=50	0.26	0.42	8.8
AR=60	0.20	0.40	8.6
AR=100	0.10	0.25	8.4

Table 4.1 RVE dimensions and fiber distance.

4.1.2 RVE meshing

For meshing within the framework of the embedded element technique, the fibers are assigned with the embedded solid elements (ESE), while the matrix is assigned with the host solid elements. The Abaqus/CAE could identify the geometric relationship between the nodes of embedded elements (fibers) and the host elements (matrix). If the nodes of fibers elements lie within the matrix elements, then the translational degrees of freedom (DOF) of these nodes are constrained to the corresponding DOF of the matrix element through interpolation. However, the rotational DOF is allowed for the embedded elements without constrains by the host elements ("Abaqus/CAE User's Manual", 2011). Obviously, the CPU running time of the proposed RVE-ESE model is longer than the direct FE meshing approach since all of the additional constraints in the RVE-ESE model need to be dealt with before solving. However, the implementation of RVE-ESE model will significantly ease the meshing process since the matrix and fibers can be meshed independently. For the FE direct meshing, one must ensure the mesh conformity at the interfaces of the matrix and fibers, which must be done manually and is very time-consuming particularly for the curved fibers.

The next step is to select the element type. Due to the structure shape of the element, the tetrahedron (Tet) shape is more convenient to mesh the curved geometry in the matrix compared to the hexahedron (Hex) shape. However, with the same element size, the application of the Tet type element usually causes some element distortion and results in over-stiffness prediction as shown in Figure 4.4. Therefore, more Tet elements than Hex elements are required to get the same stiffness prediction of the RVE ("Abaqus/CAE User's Manual", 2011). In order to save computation time, both fibers and matrix are meshed by the structured Hex type element in the fiber curvature analysis, e.g., three-dimensional 8-node linear brick elements with reduced integration formulation (C3D8R) is selected.

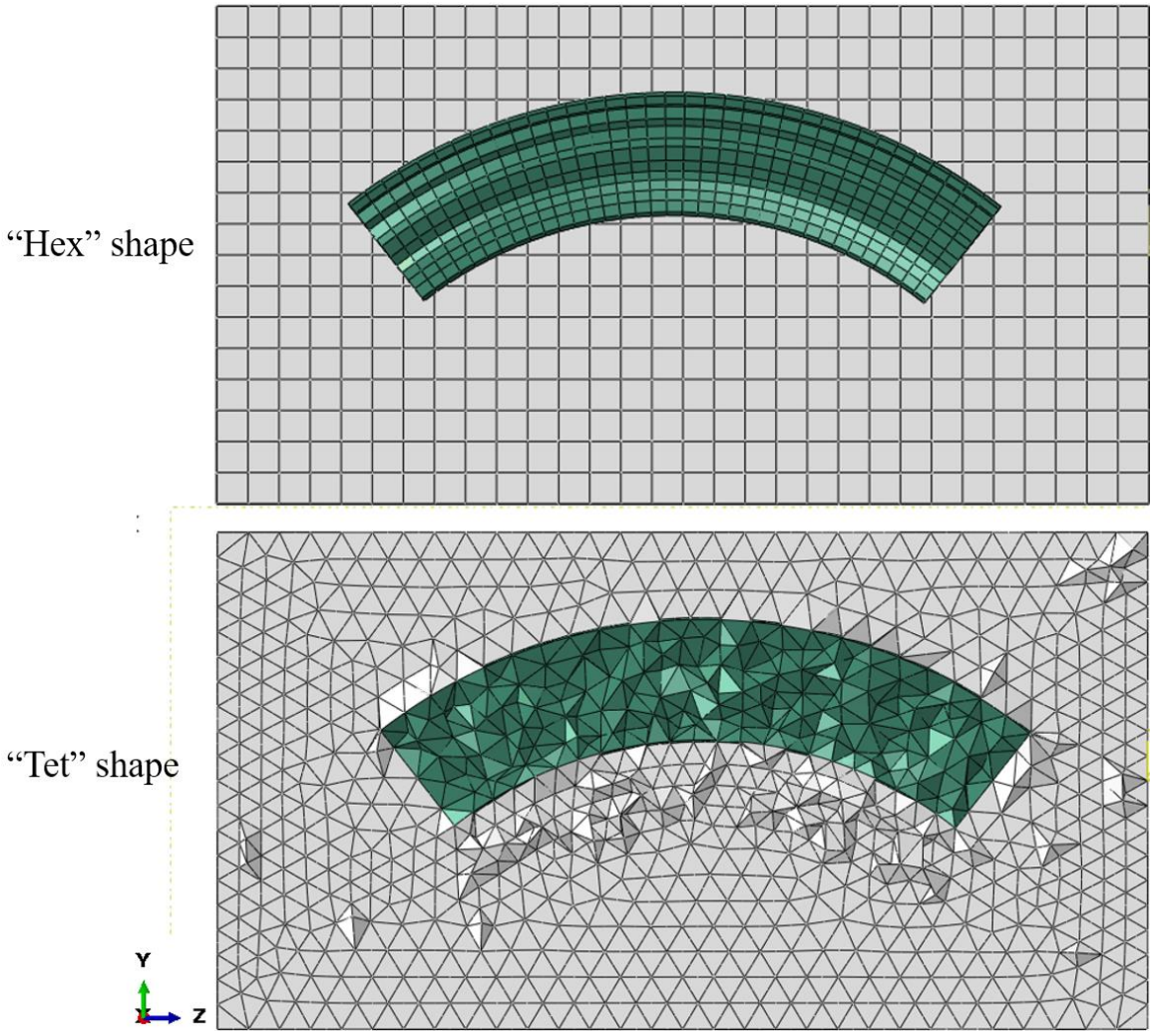

Figure 4.4 Cutting plane of the RVE model meshed by different type of elements.

The numerical prediction accuracy is affected by not only the element type, but also the element size. Usually, point load, sharp corner or point boundary condition may cause stress singularity, which can be attenuated by increasing the number of elements. Figure 4.5 shows the cross section of a meshed RVE model. To avoid the stress singularity, at least two matrix elements are guaranteed between every two fibers. Further testing on the convergence of the meshing will be performed later.

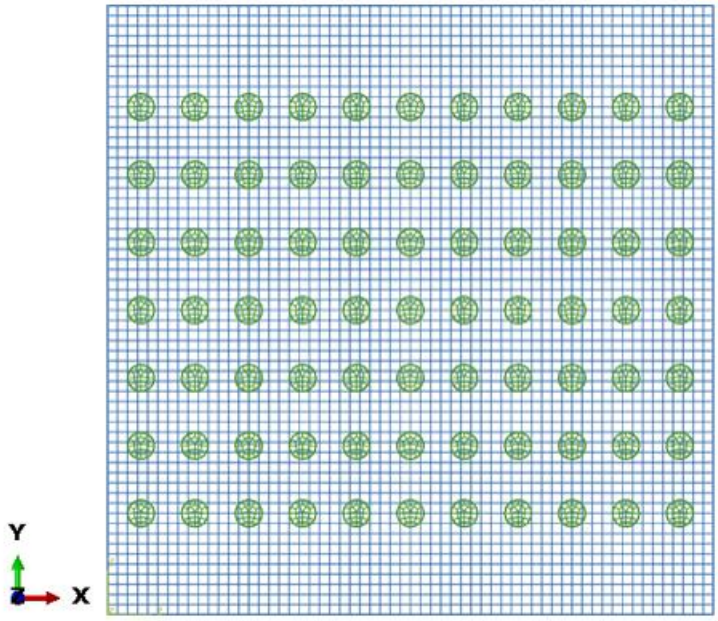

Figure 4.5 Example of meshing of the RVE model with aligned fiber, VF=10%, AR=20.

4.1.3 Boundary conditions

The symmetric boundary condition (SBC) is applied to three surfaces (S_1, S_2, and S_3 in Figure 4.6) of the RVE, which means that these three surfaces could shrink or expand in its parallel plane, but there is no displacement in its perpendicular direction. In the integrated software package we developed before, the RVE generation process is realized by Python code automatically. With the given fiber volume fraction, a RVE block is first created. Then the fibers are inserted following a modified random sequential adsorption (RSA) algorithm. It is unavoidable that some of the fibers may over-span the RVE through certain surface. In order to reach the target fiber volume fraction, the over-spanning fibers are cut and transferred to the opposite surface of the RVE. The geometric periodicity is ensured automatically for the ease application of the PBC, which is also controlled by Python code. However, for the RVE with the curved fibers, the fibers are generated first to ensure no overlapping. Then the RVE block is created to enclose those fibers. This process is realized manually since it is hard to write a Python code to control. Meanwhile, the SBC is ready in the Abaqus/CAE for application. In the literature, it was found the SBC is comparable to predict the elastic properties of the RVE model as the PBC (Xia et al., 2006).

Therefore, we choose to apply the SBC on the RVE to determine the longitudinal modulus of the RVE.

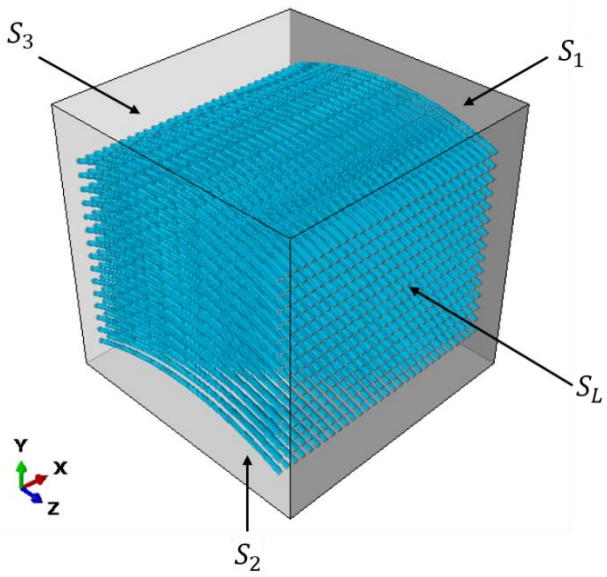

Figure 4.6 Example RVE with the surfaces applied boundary condition.

The displacements for the nodes on the surfaces of the RVE are listed in Table 4.2. The nodes on the other two surfaces not defined here are free to move. It should be mentioned that the applied displacement L_R can take any value since the material is chosen as elastic in Abaqus/CAE. The stress-strain curve will always be linear without any failure present.

Nodes on surface	Symmetric Plane	Translational DOF	Rotational DOF
S_1	X	$U_1 = 0$	$UR_2 = UR_3 = 0$
S_2	Y	$U_2 = 0$	$UR_1 = UR_3 = 0$
S_3	Z	$U_3 = 0$	$UR_1 = UR_2 = 0$
S_L		$U_3 = L_R$	

Table 4.2 The DOF of the nodes on the RVE surfaces for the symmetric boundary conditions.

Figure 4.7 shows an example of the RVE model before and after deformation, in which the fiber VF and AR are set as 15 % and 20, respectively. The deformation scale is 0.5 in Figure 4.7 and the deformation of the fibers is obvious. Fibers would approach to be aligned due to the displacement loading. Since the displacement loading is exactly the

length of RVE model, the strain of RVE could be determined as 100%, which is more convenient for the Young's modulus calculation. The elastic constant E_L for the RVE can be estimated as:

$$E_L = \frac{\frac{\sum F_R}{W_R H_R}}{Strain} \tag{4.2}$$

where $\sum F_R$ is the summation of the reaction force of all nodes on S_L.

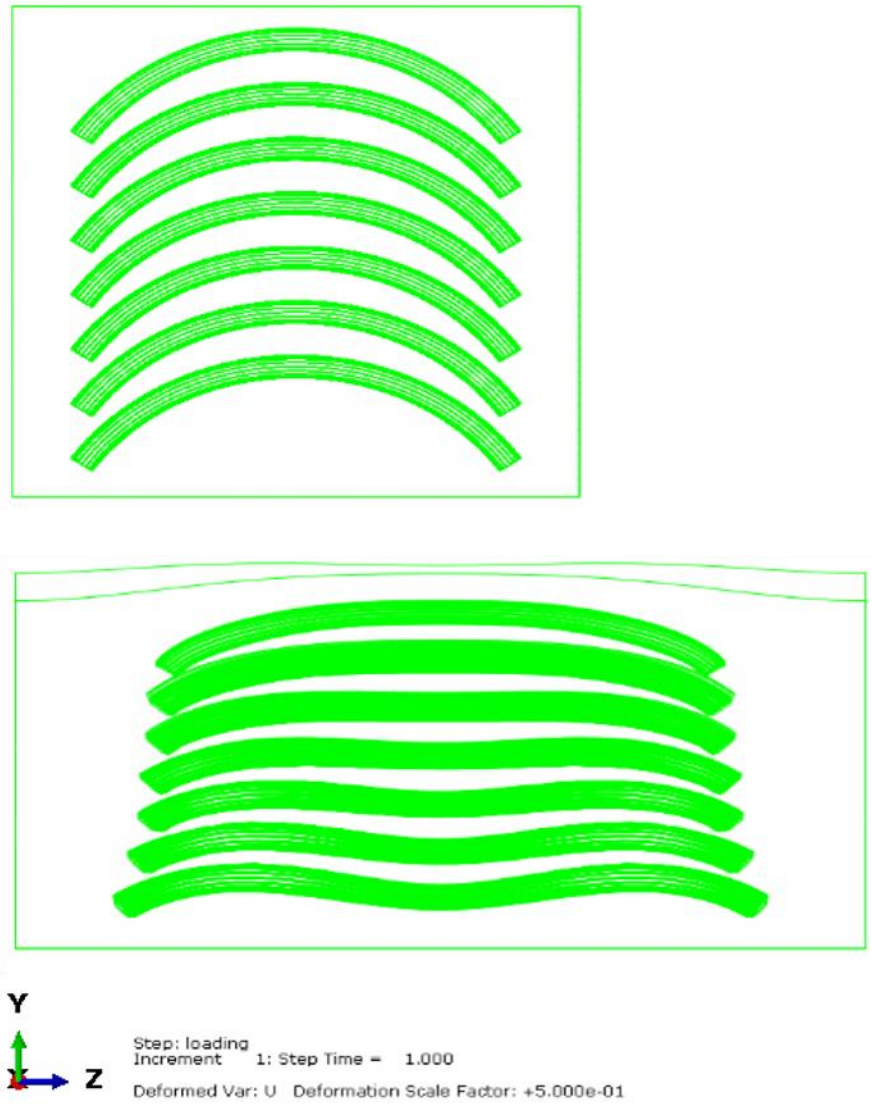

Figure 4.7 Illustration of a RVE before and after deformation.

4.1.4 Meshing convergence

Convergence is essential in the FE simulation to ensure the accuracy of the numerical simulation results. We use the same element size for both the matrix and the fibers in the embedded element technique. The element mesh sensitivity is investigated to show its effect on the computational results. As the element size decreases, the results are expected to reach the convergent solution. Since both the RVE size and the fiber separation distance are different for each model, the convergent process is checked for every case. Figure 4.8 shows an example of the convergent process for the RVE model with straight fibers (VF=10% and AR=20). When the number of the elements reaches around 150000, the solution is approaching to a stable value. The calculated result for the longitudinal Young's modulus using 150000 elements agrees very well with that from the output of the integrated software package where different type of elements are used.

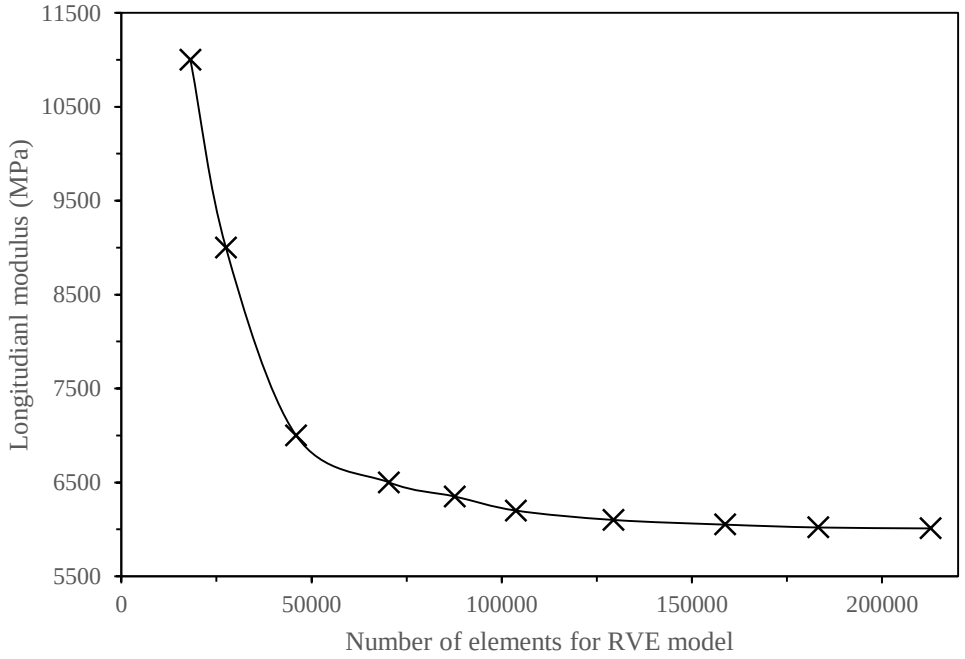

Figure 4.8 Variation of the Young's modulus E_L with the increasing element number (fiber VF=10%, AR=20).

4.2 Results and discussion

After the convergence of the numerical results is confirmed, the longitudinal Young's modulus for the G/DFRC with curved fibers is first determined for the composites with different fiber volume fraction and true fiber aspect ratio. The results are then compared with those from the database of the integrated software package in order to see the fiber curvature effects. Through data fitting, the fiber curvature effect can be represented by an effective fiber aspect ratio. A diagram or a database for the effective fiber aspect ratio is obtained for the G/DFRC with given volume fraction, true fiber aspect ratio and fiber curvature angle. For the DFRC with straight fibers, the true fiber AR will be taken as the input directly for the integrated software package to predict the elastic properties of the composites. While for the DFRC with curved fibers, the effective fiber AR will be extracted from the diagram or the database and input into the integrated software package for further calculation.

4.2.1 Effects of fiber curvature on the longitudinal Young's modulus

FE analysis is performed on the RVE models for different cases, and the calculated longitudinal Young's modulus is summarized in Table 4.3. It is observed that when the fiber volume fraction and the fiber true AR are fixed, the fiber curvature has significant effects upon the longitudinal Young's modulus and demonstrates a similar tendency for all the cases. Take the RVE model (VF=10 %, AR=20) for an example, when the fiber curvature is zero which means that all fibers are straightly aligned, the RVE model yields the highest Young's modulus, i.e., 6050.32 MPa. When the fiber curvature angle is increased to 31.62º and 60.36º, the predicted results drop to 5584.88 MPa and 4450.65 MPa respectively. According to the previous research (Chan & Wang, 1994; Gigante et al., 2017; Velmurugan et al., 2014), the effective or projected fiber length in the longitudinal direction is the major factor that affects the longitudinal modulus of composites. With the increase of the fiber curvature angle, the projected fiber length along the longitudinal direction decreases, which contribute to the reduction of the Young's modulus in this direction.

VF	Fiber curvature angle θ(degree)	Young's modulus E_L (MPa) from FEM			
		AR=20	AR=50	AR=60	AR=100
10 %	0.00	6050.32	6933.23	7159.40	7419.21
	22.27	5863.27	6612.93	6846.48	6944.57
	31.62	5584.88	6312.33	6446.94	6661.99
	38.88	5330.28	6039.54	6122.86	6381.00
	45.07	5177.98	5812.52	5931.00	6023.26
	50.60	5000.04	5593.80	5683.85	5793.04
	55.65	4727.25	5322.69	5442.70	5573.79
	60.36	4450.65	4962.58	5018.00	5127.43
15 %	0.00	8461.80	10209.12	10731.40	10944.30
	22.27	6913.74	8802.59	9530.30	9876.37
	31.62	6454.36	7402.30	7790.32	8577.74
	38.88	6126.11	6887.26	7317.36	7975.22
	45.07	5959.44	6435.98	6846.64	7137.77
	50.60	5687.42	6062.33	6223.49	6498.80
	55.65	5339.47	5634.88	5717.47	6090.68
	60.36	4910.15	5232.62	5433.32	5777.16

Table 4.3 FE predicted longitudinal Young's modulus E_L for the RVE model with curved fibers

To present the simulation data in Table 4.3 more efficiently, a normalized Young's modulus is defined as,

$$E_N = \frac{E_L \; for \; RVE \; with \; curved \; fiber}{E_L \; for \; RVE \; with \; the \; straight \; fiber} \tag{4.3}$$

The variation of the normalized Young's modulus with the fiber curvature angle is plotted in Figure 4.9 when the fiber volume fraction is fixed as 10%. It is clearly demonstrated that the curved fibers induce a reduction in the longitudinal Young's modulus as the normalized value is always less than 1. It is also found that the reduction effect of the curved fibers on

the longitudinal Young's modulus depends on the true aspect ratio of the fibers, i.e., the curved fibers with larger true aspect ratio will induce more induction in the material properties along the longitudinal direction.

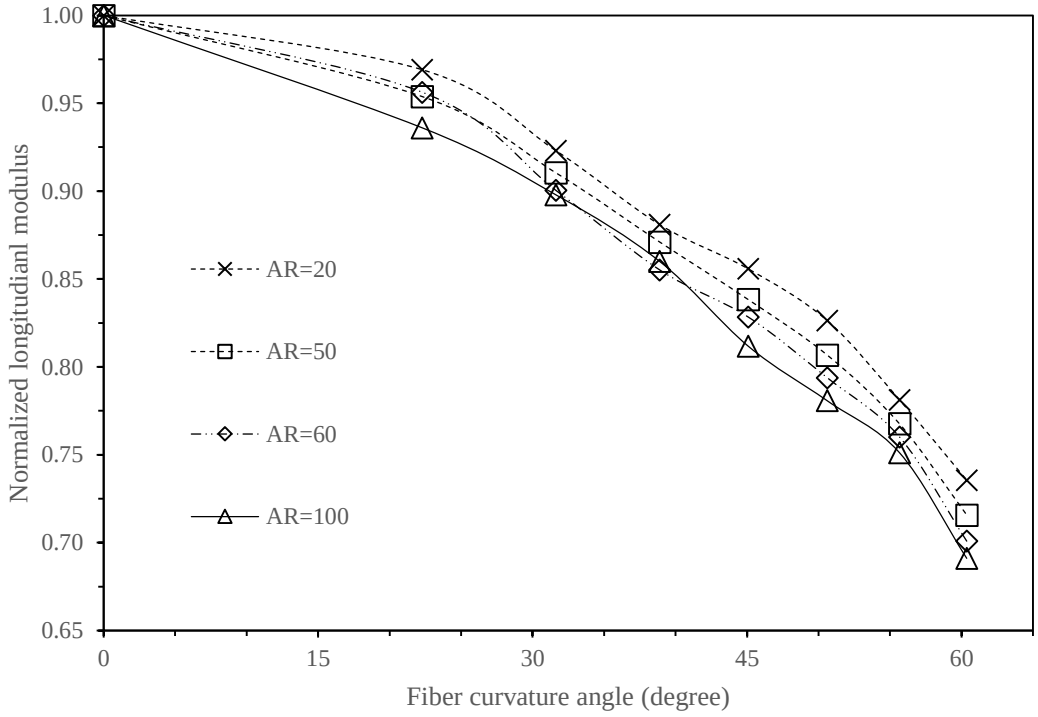

Figure 4.9 Variation of the normalized longitudinal Young's modulus with fiber curvature angle for different fiber AR (VF=10%).

The reduction effect of the curved fibers on the longitudinal Young's modulus of the G/DFRC may also be influenced by the fiber volume fraction. Figure 4.10 is plotted for this purpose when the fiber AR is fixed as 20. It is found that for the RVE model with the same fiber AR and fiber curvature angle, the higher fiber volume fraction in the RVE would lead a larger reduction in the longitudinal modulus. The reason behind it is that for the RVE with higher fiber VF, there are more fibers in the RVE and the accumulative effect of the curved fibers will be more significant upon the elastic properties of the RVE. Similar results were observed in the literature (Velmurugan et al., 2014).

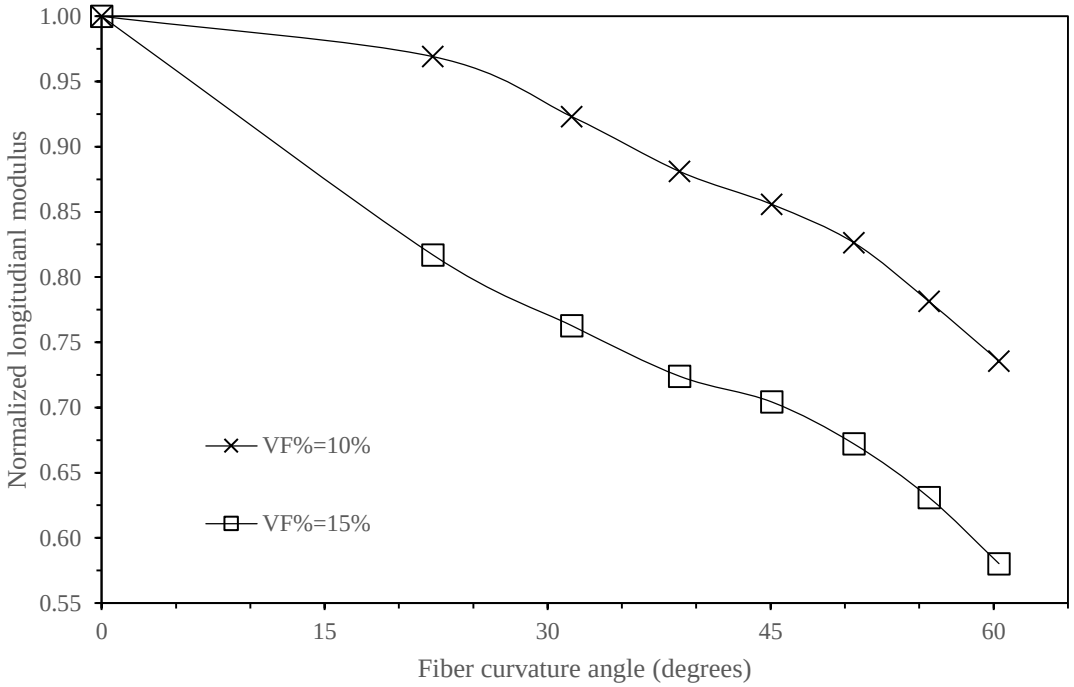

Figure 4.10 Variation of the normalized longitudinal Young's modulus with fiber curvature angle for different fiber VF (AR=20).

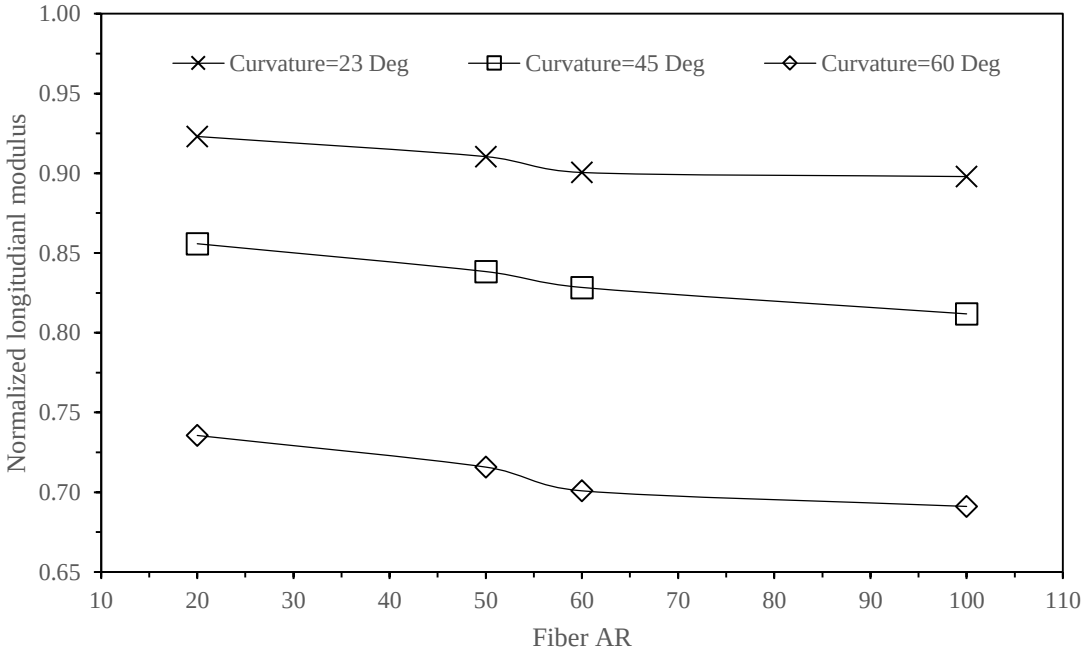

Figure 4.11 Influence of fiber AR and fiber curvature angle on the normalized longitudinal Young's modulus, fiber VF=10%.

Figure 4.11 shows the variation of the normalized Young's modulus with the fiber true AR considering different fiber curvature angle, i.e., 23º, 45º and 60º, respectively. It is found that the fiber true AR has a slight effect on the property reduction. In reality, for the composites with high AR fibers, the elastic property reduction caused by the curved fibers is expected to be more. As argued by Bapanapalli & Nguyen (2008) and Velmurugan et al. (2014), the fibers with higher AR will have more chance to be curved and form fiber bundle, which will affect the elastic properties of the composites more. However, it should be mentioned that in our preliminary FE analysis, the chance of forming curved fibers is not considered. Therefore, the trend of the fiber AR and fiber curvature effects on the elastic properties of the composites as shown in Figure 4.11 is reasonable. Once we get the detailed information on the fiber curvature from imaging, and the proportion of the fibers with curvature is extracted, we expect to give more accurate prediction on the elastic properties of the composites.

4.2.2 Effective fiber AR

From the previous FE analysis, it is found that when the fiber volume fraction is fixed, the predicted longitudinal Young's modulus E_L reduces as the fiber curvature angle increases. The increase of the fiber curvature is equivalent to reduce the projected fiber length. Meanwhile, it is commonly accepted that the longitudinal Young's modulus for the composites with aligned fibers also reduce as the decreasing of the fiber AR. Therefore, there should exist an effective fiber AR that can reflect the effects of the fiber curvature. This effective fiber AR can be used to calibrate the predicted longitudinal Young's modulus of the composites with aligned fibers without considering the fiber curvature effects. During the injection molding process, the fiber bundle may occur, there would be some curved fibers in the DFRC. Once the information about the curved fibers is given, we can convert the curvature of the fibers into the effective fiber AR. This effective fiber AR will be imported into the integrated software package, and the elastic properties of the DFRC with curved fibers could be calculated automatically. The determination of the effective fiber AR is elaborated in the following.

Fiber AR	5	10	15	20	50	60	80	100
E_L (GPa) VF=10%	3.05	4.19	5.09	5.91	6.91	7.11	7.23	7.34
E_L (GPa) VF=15%	3.88	6.10	7.40	8.55	10.21	10.61	10.70	10.95

Table 4.4 The longitudinal Young's modulus E_L of the RVE model with straight fibers predicted by the integrated software package.

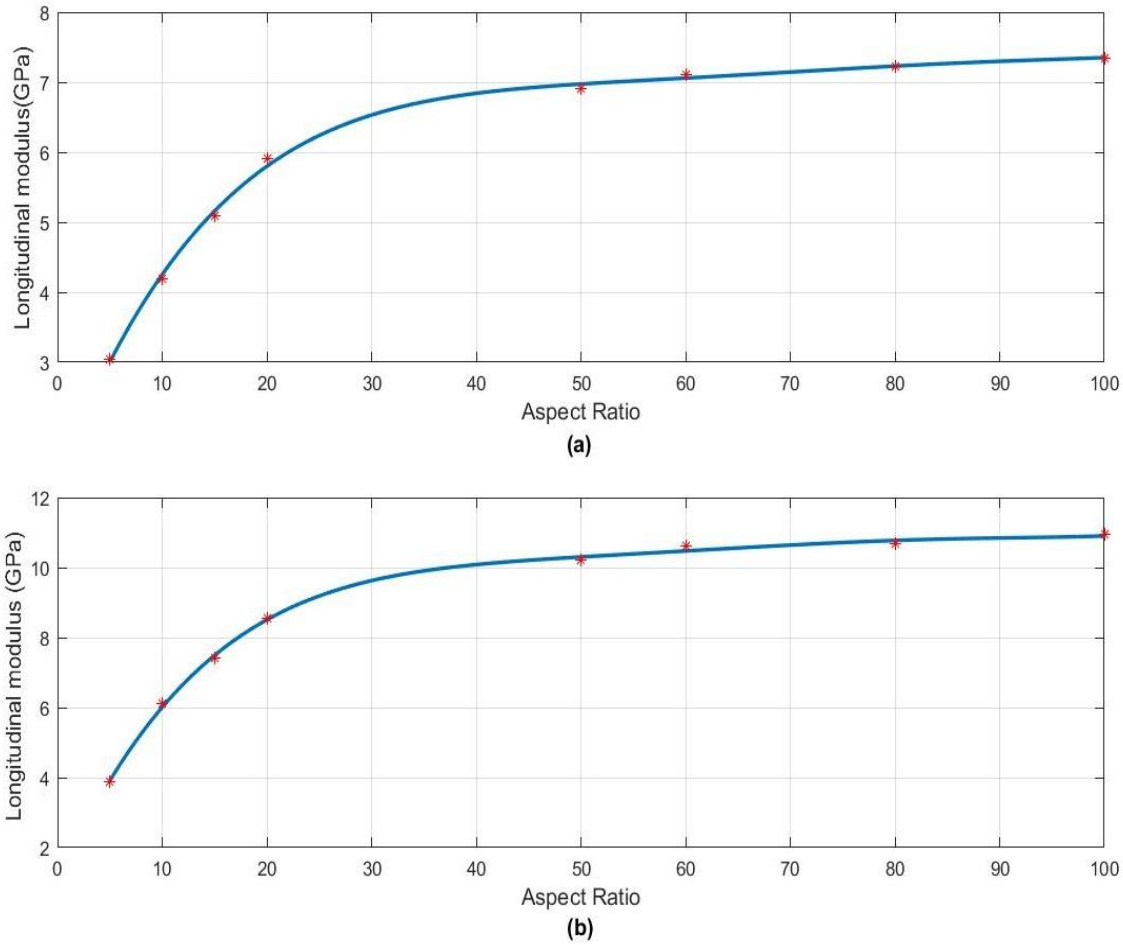

Figure 4.12 The fitting curve for the longitudinal Young's modulus E_L of the G/DFRC with straight fibers, (a) VF=10%, (b) VF=15%.

The longitudinal modulus E_L of the RVE models with curved fibers is calculated and listed in Table 4.3, in which four sets of true AR (20, 50, 60, and 100) are studied to see the fiber curvature effects. From the integrated software package, for each of fixed fiber volume

fraction (10 % and 15 %), the code is run for eight sets of fiber AR and the predicted Young's modulus is summarized in Table 4.4. It should be mentioned that the fiber VF cannot be controlled to the exact value of the target, therefore, totally five RVE models are created for each case and the results are averaged to show in Table 4.4. These data can be used further to do data fitting and get a longitudinal Young's modulus-Aspect ratio curve for the whole range of fiber AR (from 5 to 100), which is shown in Figure 4.12. The whole set of data has been previously saved in the database of the integrated software package.

Fiber curvature angle	0º	22.3º	31.6º	38.9º	45.1º	50.6º	55.7º	60.4º
Effective AR for VF=10%	20.0	18.6	17.3	16.2	15.1	14.0	12.4	11.0
	50.0	31.9	26.1	22.5	20.1	18.2	16.1	13.8
	60.0	40.3	28.3	23.5	21.3	19.0	17.0	14.5
	100.0	47.2	33.2	27.2	22.3	19.9	18.0	15.8
Fiber curvature angle	0º	22.3º	31.6º	38.9º	45.1º	50.6º	55.7º	60.4º
Effective AR for VF=15%	20.0	11.8	10.4	9.5	9.1	8.3	7.5	6.5
	50.0	20.0	13.5	11.8	10.4	9.3	8.2	7.2
	60.0	25.5	15.0	13.2	11.6	9.8	8.4	7.7
	100.0	29.4	18.7	15.8	12.6	10.6	9.4	8.6

Table 4.5 Effective fiber AR for the RVE model with typical curvature angle, for fiber VF of 10% and 15%.

Based on the longitudinal Young's modulus calculated from the RVE model with curved fibers as shown in Table 4.3, a looped code is then developed in the Matlab to fit these data with the curves in Figure 4.12 to extract the effective fiber AR of the curved fibers in the RVE. The Matlab code is provided in the Appendix B and the fitted results are shown in Table 4.5. For the RVE model with the fiber curvature angle 0º, the effective fiber AR and the true fiber AR is the same. By using the effective AR, the RVE model with curved fibers could be treated as the RVE with straight fibers in the integrated software package. The

reduction of the elastic constant E_L caused by the fiber curvature has been transferred to the fiber effective AR successfully.

The effective fiber AR due to the fiber curvature effect for four typical cases are plotted in Figure 4.13. As expected, these four sets of results show a similar trend, i.e., the effective AR decreases as the increasing of the curvature angle for the RVE model with a fixed fiber volume fraction and a true fiber AR.

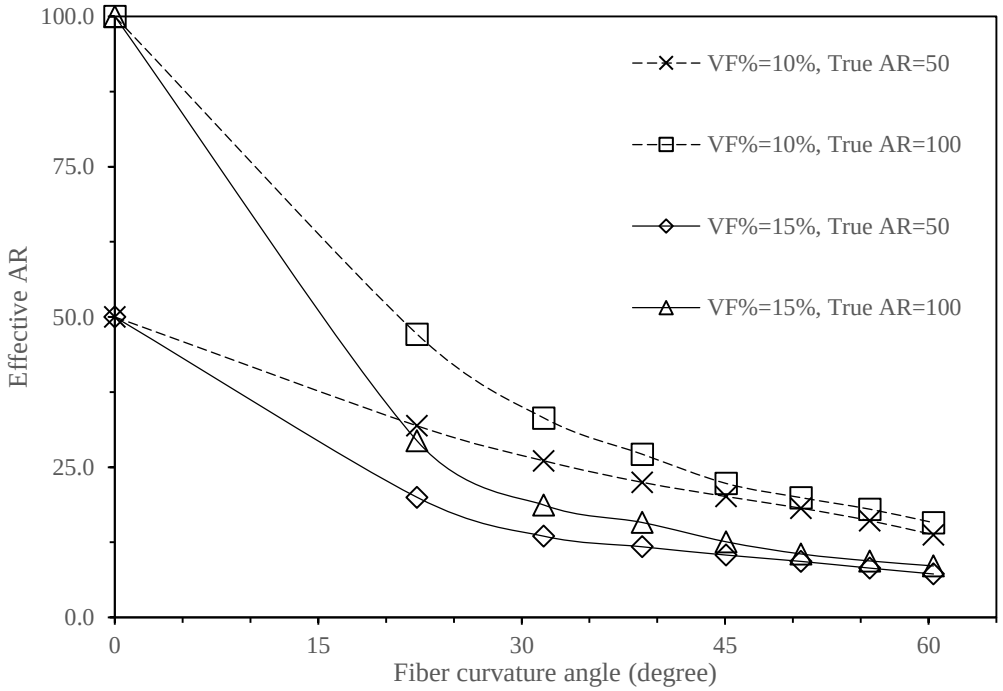

Figure 4.13 The effective fiber AR versus fiber curvature angle for the RVE models with different fiber VF and true fiber AR

The data in Table 4.5 can be further managed to do the data fitting in 3-D format, in which the effective fiber aspect ratio is expressed in terms of the true fiber aspect ratio and the fiber curvature angle for the DFRC with fixed fiber volume fraction. The data fitting is done by the toolbox in the Matlab and a 3rd order polynomial is selected as

$$z(x,y) = p_{00} + p_{10}\cdot x + p_{01}\cdot y + p_{20}\cdot x^2 + p_{11}\cdot x\cdot y + p_{02}\cdot y^2 + p_{21}\cdot x^2\cdot y + p_{12}\cdot x\cdot y^2 + p_{03}\cdot y^3 \quad (4.4)$$

where x, y, and z represent the true fiber AR, the fiber curvature angle and the effective fiber AR, respectively. These fitting coefficients for both sets of fiber VF (10% and 15%) are shown in Table 4.6 with R-square value of 0.9828 and 0.9923 respectively.

p_{mn}	VF=10 %	VF=15 %
p_{00}	-3.439	0.035
p_{10}	1.172	1.012
p_{01}	0.429	0.096
p_{20}	-1.602×10^{-3}	-1.650×10^{-4}
p_{11}	-0.032	-0.037
p_{02}	-0.002	9.975×10^{-3}
p_{21}	-2.258×10^{-5}	7.331×10^{-6}
p_{12}	3.430×10^{-4}	3.383×10^{-4}
p_{03}	-7.938×10^{-5}	1.647×10^{-4}

Table 4.6 Polynomial coefficients in 3-D data fitting for the effective fiber aspect ratio (VF=10% and VF=15%)

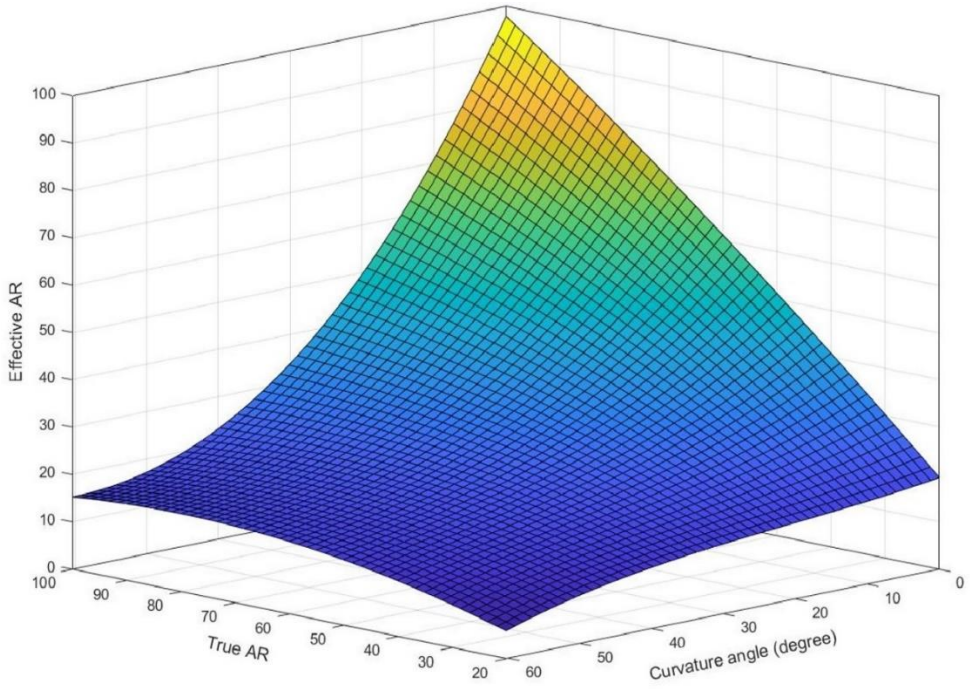

Figure 4.14 Effective fiber AR for composites with VF = 10% to be used in the integrated software package.

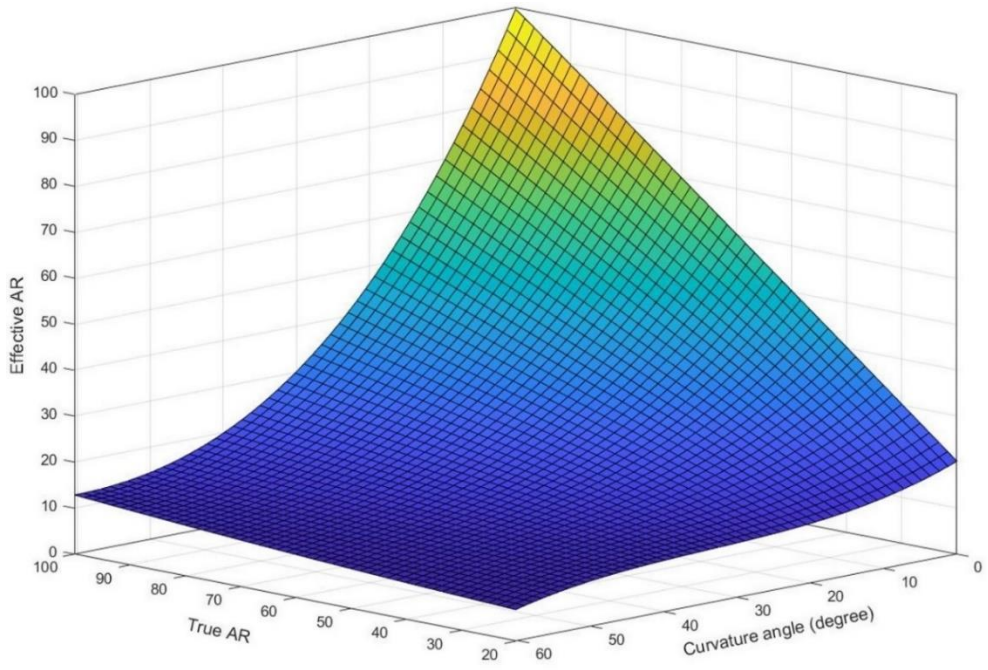

Figure 4.15 Effective fiber AR for composites with VF =15% to be used in the integrated software package.

With these parameters, the 3-D fitting surfaces are shown in Figure 4.14 and 4.15. The fitting surface can be saved as a database and be incorporated into the integrated software package. This database can determine the effective fiber AR for the RVE models with curved fibers, if the true fiber aspect ratio, fiber curvature angle and fiber volume fraction are given. This effective fiber AR will be input back to the integrated software package to output the elastic constants of the composites with the consideration of the fiber curvature effects.

The accuracy of the effective fiber AR database can be improved by adding more sets of data for fitting the 3-D surface. It also depends on how accuracy the fiber curvature could be determined. For example, in the literature, both analytical and experimental methods have been developed to calculate the fiber curvature in the composite (El Kadi, 2006; Goldman, 2005; Suhir et al., 1991). It is commonly accepted that the Microscopy-based method may be a feasible way to determine the fiber curvature. However, there is still a lack of study in characterizing the fiber curvature and this field does need further investigation.

Chapter 5

5 Conclusions, contributions and future work

5.1 Conclusions and contributions

The injection molded DFRC are getting larger share on the market of composites due to their significant weight reduction, relatively high mechanical performance, low cost, ease of manufacturing and integrating complex parts. In order to fulfill the applications of the DFRC efficiently and reduce the expensive experiment cost, a more accurate and realistic numerical model (integrated software package) is developed in this work to predict the elastic properties of the DFRC. As reviewed in Chapter 1, there are many factors that may have significant effects on the elastic properties of the DFRC. The fiber volume fraction gradient, as well as the fiber curvature effects are fully investigated to calibrate the numerical simulation results. The conclusions and contributions of this work are summarized in this section.

1. Based on micromechanics modeling and finite element analysis, an integrated software package is developed to predict the elastic properties of the DFRC. Four major influence factors are assigned as the inputs in this package, including the elastic properties of the constituents of the composite, the fiber volume fraction, the fiber AR, and the fiber orientation tensor, respectively. The integrated software package consists of two modules, one is for the prediction of the elastic properties of composites with aligned fibers and the other one is for the composites with oriented fibers through orientation averaging. The merit of this integrated software package is that it can be run automatically to map the elastic properties of the composite parts with the afore-mentioned inputs. Some findings are listed in the following:
    - The elastic properties predicted by the integrated software package are compared to the tensile tests data, and good agreement is found for most specimens except some from particular locations of the DFRC plaque.

- For both G/DFRC and C/DFRC plaques, it is found that the predicted results have higher difference with the testing data for the plaques with higher fiber volume fraction.

2. Combining the microscopy-based measurement and image pixel analysis, the fiber volume fraction gradient through the thickness of the plaque is obtained. The fiber volume fraction gradient is considered in the integrated software package to calibrate the numerical simulation. It is found that,
   - The fiber volume fraction gradient is more obvious in the DFRC plaque with the higher fiber volume fraction.
   - With the consideration of the fiber volume fraction gradient through the plaque thickness, the numerical results are more accurate compared with the experimental data.
3. Based on the FE analysis (Abaqus/CAE), the effects of the fiber curvature on the elastic properties of the DFRC are investigated. To consider the fiber curvature effects in the integrated software package, the curved fibers are treated as the straight fibers with a reduced effective fiber AR, which is determined through data fitting with the output of the 1st module of the integrated software package.
   - When the fiber volume fraction and the true fiber AR are fixed, the longitudinal modulus of the DFRC decreases as the increasing of the fiber curvature angle. Correspondingly, the effective fiber AR will also decrease.
   - It is also found that there will be more longitudinal modulus reduction due to the fiber curve effects for the composites with higher fiber volume fraction.

5.2 Recommendations for future work

This work attempts to develop a more accurate and realistic package to predict the elastic constants of the injection molded DFRC. The investigation on the effects of the fiber volume fraction gradient and the fiber curvature are expected to be helpful for improving the accuracy of the integrated software package. However, there are still some potential error sources and limitations for this developed integrated software package. Therefore, some suggestions for the future work are listed as follows:

1. It should be mentioned that in Chapter 3 when we investigated the fiber curve effects, it is assumed that all the fibers are curved in the same direction. However, from the microscopic images, it is found that the curvature patterns are not aligned such perfectly. Therefore, more image analysis should be performed to get a more accurate fiber curvature information. This information will be used for the calibration of the effective fiber AR more accurately.
2. In the integrated software package, the voids effect on the elastic properties should be considered. Voids are commonly formed during the manufacturing process of the composite materials, which have detrimental effects on the elastic properties of the composite materials. The volume fraction, size, shape, and the distribution are the interested characteristics of voids (Bowles & Frimpong, 1992; Bréard et al., 2003; Huang & Talreja, 2005; Patel & Lee, 1996; Vallittu, 1995). Further FE analysis on the RVE model with the consideration of the void effects should be performed.
3. The strength of the injection molded DFRC is also a significant mechanical property needs to be considered. The factors such as the constituent properties, the fiber volume fraction, the fiber AR, the fiber/matrix interfacial properties, and the fiber orientation distribution will have significant effects on the strength of the DFRC (Nguyen & Paquette, 2010; Rezaei et al., 2009). One limitation of the developed integrated software package is that some methodologies used are only suitable for predicting the elastic properties of the DFRC, such as the semi-empirical formulation for the composites with aligned fibers and the orientation averaging method (Advani & Tucker, 1987). Therefore, the fiber orientation distribution function should be first recovered from the fiber orientation tensor, which is further used to generate the RVE model with oriented fibers for strength analysis of the DFRC.

References

ABAQUS, C. (2012). Analysis user's manual, Version 6.12.

Abd El-Rahman, A. I., & Tucker, C. L. (2013). Mechanics of Random Discontinuous Long-Fiber Thermoplastics—Part I: Generation and Characterization of Initial Geometry. Journal of Applied Mechanics, 80(5), 51007.

Abdulmajeed, A. A., Närhi, T. O., Vallittu, P. K., & Lassila, L. V. (2011). The effect of high fiber fraction on some mechanical properties of unidirectional glass fiber-reinforced composite. Dental Materials, 27(4), 313–321.

Adams, D. F. (1987). Engineering composite materials. Composites, 18(3), 261.

Advani, S. G., & Tucker, C. L. (1987). The Use of Tensors to Describe and Predict Fiber Orientation in Short Fiber Composites. Journal of Rheology, 31(8), 751–784.

Advani, S. G., & Tucker, C. L. (1990). Closure approximations for three ‐ dimensional structure tensors. Journal of Rheology, 34(3), 367 ‐ 386.

Ajit D. kelkar. (2009). Characterization and Structural Behavior of Braided Composites. Stress: The International Journal on the Biology of Stress, (January), 181.

Aleksendrić, D., & Carlone, P. (2015). Introduction to composite materials. Soft Computing in the Design and Manufacturing of Composite Materials, 1–5.

Altan, M. C., Subbiah, S., Guceri, S. I., & Pipes, R. B. (1971). Numerical Prediction of Three-Dimensional Fiber, 30(74).

Asp, L. E., & Greenhalgh, E. S. (2014). Structural power composites. Composites science and technology, 101, 41-61.

ASTM International. (2010a). ASTM D3171-15. Standard Test Methods for Constituent Content of Composite Materials. Annual Book of ASTM Standards, (May 2009), 1–6.

ASTM International. (2010b). D 3171 - Standard Test Methods for Constituent Content of Composite Materials. Annual Book of ASTM Standards, 76(February), 1–6.

Bapanapalli, S., & Nguyen, B. N. (2008). Prediction of elastic properties for curved fiber polymer composites. Polymer Composites, 29(5), 544–550.

Barkoula, N. M., Alcock, B., Cabrera, N. O., & Peijs, T. (2008). Fatigue properties of highly oriented polypropylene tapes and all-polypropylene composites. Polymers and Polymer Composites, 16(2), 101–113.

Blanc, R., Germain, C., Da Costa, J. P., Baylou, P., & Cataldi, M. (2006). Fiber orientation measurements in composite materials. Composites Part A: Applied Science and Manufacturing, 37(2), 197–206.

Bledzki, a K., & Faruk, O. (2004). Wood fiber reinforced polypropylene composites: Compression and injection molding process. Polymer - Plastics Technology and Engineering, 43(3), 871–888.

Bowles, K. J., & Frimpong, S. (1992). Void Effects on the Interlaminar Shear Strength of Unidirectional Graphite-Fiber-Reinforced Composites, (10).

Bréard, J., Saouab, A., & Bouquet, G. (2003). Numerical simulation of void formation in LCM. Composites Part A: Applied Science and Manufacturing, 34(6 SPEC.), 517–523.

Callister, W. D. (2006). Composites. Materials Science and Engineering: An Introduction, 7th Edition, 577–620.

Campbell, F. C. (2010). Structural Composite. Structural Composite Materials, 31–61.

Cann, M. T., Adams, D. O., & Schneider, C. L. (2008). Characterization of Fiber Volume Fraction Gradients in Composite Laminates. Journal of Composite Materials, 42(5), 447–466.

Chan, W. S., & Wang, J. S. (1994). Influence of Fiber Waviness on the Structural Response of Composite Laminates. Journal of Thermoplastic Composite Materials, 7(3), 243–260.

Chawla, K. K. (2012). Composite Materials. Advanced Materials by Design, 73.

Chung, D. H., & Kwon, T. H. (2001). Improved model of orthotropic closure approximation for flow induced fiber orientation. Polymer Composites, 22(5), 636–649.

Chung, D. H., & Kwon, T. H. (2002). Invariant-based optimal fitting closure approximation for the numerical prediction of flow-induced fiber orientation. Journal of Rheology, 46(1), 169–194.

Cintra, J. S., & Tucker, C. L. (1995). Orthotropic closure approximations for flow‐induced fiber orientation. Journal of Rheology, 39(6), 1095‐1122.

D'Almeida, J., Mauricio, M., & Paciornik, S. (2012). Evaluation of the cross-section of lignocellulosic fibers using digital microscopy and image analysis. Journal of Composite Materials, 46(24), 3057–3065.

Dmitri Kopeliovich. (2014). Injection molding of polymers. Retrieved from http://www.substech.com/dokuwiki/doku.php?id=injection_molding_of_polymers

Doghri, I., & Tinel, L. (2006). Micromechanics of inelastic composites with misaligned inclusions: Numerical treatment of orientation. Computer Methods in Applied Mechanics and Engineering, 195(13–16), 1387–1406.

Drugan, W. J., & Willis, J. R. (1996). A micromechanics-based nonlocal constitutive equation and estimates of representative volume element size for elastic composites. Journal of the Mechanics and Physics of Solids, 44(4), 497–524.

Dupret, F., & Verleye, V. (1999). Modelling the flow of fiber suspensions in narrow gaps. Rheology Series, 8(C), 1347–1398.

Eberhardt, C., Clarke, A., Vincent, M., Giroud, T., & Flouret, S. (2001). Fibre-orientation measurements in short-glass-fibre composites—II. Composites Science and Technology, 61(10), 1389–1400.

El Kadi, H. (2006). Modeling the mechanical behavior of fiber-reinforced polymeric composite materials using artificial neural networks—A review. Composite Structures, 73(1), 1–23.

Fisher, F. T., Bradshaw, R. D., & Brinson, L. C. (2003). Fiber waviness in nanotube-reinforced polymer composites-I: Modulus predictions using effective nanotube properties. Composites Science and Technology, 63(11), 1689–1703.

Fu, S., Lauke, B., & Edith, M. a. (2006). Hybrid effects on tensile properties of hybrid short-glass-fiber-and short-carbon-fiber- reinforced polypropylene composites. Advanced Materials, 6, 1243–1251.

Fu, S. Y., & Lauke, B. (1996). Effects of fiber length and fiber orientation distributions on the tensile strength of short-fiber-reinforced polymers. Composites Science and Technology, 56(10), 1179–1190.

Fu, S. Y., Lauke, B., Mäder, E., Yue, C. Y., & Hu, X. (2000). Tensile properties of short-glass-fiber- and short-carbon-fiber-reinforced polypropylene composites. Composites Part A: Applied Science and Manufacturing, 31(10), 1117–1125.

Gigante, V., Aliotta, L., Phuong, V. T., Coltelli, M. B., Cinelli, P., & Lazzeri, A. (2017). Effects of waviness on fiber-length distribution and interfacial shear strength of natural fibers reinforced composites. Composites Science and Technology, 152, 129–138.

Goldman, R. (2005). Curvature formulas for implicit curves and surfaces. In Computer Aided Geometric Design (Vol. 22, pp. 632–658).

Guild, F. J., & Summerscales, J. (1993). Microstructural image analysis applied to fibre composite materials: a review. Composites, 24(5), 383–393.

Affdl, J. H., & Kardos, J. L. (1976). The Halpin‐Tsai equations: a review. Polymer Engineering & Science, 16(5), 344-352.

Harper, L. T., Qian, C., Turner, T. A., Li, S., & Warrior, N. A. (2012a). Representative volume elements for discontinuous carbon fibre composites - Part 2: Determining the critical size. Composites Science and Technology, 72(2), 204–210.

Harper, L. T., Qian, C., Turner, T. A., Li, S., & Warrior, N. A. (2012b). Representative volume elements for discontinuous carbon fibre composites - Part 2: Determining the critical size. Composites Science and Technology, 72(2), 204–210.

Hill, R. (1963). Elastic properties of reinforced solids: Some theoretical principles. Journal of the Mechanics and Physics of Solids, 11(5), 357–372.

Hine, P. J., Rudolf Lusti, H., & Gusev, A. A. (2002). Numerical simulation of the effects of volume fraction, aspect ratio and fibre length distribution on the elastic and thermoelastic properties of short fibre composites. Composites Science and Technology, 62(10–11), 1445–1453.

Houshyar, S., Shanks, R. A., & Hodzic, A. (2005). The effect of fiber concentration on mechanical and thermal properties of fiber-reinforced polypropylene composites. Journal of Applied Polymer Science, 96(6), 2260–2272.

Huang, H., & Talreja, R. (2005). Effects of void geometry on elastic properties of unidirectional fiber reinforced composites. Composites Science and Technology, 65(13), 1964–1981.

ISO, E. (1997). 527-4. Plastics-Determination of tensile properties-Part 4: Test conditions for isotropic and orthotropic fibre-reinforced plastic composites. International Organization for Standardization (ISO), Geneva, Switzerland.

Jagannatha, T. D., Harish, G., & Author, C. (2015). Mechanical Properties of Carbon/Glass Fiber Reinforced Epoxy Hybrid Polymer Composites. Int. J. Mech. Eng. & Rob. Res, 4(2).

Kanit, T., Forest, S., Galliet, I., Mounoury, V., & Jeulin, D. (2003). Determination of the size of the representative volume element for random composites: Statistical and numerical approach. International Journal of Solids and Structures, 40(13–14), 3647 – 3679.

Karsli, N. G., & Aytac, A. (2013). Tensile and thermomechanical properties of short carbon fiber reinforced polyamide 6 composites. Composites Part B: Engineering, 51, 270–275.

Kepnang, A. N., Berthet, F., & Castanie, B. (2009). Parameters affecting mechanical properties of composite manufactured by Liquid Resin Infusion (LRI). The 17th International Conference of Composite Materials (ICCM).

Kim, E. G., Park, J. K., & Jo, S. H. (2001). A study on fiber orientation during the injection molding of fiber-reinforced polymeric composites: (Comparison between image processing results and numerical simulation). Journal of Materials Processing Technology, 111(1–3), 225–232.

Kim, H. S. (2000). On the rule of mixtures for the hardness of particle reinforced composites. Materials Science and Engineering A, 289(1–2), 30–33.

Kunc, V., Case, S. W., Santos-Villalobos, H. J., & Simunovic, S. (2015). The stiffness tensor for composites with curved discontinuous fibers. Composites Part A: Applied Science and Manufacturing, 72, 239–248.

Liu, H., Zeng, D., Li, Y., & Jiang, L. (2016). Development of RVE-embedded solid elements model for predicting effective elastic constants of discontinuous fiber reinforced composites. Mechanics of Materials, 93, 109–123.

Ltd., R. and J. B. (2002). Grinding and polishing machine. Journal of Scientific Instruments, 34(11), 468–469.

Lu, Z., Yuan, Z., & Liu, Q. (2014). 3D numerical simulation for the elastic properties of random fiber composites with a wide range of fiber aspect ratios. Computational Materials Science, 90, 123–129.

McDonough, W. G., Hunston, D. L., & Dunkers, J. P. (2004). Test Method for Constituent Content of Composite Materials. ASTM Int, 1(3), 1-15.

Mortazavian, S., & Fatemi, A. (2015). Effects of fiber orientation and anisotropy on tensile strength and elastic modulus of short fiber reinforced polymer composites. Composites Part B: Engineering, 72, 116–129.

Nguyen, B. N., Bapanapalli, S. K., Holbery, J. D., Smith, M. T., Kunc, V., Frame, B. J., … Tucker, C. L. (2008). Fiber length and orientation in long-fiber injection-molded thermoplastics - Part I: Modeling of microstructure and elastic properties. Journal of Composite Materials, 42(10), 1003–1029.

Nguyen, B. N., & Paquette, J. (2010). EMTA's Evaluation of the Elastic Properties for Fiber Polymer Composites Potentially Used in Hydropower Systems. US Department of Energy (DOE), PNNL–19729.

Nguyen, V. D., Béchet, E., Geuzaine, C., & Noels, L. (2012). Imposing periodic boundary condition on arbitrary meshes by polynomial interpolation. Computational Materials Science, 55, 390–406.

Nguyen Thi, T. B., Morioka, M., Yokoyama, A., Hamanaka, S., Yamashita, K., & Nonomura, C. (2015). Measurement of fiber orientation distribution in injection-molded short-glass-fiber composites using X-ray computed tomography. Journal of Materials Processing Technology, 219, 1–9.

Notta-Cuvier, D., Lauro, F., & Bennani, B. (2014). An original approach for mechanical modelling of short-fibre reinforced composites with complex distributions of fibre orientation. Composites Part A: Applied Science and Manufacturing, 62, 60–66.

Ostoja-Starzewski, M. (2006). Material spatial randomness: From statistical to representative volume element. Probabilistic Engineering Mechanics, 21(2), 112–132.

Paciornik, S., & d'Almeida, J. (2010). Digital microscopy and image analysis applied to composite materials characterization. Matéria (Rio de Janeiro), 15(2), 172-181.

Pan, N. (1993). Theoretical determination of the optimal fiber volume fraction and fiber-matrix property compatibility of short fiber composites. Polymer Composites, 14(2), 85–93.

Panthapulakkal, S., & Sain, M. (2007). Injection-molded short hemp fiber/glass fiber-reinforced polypropylene hybrid composites -mechanical, water absorption and thermal properties. Journal of Applied Polymer Science, 103(4), 2432–2441.

Patel, N., & Lee, L. J. (1996). Modeling of void formation and removal in liquid composite molding. Part II: Model development and implementation. Polymer Composites, 17(1), 104–114.

Rezaei, F., Yunus, R., & Ibrahim, N. A. (2009). Effect of fiber length on thermomechanical properties of short carbon fiber reinforced polypropylene composites. Materials & Design, 30(2), 260–263.

Robinson, I. M., & Robinson, J. M. (1994). The influence of fibre aspect ratio on the deformation of discontinuous fibre-reinforced composites. Journal of Materials Science, 29(18), 4663–4677.

Rosen, B. W. (1973). Stiffness of fibre composite materials. Composites, 4(1), 16–25.

S.Stevenson. (2011). Overview of Fiber-Reinforced Composites. Composite Structures, 3(2), 46–54.

Prashanth, S., Subbaya, KM., Nithin, K., & Sachhidananda, S. (2017). Fiber Reinforced Composites - A Review. J Material Sci Eng 6: 341.

Suhir, E., Bubel, G. M., & Tuminaro, R. D. (1991). Predicted Curvature of a Glass Fiber from the Measured Curvature of its Coating. Journal of Lightwave Technology, 9(6), 701–708.

Ting, T. C. T. (1996). Anisotropic elasticity: theory and applications (No. 45). Oxford University Press on Demand.

Tandon, G. P., & Weng, G. J. (1984). The effect of aspect ratio of inclusions on the elastic properties of unidirectionally aligned composites. Polymer Composites, 5(4), 327–333.

Thomason, J. L. L., & Groenewoud, W. M. M. (1996). The influence of fibre length and concentration on the properties of glass fibre reinforced polypropylene: 2. Thermal properties. Composites Part A: Applied Science and Manufacturing, 27(7), 555–565.

Thomason, J. L., & Vlug, M. A. (1996). Influence of fibre length and concentration on the properties of glass fibre-reinforced polypropylene: 1. Tensile and flexural modulus. Composites Part A: Applied Science and Manufacturing, 27(6), 477–484.

Thomason, J. L., Vlug, M. A., Schipper, G., & Krikor, H. G. L. T. (1996). Influence of fibre length and concentration on the properties of glass fibre-reinforced polypropylene: Part 3. Strength and strain at failure. Composites Part A: Applied Science and Manufacturing, 27(11), 1075–1084.

Tucker, C. L., & Liang, E. (1999a). Stiffness predictions for unidirectional short-fiber composites: Review and evaluation. Composites Science and Technology, 59(5), 655–671.

Tucker, C. L., & Liang, E. (1999b). Stiffness predictions for unidirectional short-fiber composites: Review and evaluation. Composites Science and Technology, 59(5), 655–671.

Vallittu, P. K. (1995). The effect of void space and polymerization time on transverse strength of acrylic ‐ glass fibre composite. Journal of Oral Rehabilitation, 22(4), 257–261.

Velmurugan, R. (2012). Composite Materials. Composite Material, 1–8.

Velmurugan, R., Srinivasulu, G., & Jayasankar, S. (2014). Influence of fiber waviness on the effective properties of discontinuous fiber reinforced composites. Computational Materials Science, 91, 339–349.

Vincent, M., Giroud, T., Clarke, A., & Eberhardt, C. (2005). Description and modeling of fiber orientation in injection molding of fiber reinforced thermoplastics. Polymer, 46(17), 6719-6725.

Wang, R. M., Zheng, S. R., & Zheng, Y. G. (2011). Introduction to polymer matrix composites. Polymer Matrix Composites and Technology, 1–548.

Xia, Z., Zhou, C., Yong, Q., & Wang, X. (2006). On selection of repeated unit cell model and application of unified periodic boundary conditions in micro-mechanical analysis of composites. International Journal of Solids and Structures, 43(2), 266–278.

Younes, R., Hallal, A., Fardoun, F., & Hajj, F. (2012). Comparative Review Study on Elastic Properties Modeling for Unidirectional Composite Materials. Composites and Their Properties.

Zeng, D., Lu, L., Zhou, J., Li, Y., Xia, Z., Hoke, P., & Souza, D. (2015). Modeling of Long Fiber Reinforced Plastics, SAE Technical Paper 2015-01- 0698

Zeng, D., Xia, C., Webb, J., Lu, L., Gan, Y., Sun, X., & Lasecki, J. (2014). Effect of Fiber Orientation on the Mechanical Properties of Long Glass Fiber Reinforced (LGFR) Composites, SAE Technical Paper 2014-01-1049

Appendices

Appendix A: The parameters $pa(i,j)$ for IBOF

pa(i, j)	i = 3	i = 4	i = 6
j = 1	0.249 409 081 E+02	-0.497 217 790 E+00	0.234 146 291 E+02
j = 2	-0.435 101 153 E+03	0.234 980 797 E+02	20.412 048 043 E+03
j = 3	0.372 389 335 E+04	-0.391 044 251 E+03	0.319 553 200 E+04
j = 4	0.703 443 657 E+04	0.153 965 820 E+03	0.573 259 594 E+04
j = 5	0.823 995 187 E+06	0.152 772 950 E+06	-0.485 212 803 E+05
j = 6	-0.133 931 929 E+06	-0.213 755 248 E+04	-0.605 006 113 E+05
j = 7	0.880 683 515 E+06	-0.400 138 947 E+04	-0.477 173 740 E+05
j = 8	- 0.991 630 690 E+07	- 0.185 949 305 E+07	0.599 066 486 E+07
j = 9	- 0.159 392 396 E+05	0.296 004 865 E+04	- 0.110 656 935 E+05
j = 10	0.800 970 026 E+07	0.247 717 810 E+07	- 0.460 543 580 E+08
j = 11	- 0.237 010 458 E+07	0.101 013 983 E+06	0.203 042 960 E+07
j = 12	0.379 010 599 E+08	0.732 341 494 E+07	- 0.556 606 156 E+08
j = 13	-0.337 010 820 E+08	- 0.147 919 027 E+08	0.567 424 911 E+09
j = 14	0.322 219 416 E+05	- 0.104 092 072 E+05	0.128 967 058 E+05
j = 15	- 0.257 258 805 E+09	- 0.635 149 929 E+08	- 0.152 752 854 E+10
j = 16	0.214 419 090 E+07	- 0.247 435 106 E+06	- 0.499 321 746 E+07
j = 17	- 0.449 275 591 E+08	- 0.902 980 378 E+07	0.132 124 828 E+09
j = 18	- 0.213 133 920 E+08	0.724 969 796 E+07	- 0.162 359 994 E+10
j = 19	0.157 076 702 E+10	0.487 093 452 E+09	0.792 526 849 E+10
j = 20	- 0.232 153 488 E+05	0.138 088 690 E+05	0.466 767 581 E+04
j = 21	- 0.395 769 398 E+10	- 0.160 162 178 E+10	- 0.128 050 778 E+11

Appendix B: MATLAB code in the image pixel analysis and the effective fiber aspect ratio determination

```
clc,clear %%%%%%%%%%%level 0.48for W40%%%%%%%%%%%levle 0.55 for W20%%%%%%%%%%5
f=imread('021017-NorthernStarPlaque2-300x-stitch.jpg');%%%%%%%%%%%%%%%%%%%need change for each pic%%%%%%%%%%%%
c=400:4345;% column pixel%%%%%%%%%%%%%%%%%%%need change for each pic%%%%%%%%%%%%%
r=360:9000;% row pixel%%%%%%%%%%%%%%%%%%%need change for each pic%%%%%%%%%%%%%
cc=round(length(c)/5);%divided to 5 parts
rr=round(length(r)/5);%divided to 5 parts
%% caculate 25 parts
for ic=0:4
   for ir=0:4
   fc=f(c(ic*cc+1):c(cc*(ic+1)),r(ir*rr+1):r(rr*(ir+1)));
%     imshow(fc);
level=0.501; %%%%%%%%%%%%%%%%%%%%need change for each pic%%%%%%%%%%%%threshold to determine black or white
bw_image=im2bw(fc,level);
%  figure(2)
% imshow(bw_image);
area_fiber=bwarea(bw_image); % white
% The number of white pixels is simply the sum of all the image pixel values since each white pixel has value 1.
% If the white pixels have value 255 then divide the sum by 255.
% numberOfWhitePixels = sum(bw_image(:))%
% The number of black pixels is simply the total number of pixels in the image minus the number of white pixels.
numberOfAllPixels = numel(bw_image);%
VF_area = area_fiber  / numberOfAllPixels;
% formatSpec = 'Volume fraction of number%2.0f%1.0f is%8.3f \n';
% fprintf(formatSpec,ic+1,ir+1,VF_area)
formatSpec = '%8.3f \n';
fprintf(formatSpec,VF_area)
   end
end

% %% caculate 5 rows
% for ic=0:4
%     fc=f(c(ic*cc+1):c(cc*(ic+1)),r);
% %     imshow(fc);
% level=0.475; %%%%%%%%%%%%%%%%%%%%%%%%%%%%%%%%%%%%%%%%%%%%%%%%%%%%%%%%%%%%%%%%need change for each pic%%%%%%%%%%%%%% threshold to determine black or white
% bw_image=im2bw(fc,level);
% %  figure(2)
% % imshow(bw_image);
% area_fiber=bwarea(bw_image); % white
% % The number of white pixels is simply the sum of all the image pixel values since each white pixel has value 1.
```

```
% % If the white pixels have value 255 then divide the sum by 255.
% % numberOfWhitePixels = sum(bw_image(:))%
% % The number of black pixels is simply the total number of pixels in the image minus the number of white pixels.
% numberOfAllPixels = numel(bw_image);%
% VF_area = area_fiber  / numberOfAllPixels;
% % formatSpec = 'Volume fraction of row%2.0f is%8.3f \n';
% % fprintf(formatSpec,ic+1,VF_area)
% formatSpec = '%8.3f \n';
% fprintf(formatSpec,VF_area)
%
% end
%
function [fitresult, gof] = createFit(Ideal_AR, Curvature_Angle, Effective_AR_VF15)
%CREATEFIT(IDEAL_AR,CURVATURE_ANGLE,EFFECTIVE_AR_VF10)
%  Create a fit.
%
%  Data for 'untitled fit 1' fit:
%      X Input : Ideal_AR
%      Y Input : Curvature_Angle
%      Z Output: Effective_AR_VF10
%  Output:
%      fitresult : a fit object representing the fit.
%      gof : structure with goodness-of fit info.
%
%  See also FIT, CFIT, SFIT.

%  Auto-generated by MATLAB on 06-Oct-2017 14:36:51


%% Fit: 'untitled fit 1'.
[xData, yData, zData] = prepareSurfaceData( Ideal_AR, Curvature_Angle, Effective_AR_VF15 );

% Set up fittype and options.
ft = fittype( 'poly23' );
opts = fitoptions( ft );
opts.Lower = [-Inf -Inf -Inf -Inf -Inf -Inf -Inf -Inf -Inf];
opts.Robust = 'Bisquare';
opts.Upper = [Inf Inf Inf Inf Inf Inf Inf Inf Inf];
opts.Normalize = 'off';

% Fit model to data.
[fitresult, gof] = fit( [xData, yData], zData, ft, opts );

% Plot fit with data.
figure( 'Name', 'untitled fit 1' );
h = plot( fitresult, [xData, yData], zData );
 legend( h, 'untitled fit 1', 'Effective AR VF15 vs. Ideal AR, Curvature Angle', 'Location', 'NorthEast' );
```

```
% Label axes
xlabel( 'Ideal AR' );
ylabel( 'Curvature Angle' );
zlabel( 'Effective AR VF15' );
grid on
view( -135, 15.0 );
function [fitresult, gof] = createFit(Ideal_AR, Curvature_Angle, Effective_AR_VF10)
%CREATEFIT(IDEAL_AR,CURVATURE_ANGLE,EFFECTIVE_AR_VF10)
%  Create a fit.
%
%  Data for 'untitled fit 1' fit:
%      X Input : Ideal_AR
%      Y Input : Curvature_Angle
%      Z Output: Effective_AR_VF10
%  Output:
%      fitresult : a fit object representing the fit.
%      gof : structure with goodness-of fit info.
%
%  See also FIT, CFIT, SFIT.

%  Auto-generated by MATLAB on 06-Oct-2017 14:36:51


%% Fit: 'untitled fit 1'.
[xData, yData, zData] = prepareSurfaceData( Ideal_AR, Curvature_Angle, Effective_AR_VF10 );

% Set up fittype and options.
ft = fittype( 'poly23' );
opts = fitoptions( ft );
opts.Lower = [-Inf -Inf -Inf -Inf -Inf -Inf -Inf -Inf -Inf];
opts.Robust = 'Bisquare';
opts.Upper = [Inf Inf Inf Inf Inf Inf Inf Inf Inf];
opts.Normalize = 'on';

% Fit model to data.
[fitresult, gof] = fit( [xData, yData], zData, ft, opts );

% Plot fit with data.
figure( 'Name', 'untitled fit 1' );
h = plot( fitresult, [xData, yData], zData );
legend( h, 'untitled fit 1', 'Effective AR VF10 vs. Ideal AR, Curvature Angle', 'Location', 'NorthEast' );
% Label axes
xlabel( 'Ideal AR' );
ylabel( 'Curvature Angle' );
zlabel( 'Effective AR VF10' );
grid on
view( -135, 15.0 );
```

```
clc,clear
AR=[5,10,15,20,50,60,80,100,110];
y1=(3.03690112118+3.14741831138+2.92724618731+3.00001164151+3.11749576035)/5;
y2=(4.27692554668+4.39820502454+3.88199573163+4.25995086759+4.15359592744)/5;
y3=(4.73417047359+5.11000493448+5.31875608463+5.11755945673+5.15714471539)/5;
y4=(6.05325212299+5.75256614031+5.97836386349+5.94748385343+5.82573472734)/5;
y5=(7.09710312895+6.89876170129+7.19249489211+6.27527243209+7.08062526369)/5;
y6=(7.24694818171+7.0412446152+7.24675818903+7.44598475546+6.54447103729)/5;
y7=(7.67229122225+7.65618701445+6.15258797275+7.72517384528+7.50938830228)/5;
E11_10VF=[y1,y2,y3,y4,y5,y6,7.23,y7];
yy1=(3.8688006642+3.83773502379+3.85016014195+3.76771695751+4.09646674745)/5;
yy2=(6.64597981823+5.83856024949+5.94040612685+5.83165141428+6.26538771164)/5;
yy3=(7.31392636795+6.76657867905+7.63256235227+7.80934627329+7.47951589988)/5;
yy4=(7.73400330629+8.73614850313+8.6809559337+8.95308645546+8.66498346982)/5;
yy5=(10.3138422968+9.55533552248+9.76303758963+10.5784394829+10.3531270898)/5;
yy6=(10.655242456+10.8556188941+10.3605048733+10.8440823711+10.8179854482)/5;
yy7=(11.3061207596+11.2823781763+0.5396035582+10.3811845194+11.2271494607)/5;
E11_15VF=[yy1,yy2,yy3,yy4,yy5,yy6,10.7,yy7];
% p=polyfit(AR,E11_15VF,4);
% x=linspace(5,100);
% E11_15=p(1)*x.^4+p(2)*x.^3+p(3)*x.^2+p(4)*x+p(5);
p=polyfit(AR,E11_15VF,5);
x=linspace(5,100);
E11_15=p(1)*x.^5+p(2)*x.^4+p(3)*x.^3+p(4)*x.^2+p(5)*x.^1+p(6);
pp=polyfit(AR,E11_10VF,5);
xx=linspace(5,100);
E11_10=pp(1)*xx.^5+pp(2)*xx.^4+pp(3)*xx.^3+pp(4)*xx.^2+pp(5)*xx+pp(6);
figure(1)
plot(xx,E11_10)
xlabel( 'Aspect Ratio' );
ylabel( 'E11(GPa)' );
title('E11 for aligned fiber case with VF=10%')
grid on
hold on
plot(AR(1:7),E11_10VF(1:7),'r*')
figure(2)
plot(x,E11_15)
xlabel( 'Aspect Ratio' );
ylabel( 'E11(GPa)' );
title('E11 for aligned fiber case with VF=15%')
grid on
hold on
plot(AR(1:7),E11_15VF(1:7),'r*')
figure(3)
subplot(2,1,1)
plot(xx,E11_10,'LineWidth',2)
xlabel( 'Aspect Ratio' );
```

```
ylabel( 'E11(GPa)' );
title('E11 for aligned fiber case with VF=10%')
grid on
hold on
plot(AR(1:8),E11_10VF(1:8),'r*')
subplot(2,1,2)
plot(x,E11_15,'LineWidth',2)
xlabel( 'Aspect Ratio' );
ylabel( 'E11(GPa)' );
title('E11 for aligned fiber case with VF=15%')
grid on
hold on
plot(AR(1:8),E11_15VF(1:8),'r*')
figure(4)
plot(xx,E11_10)
xlabel( 'Aspect Ratio' );
ylabel( 'E11(GPa)' );
title('E11 for aligned fiber case with VF=10%')
grid on
hold on


% %%%%
```

```
Effective_VF10_AR_50=(50/Effective_VF10_AR_50(1))*Effective_VF10_AR_50;

zhi_VF10_AR_60=[7159.40 6846.481481 6446.938272 6122.864198 5931.00 5683.85 5442.70
        5075.27]/1000; %%the reslut from the abaqus%%%%%%%%%%%%%%%%%%%
for i=1:length(zhi_VF10_AR_60)
syms xx
eqn=pp(1)*xx^5+pp(2)*xx^4+pp(3)*xx^3+pp(4)*xx^2+pp(5)*xx+pp(6)==zhi_VF10_AR_60(i);
solxx=solve(eqn,xx);
Effective_AR60(i)=solxx(1);
end
Effective_VF10_AR_60=double(Effective_AR60);
% Effective_VF10_AR_60=-(Effective_VF10_AR_60(1)-60)+Effective_VF10_AR_60
Effective_VF10_AR_60=(60/Effective_VF10_AR_60(1))*Effective_VF10_AR_60;

zhi_VF10_AR_100=[7419.21 6944.57 6661.99 6381.00 6023.26 5793.04 5573.79 5275.23]/1000; %%the reslut
from the abaqus
for i=1:length(zhi_VF10_AR_100)
syms xx
eqn=pp(1)*xx^5+pp(2)*xx^4+pp(3)*xx^3+pp(4)*xx^2+pp(5)*xx+pp(6)==zhi_VF10_AR_100(i);
solxx=solve(eqn,xx);
Effective_AR100(i)=solxx(1);
end
Effective_VF10_AR_100=double(Effective_AR100);
% Effective_VF10_AR_100=-(Effective_VF10_AR_100(1)-100)+Effective_VF10_AR_100
Effective_VF10_AR_100=(100/Effective_VF10_AR_100(1))*Effective_VF10_AR_100;

Curvature_Angle=[0 22.27435215 31.6220778 38.88044929 45.07361984 50.59738795
        55.65437888 60.36486632 0 22.27435215 31.6220778 38.88044929
        45.07361984 50.59738795 55.65437888 60.36486632 0 22.27435215
        31.6220778 38.88044929 45.07361984 50.59738795 55.65437888
        60.36486632 0 22.27435215 31.6220778 38.88044929 45.07361984
        50.59738795 55.65437888 60.36486632];
Ideal_AR=[20,20,20,20,20,20,20,20,50,50,50,50,50,50,50,50,60,60,60,60,60,60,60,60,100,100,100,100,100,100,100,100];
Effective_AR_VF10=[Effective_VF10_AR_20,Effective_VF10_AR_50,Effective_VF10_AR_60,Effective_VF10_AR_100];

% createFitVF10(Ideal_AR, Curvature_Angle, Effective_AR_VF10)
createFit(Ideal_AR, Curvature_Angle, Effective_AR_VF10)
% % %
% % %
% % % %%%%%%%%%%%%%%%%%%%%
```

```
solx=solve(eqnx,x);
Effective_AR20VF15(i)=solx(1);
end
Effective_VF15_AR_20=double(Effective_AR20VF15);
% Effective_VF10_AR_20=-(Effective_VF10_AR_20(1)-20)+Effective_VF10_AR_20
 Effective_VF15_AR_20=(20/Effective_VF15_AR_20(1))*Effective_VF15_AR_20;

zhi_VF15_AR_50=[10209.12 8802.59 7402.30 6887.26 6435.98 6062.11 5634.88 5232.62]/1000; %%the reslut from the abaqus
for i=1:length(zhi_VF15_AR_50)
syms x
eqnx=p(1)*x^5+p(2)*x^4+p(3)*x^3+p(4)*x^2+p(5)*x+pp(6)==zhi_VF15_AR_50(i);
solx=solve(eqnx,x);
Effective_AR50VF15(i)=solx(1);
end
Effective_VF15_AR_50=double(Effective_AR50VF15);
% Effective_VF15_AR_50=-(Effective_VF15_AR_50(1)-50)+Effective_VF15_AR_50;
 Effective_VF15_AR_50=(50/Effective_VF15_AR_50(1))*Effective_VF15_AR_50;

zhi_VF15_AR_60=[10731.40 9530.30  7790.320988 7317.36 6846.64 6223.49 5717.47 5411.32]/1000; %%the reslut from the
abaqus%%%%%%%%%%%%%%%%%%
for i=1:length(zhi_VF15_AR_60)
syms x
eqnx=p(1)*x^5+p(2)*x^4+p(3)*x^3+p(4)*x^2+p(5)*x+pp(6)==zhi_VF15_AR_60(i);
solx=solve(eqnx,x);
Effective_AR60VF15(i)=solx(1);
end
Effective_VF15_AR_60=double(Effective_AR60VF15);
% Effective_VF15_AR_60=-(Effective_VF15_AR_60(1)-60)+Effective_VF15_AR_60;
 Effective_VF15_AR_60=(60/Effective_VF15_AR_60(1))*Effective_VF15_AR_60;

zhi_VF15_AR_100=[10944.30 9876.37 8577.74 7975.22 7137.77 6498.80 6090.68 5777.16 ]/1000; %%the reslut from the abaqus
for i=1:length(zhi_VF15_AR_100)
syms x
eqnx=p(1)*x^5+p(2)*x^4+p(3)*x^3+p(4)*x^2+p(5)*x+pp(6)==zhi_VF15_AR_100(i);
solx=solve(eqnx,x);
Effective_AR100VF15(i)=solx(1);
end
Effective_VF15_AR_100=double(Effective_AR100VF15);
% Effective_VF10_AR_100=-(Effective_VF10_AR_100(1)-100)+Effective_VF10_AR_100
Effective_VF15_AR_100=(100/Effective_VF15_AR_100(1))*Effective_VF15_AR_100;


Effective_AR_VF15=[Effective_VF15_AR_20,Effective_VF15_AR_50,Effective_VF15_AR_60,Effective_VF15_AR_100];

createFit15(Ideal_AR, Curvature_Angle, Effective_AR_VF15)
```

Curriculum Vitae

Name:	Xiaotian Yi
Post-secondary Education and Degrees:	University of Windsor Windsor, Ontario, Canada 2012-2016 Bachelor Western University London, Ontario, Canada 2016-2018 Master
Related Work Experience	Teaching Assistant Research Assistant
2016-2018	Western University